AMPLIFIER LINEARIZATION USING ADAPTIVE ANALOG PREDISTORTION

by

Flaviu C. Costescu

B.A.Sc., Simon Fraser University, 1991

THESIS SUBMITTED IN PARTIAL FULFILLMENT OF

THE REQUIREMENTS FOR THE DEGREE OF

MASTER OF APPLIED SCIENCE

in the School of Engineering Science

SIMON FRASER UNIVERSITY

January, 1992

APPROVAL

Name: Flaviu C. Costescu

Degree: Master of Applied Science (Engineering Science)

Title of Thesis: Amplifier Linearization Using Adaptive Analog Predistortion

Examining Committee:

Chair:

Dr. John Jones
Associate Professor
School of Engineering Science

Senior Supervisor:

Dr. Shawn Stapleton
Assistant Professor
School of Engineering Science

Supervisor:

Dr. James K. Cavers
Professor
School of Engineering Science

Examiner:

Dr. Marek Syrzycki
Associate Professor
School of Engineering Science

Date Approved: January 31, 1992

PARTIAL COPYRIGHT LICENSE

I hereby grant to Simon Fraser University the right to lend my thesis, project or extended essay (the title of which is shown below) to users of the Simon Fraser University Library, and to make partial or single copies only for such users or in response to a request from the library of any other university, or other educational institution, on its own behalf or for one of its users. I further agree that permission for multiple copying of this work for scholarly purposes may be granted by me or the Dean of Graduate Studies. It is understood that copying or publication of this work for financial gain shall not be allowed without my written permission.

Title of Thesis/Project/Extended Essay

Amplifier Linearization Using Adaptive Predistortion

Author: _____
(signature)

Flaviu Costescu
(name)

January 31, 1992
(date)

ABSTRACT

Linear modulation methods possess good spectral efficiency. However, their fluctuating envelopes, in conjunction with typically nonlinear power amplifiers, lead to spectral spreading and adjacent channel emissions. A method used to achieve high power efficiency and low adjacent channel emissions is to linearize the power amplifier using predistortion.

This thesis presents the design and implementation of an analog adaptive polynomial predistorter linearizer. The adaptive predistortion approach is to minimize the transmitter output power in spectral regions occupied only by intermodulation distortion products, which for a single channel data signal is the adjacent channel. By monitoring the out-of-band power, an estimate for the distortion introduced by the power amplifier is obtained. The optimization methods adjust the predistorter parameters so as to minimize the intermodulation distortion power value.

Direct search and gradient optimization methods are first simulated and compared for speed of convergence using a 16 QAM input signal. A simulated 15 dB reduction in the power amplifier's intermodulation distortion skirts was obtained as a result of optimization. The adaptive analog predistorter was then implemented and a 10-12 dB reduction in the power amplifier's intermodulation distortion skirts was obtained with a 16 QAM input signal.

ACKNOWLEDGEMENTS

I would like to thank my committee members Dr. John Jones, Dr. Shawn Stapleton, Dr. Jim Cavers and Dr. Marek Syrzycki for taking the time to be part of my committee. Special thanks are due to my senior supervisor, Dr. Shawn Stapleton for his supervision during the course of the thesis work and for the fruitful discussions and suggestions during the times when I experienced difficulties. I would also like to thank Sirooj Rambaran for the technical aid he provided, Gurmail Kandola for his help on the analysis of the predistorter and Derek Hilborn for the implementation of the 16 QAM modem, much needed in the testing of the predistorter.

For my mother and father with love

Table of Contents

List of Figures

List of Tables

List of Abbreviations and Symbols

ADC	analog to digital converter
AM-AM	input amplitude modulation to output amplitude modulation relationship
AM-PM	input amplitude modulation to output phase modulation relationship
DAC	digital to analog converter
DFP	Davidon Fletcher Powell
DSP	digital signal processing
IF	intermediate frequency
IM_o	average power of intermodulation distortion products
IMD	intermodulation distortion
LINC	linear amplification using non-linear components
LUT	look-up-table
OBO	output back-off power
OQPSK	offset quadrature phase shift keying
PSD	power spectral density
QAM	quadrature amplitude modulation
QPSK	quadrature phase shift keying
RF	radio frequency
F_1	2^{nd} order function that interpolates the AM-AM nonlinearities of the power amplifier
F_2	2^{nd} order function that interpolates the AM-PM nonlinearities of the power amplifier

1 INTRODUCTION

Constant envelope modulation such as FM allows the power amplifiers to be operated close to saturation for high power efficiency. However, due to the limited spectrum allotted for mobile communication applications, higher spectrum efficient modulation techniques like QPSK and 16 QAM are required. The varying envelope of the QAM signals generate intermodulation distortion (IMD) products from the nonlinear power amplifier. In mobile communication systems, the adjacent channel interference has to be 60 dB lower than the in-band carrier level [1]. One way to reduce the adjacent channel interference is to back off the power amplifier to a linear operating region, decreasing the efficiency of the power amplifier. In order to achieve both spectrum and power efficiency, the power amplifier has to be linearized.

There are several types of linearization techniques used to reduce the power amplifier's out-of-band emission. The five categories of linearization techniques are active biasing, feed-forward, LINC, negative feedback, and predistortion.

Active biasing linearization [2] uses the envelope of the input signal to alter the operating bias point of the transistor. The envelope of the input signal is applied to a nonlinear function that interpolates the inverse nonlinearities of the transistor. The output of the nonlinear function is applied to the base of the transistor and the bias point of the transistor is varied as a function of the envelope input signal. Due to filtering requirements in the bias network, active biasing linearization is restricted to narrow bandwidths. Also, since the system operates as an open loop, some form of adaptation is required to compensate for transistor drift.

Feed-forward linearization [3] uses the vector error signal between the power amplifier's output signal and a time-delayed version of the input signal to correct for the distortion introduced by the power amplifier. This technique has demonstrated good IMD cancellation and is capable of achieving good power efficiency, however, it tends to be sensitive and expensive, since the up-converter hardware is doubled.

LINC is an acronym for LInear Amplification using Non-linear Components. The concept of the LINC technique is to convert the input bandpass signal having amplitude and phase nonlinearities into two constant envelope signals that are combined before transmission [4]. The LINC technique can be used with power efficient amplifiers. On the other hand, the LINC technique needs components with very stable characteristics and possesses an increased level of complexity.

The negative feedback or Cartesian feedback technique [5,6] is one of the simplest linearization techniques. Although this technique is simple, it has several shortcomings. Stability is a serious problem since it depends on precise adjustment of the phase shifter and feedback gain.

Predistortion [7]-[11] is the most commonly used technique for linearizing an amplifier. The concept of predistortion is to insert a nonlinear module between the input signal and the power amplifier. The nonlinear module generates IMD products that are in anti-phase with the IMD products generated by the power amplifier, hence, reducing the power amplifier's out-of-band emission. A basic predistortion block diagram is presented in Figure 1.1.

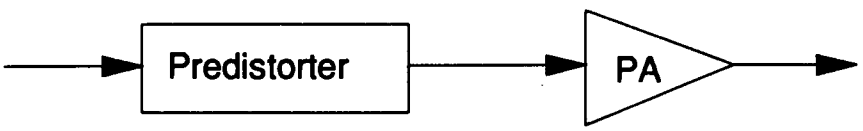

Figure 1.1. Basic Predistorter Block Diagram

Several predistortion linearizers have been developed during the past decade. IN general, there are three basic predistorter techniques. The baseband predistorter predistorts each vector of the baseband signal using DSP hardware [12]. The cuber predistorter [8], uses an anti-parallel pair of diodes as the nonlinear module and it reduces strictly the third order IMD products. The third predistortion technique uses the envelope of the modulating signal to generate two second order nonlinear functions that interpolate the inverse AM-AM and AM-PM nonlinearities of the power amplifier. These two second order nonlinear functions are used to predistort the power

amplifier.

A robust predistorter should incorporate some form of adaptation, since the power amplifier's characteristics tend to drift with time. These drifts are caused by changes in temperature, supply voltage variations, aging of devices and switching between channels. A simplified block diagram of the adaptive analog predistorter designed and implemented for this thesis is shown in Figure 1.2.

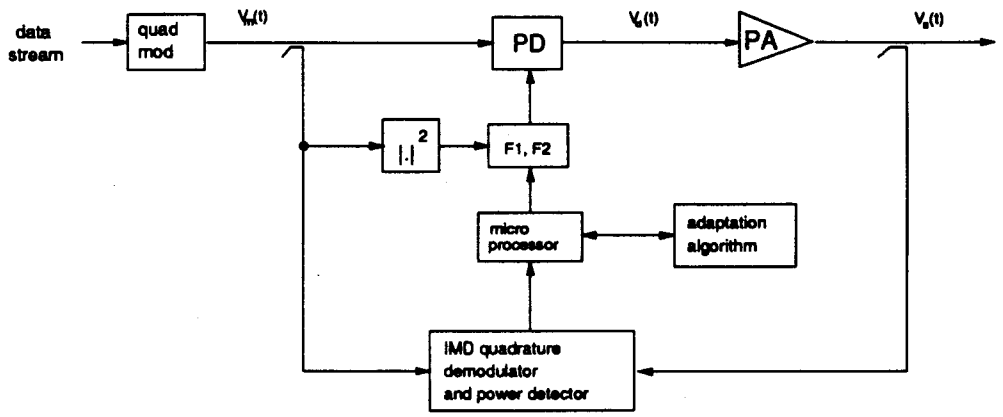

Figure 1.2. Adaptive Analog Predistorter

The linearizer creates a predistorted version $V_d(t)$ of the desired modulation $V_m(t)$. The predistorter block is made up of a complex phasor modulator which controls both the amplitude and phase of the input RF signal. The amount of predistortion is controlled by two nonlinear second order functions F_1 and F_2 that interpolate the inverse AM-AM and AM-PM nonlinearities of the power amplifier. Note that F_1 and F_2 are functions of the complex envelope of the modulating signal.

The feedback path, couples a portion of the input bandpass signal and power amplifier output signal, $V_m(t)$ and $V_a(t)$ respectively, to the IMD quadrature demodulator and power detector circuit. Here, the IMD products are down-converted to baseband, and the contribution of the 3rd and 5th order IMD products is filtered out of the spectrum. The power in the undesired spectrum is then detected and averaged to obtain a magnitude IM_o which will be used to adjust the linearizer. The adaptation algorithm adjusts the F_1 and F_2 coefficient values so as to

minimize the out-of-band power magnitude IM_o. Note that the micro-controller is a very important part of the linearizer, since it controls the flow of information between the F_1 and F_2 polynomial generator circuit, IMD quadrature demodulator and power detector circuit and adaptation algorithm.

This thesis describes the design and implementation of an adaptive predistorter linearizer. Chapter 2 of the thesis presents the mathematical system analysis and shows how predistortion reduces the 3rd and 5th order IMD products generated by the power amplifier. Chapter 3 describes various optimization methods that can be used to adaptively minimize the out-of-band power generated by the power amplifier. Next, chapter 4 outlines the simulation model used to simulate the performance of the adaptive predistorter and shows the simulation results obtained. Chapter 5 describes the hardware implementation of the adaptive predistorter while Chapter 6 presents the results obtained with the implemented adaptive predistorter.

2 SYSTEM ANALYSIS

This chapter presents a detailed analysis of the adaptive predistorter. The first section describes the analysis of the system using a real bandpass model. The second section describes the composite model analysis. Third section uses an amplitude modulated (AM) signal to show how predistortion can reduce the 3rd and 5th order IMD products. Finally, the last section of this chapter describes mathematically how the IMD products of the power amplifier are separated from the spectrum.

2.1 Analysis of the System Using a Bandpass Model

A detailed block diagram of a transmitter with an adaptive predistorter is illustrated in Figure 2.1.

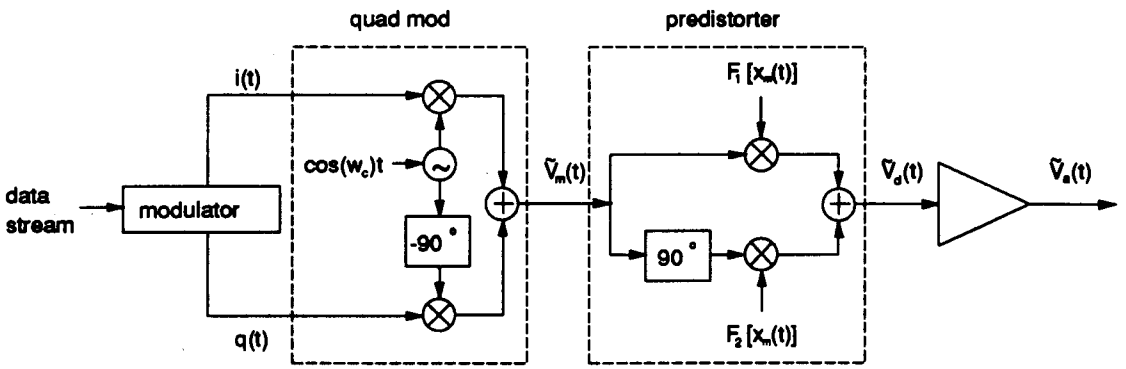

Figure 2.1. Detailed Diagram of Adaptive Predistorter

The modulator converts the input data stream into the desired modulation scheme (i.e. 16 QAM, QPSK, OQPSK). The complex baseband signal $V_m(t)$ is expressed as

$$V_m(t) = i(t) + jq(t) = a_m(t)e^{j\Phi(t)} \tag{2.1}$$

The complex baseband signal $V_m(t)$ is then up-converted into a real bandpass signal $\tilde{V}_m(t)$ using a quadrature modulator. The real bandpass signal $\tilde{V}_m(t)$ can be written as

$$\tilde{V}_m(t) = i(t)\cos(\omega_c t) - q(t)\sin(\omega_c t) = \Re e\{V_m(t)e^{j\omega_c t}\} \tag{2.2}$$

$V_m(t)$ in equation (2.2) is commonly referred to as the complex envelope. The predistorter modelled by a quadrature structure, creates a predistorted real bandpass signal $\tilde{V}_d(t)$. This is accomplished as a result of the multiplication of the in-phase and quadrature components of the bandpass input signal $\tilde{V}_m(t)$ by the in-phase and quadrature nonlinearities of the predistorter. The predistorter's nonlinearities are modelled by two 2nd order nonlinear functions denoted by F_1 and F_2. The two functions interpolate the inverse AM-AM and AM-PM nonlinearities of the power amplifier and are represented by

$$F_1[x_m(t)] = \alpha_{11} + \alpha_{13}x_m(t) + \alpha_{15}x_m^2(t) \tag{2.3}$$

$$F_2[x_m(t)] = \alpha_{21} + \alpha_{23}x_m(t) + \alpha_{25}x_m^2(t) \tag{2.4}$$

where $x_m(t)=|V_m(t)|^2$ since F_1 and F_2 are amplitude dependent. Using the F_1 and F_2 functions, the predistorter's complex gain, $F[x_m(t)]$, can be expressed as

$$F[x_m(t)] = F_1[x_m(t)] + j \cdot F_2[x_m(t)] = \alpha_1 + \alpha_3 x_m(t) + \alpha_5 x_m^2(t) \tag{2.5}$$

where $\alpha_i=\alpha_{1i}+j\alpha_{2i}$ are complex coefficients that model the power amplifier's inverse AM-AM and AM-PM nonlinearities. The predistorted real bandpass signal $\tilde{V}_d(t)$ can now be written as

$$\tilde{V}_d(t) = \Re e\{V_d(t)e^{j\omega_c t}\} = \Re e\{V_m(t)F[x_m(t)]e^{j\omega_c t}\} \tag{2.6}$$

Note that the $\tilde{V}_d(t)$ expression ignores the even order terms, since they generate distortion outside the frequency band of interest. Next, to model the power amplifier, the quadrature structure of Figure 2.2 is used [3].

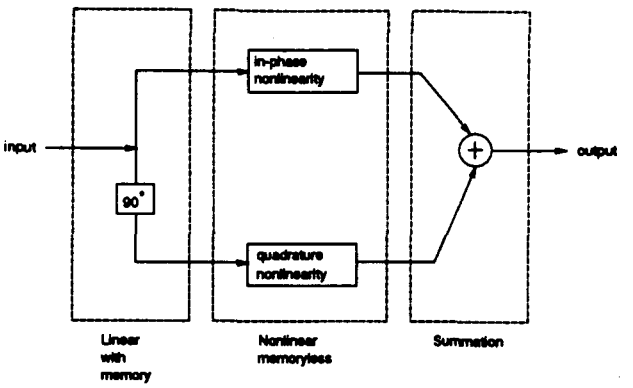

Figure 2.2. Quadrature Model of Power Amplifier

As illustrated in Figure 2.2, the quadrature structure is made up of a 90° power splitter, two memoryless nonlinearities and a summation block. The nonlinearities are functions of the magnitude of the input signal and they are represented using power series. The quadrature model can be drawn in real bandpass form as illustrated in Figure 2.3

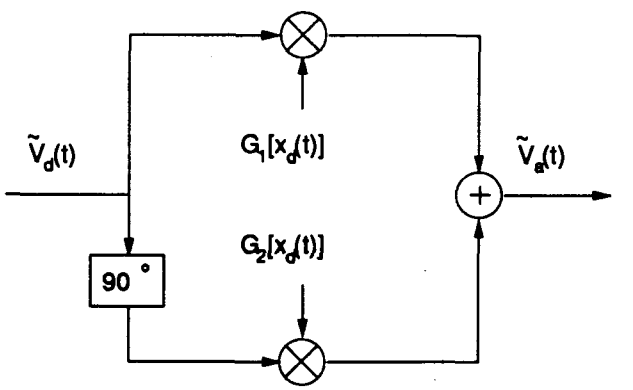

Figure 2.3. Real Bandpass Form of the Quadrature Structure

The G_1 and G_2 functions model the power amplifier's AM-AM and AM-PM nonlinearities, respectively. The two nonlinearities are represented by power series of the form

$$G_1[x_d(t)] = \beta_{11} + \beta_{13}x_d(t) + \beta_{15}x_d(t) \tag{2.7}$$

$$G_2[x_d(t)] = \beta_{21} + \beta_{23}x_d(t) + \beta_{25}x_d(t) \tag{2.8}$$

where $x_d(t)=|V_d(t)|^2$. Using complex notation, the power amplifier's complex gain is expressed as

$$G[x_d(t)] = G_1[x_d(t)] + jG_2[x_d(t)] = \beta_1 + \beta_3 x_d(t) + \beta_5 x_d^2(t) \tag{2.9}$$

where $\beta_i=\beta_{1i}+j\beta_{2i}$ are complex coefficients that model the power amplifier's AM-AM and AM-PM characteristics and can be obtained in practice by characterizing the power amplifier.

Using the quadrature structure model, the power amplifier's real bandpass output signal becomes

$$\tilde{V}_a(t) = \Re e\{V_a(t)e^{j\omega_c t}\} = \Re e\{V_m(t)F[x_m(t)]G[x_d(t)]e^{j\omega_c t}\} \tag{2.10}$$

As illustrated by equation (2.10), the complex envelope of the power amplifier's output signal is a function of the complex envelopes of the input signal, predistorter and power amplifier. This indicates that an analysis having the signals in complex envelope form is more suitable. Next section demonstrates how the predistorter and power amplifier can be modelled by a composite model using the complex gains of the predistorter and power amplifier.

2.2 Analysis of the System Using a Composite Model

This section shows mathematically how the 3rd and 5th order IMD products of the power amplifier can be reduced by the 3rd and 5th order components generated by the predistorter. Start by modelling the predistorter and power amplifier using a composite model in complex gain form as shown in Figure 2.3.

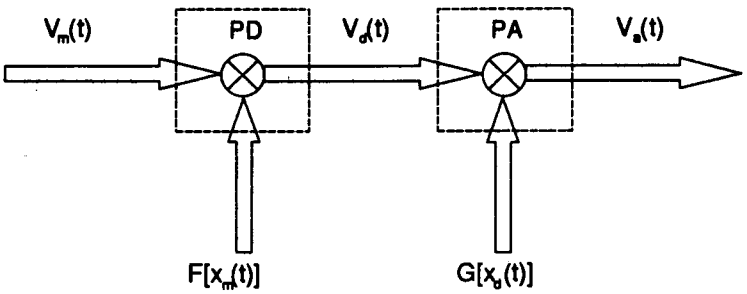

Figure 2.4. Block Diagram of Complex Predistorter and Power Amplifier

Using Figure 2.4's notation, the power amplifier's output signal, $V_a(t)$ is

$$V_a(t) = V_d(t) \cdot G[x_d(t)] \tag{2.11}$$

where $G[x_d(t)]$ is the power amplifier's complex gain and can be approximated by a truncated power series of the form

$$G[x_d(t)] = \beta_1 + \beta_3 x_d(t) + \beta_5 x_d^2(t) = G_1[x_d(t)] + j \cdot G_2[x_d(t)] \tag{2.12}$$

As mentioned previously, β_1, β_3 and β_5 are complex coefficients that account for the power amplifier's AM-AM and AM-PM nonlinearities. By expressing the predistorted signal $V_d(t)$ in terms of its complex gain, the overall complex gain expression of the predistorter and power amplifier becomes

$$V_a(t) = V_m(t) \cdot F[x_m(t)] \cdot G[x_d(t)] \tag{2.13}$$

where $F[x_m(t)]$ is the predistorter's complex gain and can be approximated by a truncated power series of the form

$$F[x_m(t)] = \alpha_1 + \alpha_3 x_m(t) + \alpha_5 x_m^2(t) = F_1[x_m(t)] + j \cdot F_2[x_m(t)] \tag{2.14}$$

α_1, α_3 and α_5 are complex coefficients that interpolate the power amplifier's inverse AM-AM and AM-PM nonlinearities.

Equation (2.14) indicates that the input and output complex envelopes, $V_m(t)$ and $V_a(t)$ respectively, are related by a composite complex gain $F[x_m(t)] \cdot G[x_d(t)]$. By defining the composite complex gain $K[x_m(t)]$ as

$$K[x_m(t)] = F[x_m(t)] \cdot G[x_d(t)] = F[x_m(t)] \cdot G[x_m(t) \cdot |F[x_m(t)]|^2] \tag{2.15}$$

the concatenated predistorter and power amplifier complex gain can be modelled by the composite complex model illustrated in Figure 2.5.

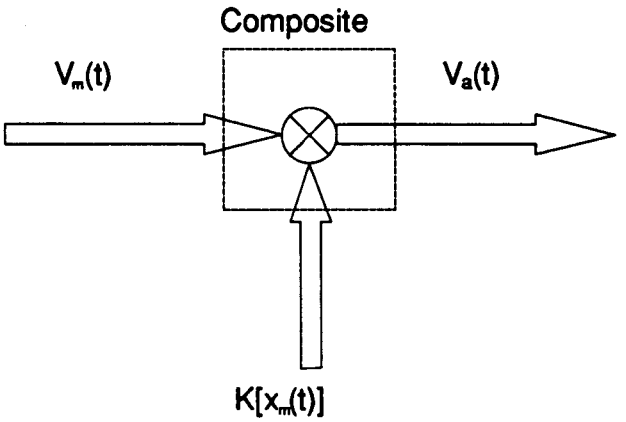

Figure 2.5. Block diagram of Composite Complex Model

Furthermore, the composite complex gain can be approximated by a truncated power series of the form

$$K[x_m(t)] = \gamma_1 + \gamma_3 x_m(t) + \gamma_5 x_m^2(t) = K_1[x_m(t)] + j \cdot K_2[x_m(t)] \tag{2.16}$$

where $K_1[x_m(t)]$ and $K_2[x_m(t)]$ are the composite in-phase and quadrature nonlinearities and can be expressed as

$$K_1[x_m(t)] = \gamma_{11} + \gamma_{13} x_m(t) + \gamma_{15} x_m^2(t) \tag{2.17}$$

$$K_2[x_m(t)] = \gamma_{21} + \gamma_{23} x_m(t) + \gamma_{25} x_m^2(t) \tag{2.18}$$

The composite complex gain coefficients γ are functions of the predistorter's α and power amplifier's β coefficients. By combining equations (2.12), (2.14), (2.15) and (2.16), the relationship between the α, β and γ coefficients can be found. The complete mathematical derivation is presented in Appendix A. The expressions for the γ coefficients as found in Appendix A are

$$\gamma_1 = \alpha_1 \beta_1 \tag{2.19}$$

$$\gamma_3 = \alpha_3 \beta_1 + \alpha_1 \beta_3 |\alpha_1|^2 \tag{2.20}$$

$$\gamma_5 = \alpha_5 \beta_1 + \alpha_3 \beta_3 |\alpha_1|^2 + \alpha_1 \beta_5 |\alpha_1|^4 + 2\alpha_1 \beta_3 \cdot \Re e\{\alpha_1 \alpha_3^*\} \tag{2.21}$$

Furthermore, the 3rd and 5th order composite coefficients can be expressed in terms of the real and imaginary parts of the α and β coefficients as

$$\gamma_{13} = \alpha_{13}\beta_{11} - \alpha_{23}\beta_{21} + \alpha_{11}^3\beta_{13} - \alpha_{11}^2\alpha_{21}\beta_{23} + \alpha_{11}\alpha_{21}^2\beta_{13} - \alpha_{21}^3\beta_{23} \tag{2.22}$$

$$\gamma_{23} = \alpha_{23}\beta_{11} + \alpha_{13}\beta_{21} + \alpha_{11}^2\alpha_{21}\beta_{13} + \alpha_{11}^3\beta_{23} + \alpha_{21}^3\beta_{13} + \alpha_{11}\alpha_{21}^2\beta_{23} \tag{2.23}$$

$$\begin{aligned}\gamma_{15} = {} & -\alpha_{21}^5\beta_{25} + \alpha_{11}^5\beta_{15} + \alpha_{11}\alpha_{21}^4\beta_{15} - \alpha_{21}\alpha_{11}^4\beta_{25} + 2\alpha_{11}^3\alpha_{21}^2\beta_{15} - 2\alpha_{21}^3\alpha_{11}^2\beta_{25} \\ & + \alpha_{13}\alpha_{11}^2\beta_{13} + \alpha_{13}\alpha_{21}^2\beta_{13} - \alpha_{23}\alpha_{11}^2\beta_{23} - \alpha_{23}\alpha_{21}^2\beta_{23} + 2\alpha_{11}^2\alpha_{13}\beta_{13} \\ & - 2\alpha_{21}^2\alpha_{23}\beta_{23} - 2\alpha_{21}\alpha_{11}\alpha_{13}\beta_{23} + 2\alpha_{11}\alpha_{21}\alpha_{23}\beta_{13} + \alpha_{15}\beta_{11} - \alpha_{25}\beta_{21}\end{aligned} \tag{2.24}$$

$$\begin{aligned}\gamma_{25} = {} & \alpha_{21}^5\beta_{15} + \alpha_{11}^5\beta_{25} + \alpha_{11}\alpha_{21}^4\beta_{25} + \alpha_{11}^4\alpha_{21}\beta_{15} + 2\alpha_{21}^3\alpha_{11}^2\beta_{15} + 2\alpha_{11}^3\alpha_{21}^2\beta_{25} \\ & + \alpha_{11}^2\alpha_{23}\beta_{13} + \alpha_{21}^2\alpha_{23}\beta_{13} + \alpha_{11}^2\alpha_{13}\beta_{23} + \alpha_{21}^2\alpha_{13}\beta_{23} + 2\alpha_{21}^2\alpha_{23}\beta_{13} \\ & + 2\alpha_{11}^2\alpha_{13}\beta_{23} + 2\alpha_{21}\alpha_{11}\alpha_{13}\beta_{13} + 2\alpha_{11}\alpha_{21}\alpha_{23}\beta_{23} + \alpha_{25}\beta_{11} + \alpha_{15}\beta_{21}\end{aligned} \tag{2.25}$$

In order to reduce the magnitude of the 3rd and 5th order IMD products, magnitude of the γ_{13}, γ_{23}, γ_{15} and γ_{25} has to be reduced. Since the power amplifier's β coefficients can-not be controlled, the only way to reduce the magnitudes of the four γ coefficients is by proper adjustment of the predistorter's α coefficients.

2.3 Analysis of the System with an AM Signal

Using an AM input signal, this section shows how predistortion can reduce the 3rd and 5th order IMD products generated by the power amplifier. Start with a modulating signal of the form

$$V_m(t) = A \cdot \Re e\{\exp(j\omega_m t)\} \tag{2.26}$$

where A is the amplitude of the modulating signal. Using the modulating signal $V_m(t)$, a real bandpass AM signal $\tilde{V}_m(t)$ can be generated as

$$\begin{aligned}\tilde{V}_m(t) &= B(1 + V_m(t)) \cdot \Re e\{\exp(j\omega_c t)\} \\ &= B \cdot \Re e\{\exp(j\omega_c t)\} + AB \cdot \Re e\{\exp(j\omega_c t) \cdot \cos(\omega_m)t\}\end{aligned} \tag{2.27}$$

where B is the amplitude of the carrier. Next, the composite predistorter and power amplifier model from Figure 2.5 is represented in real bandpass signal form as illustrated in Figure 2.6.

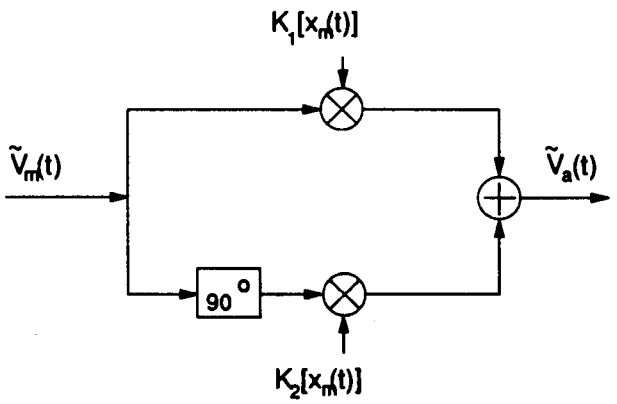

Figure 2.6. Composite Model in Real Bandpass Signal Form

The real bandpass signal $\tilde{V}_m(t)$ is now the input to the composite model in real bandpass form of Figure 2.6. Using the notation of Figure 2.6, the real bandpass output signal of the composite model becomes

$$\tilde{V}_a(t) = \tilde{V}_m(t)K_1[x_m(t)] + \hat{\tilde{V}}_m(t)K_2[x_m(t)] \tag{2.28}$$

where $\hat{\tilde{V}}$ is the real bandpass input signal $\tilde{V}_m(t)$ phase shifted by 90°. Using equations (2.17) and (2.18) for $K_1[x_m(t)]$ and $K_2[x_m(t)]$ respectively, it can be shown that the real bandpass output signal can be expressed as

$$\begin{aligned}
\tilde{V}_a(t) = {} & \Re e\left\{\left[\left(\gamma_{11}B + \frac{1}{2}\gamma_{13}A^2B + \frac{3}{8}\gamma_{15}A^4B\right) + j\left(\gamma_{21}B + \frac{1}{2}\gamma_{23}A^2B + \frac{3}{8}\gamma_{25}A^4B\right)\right]\cdot \exp(j\omega_c t)\right\} \\
& + \Re e\left\{\left[\left(\frac{1}{2}\gamma_{11}AB + \frac{3}{8}\gamma_{13}A^3B + \frac{5}{16}\gamma_{15}A^5B\right) + j\left(\frac{1}{2}\gamma_{21}AB + \frac{3}{8}\gamma_{23}A^3B + \frac{5}{16}\gamma_{25}A^5B\right)\right]\cdot \exp(j\omega_c t)\cdot 2\cos(\omega_m)t\right\} \\
& + \Re e\left\{\left[\left(\frac{1}{4}\gamma_{13}A^2B + \frac{1}{4}\gamma_{15}A^4B\right) + j\left(\frac{1}{4}\gamma_{23}A^2B + \frac{1}{4}\gamma_{25}A^4B\right)\right]\cdot \exp(j\omega_c t)\cdot 2\cos(2\omega_m)t\right\} \\
& + \Re e\left\{\left[\left(\frac{1}{8}\gamma_{13}A^3B + \frac{5}{32}\gamma_{15}A^5B\right) + j\left(\frac{1}{8}\gamma_{23}A^3B + \frac{5}{32}\gamma_{25}A^5B\right)\right]\cdot \exp(j\omega_c t)\cdot 2\cos(3\omega_m)t\right\}
\end{aligned} \tag{2.29}$$

The first and second terms of equation (2.29) denote the carrier and sidebands at the output of the power amplifier, respectively. The third and fourth terms of equation (2.29) represents the 3rd and 5th order IMD products of the power amplifier. Note that the 3rd and 5th order IMD products are functions of the γ_{13}, γ_{23}, γ_{15} and γ_{25} coefficients. In order to reduce the magnitude of the 3rd and 5th order IMD products, the magnitude of the last two terms of equation (2.29) has to be minimized, meaning that the magnitude of the γ coefficients has to be minimized. However, as shown in the previous section, the γ coefficients are functions of the α and β coefficients. Therefore, by selecting optimum α coefficients the magnitudes of the 3rd and 5th order IMD products can be reduced.

2.4 IMD Quadrature Demodulation Technique

This section describes the technique used to separate the 3rd and 5th order IMD products from the power amplifier's output spectrum so that the power in the out-of-band spillover generated by the power amplifier can be measured. Again, an AM signal is used to illustrate the separation process. The spectrum of the real bandpass input AM signal and the spectrum of the real bandpass AM signal generated by the power amplifier is shown in Figure 2.7.

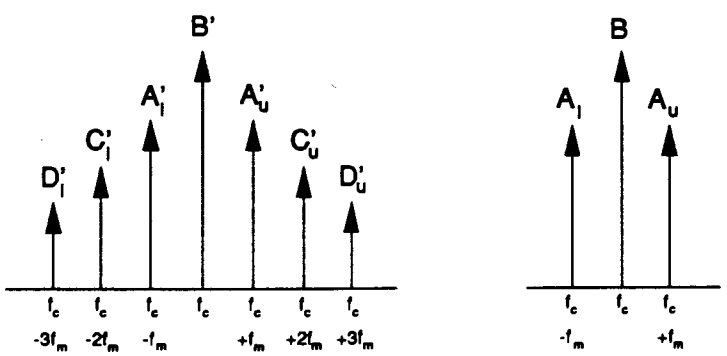

Figure 2.7. Spectra of Original and Amplified AM Signals

By performing a complex convolution on the two AM signals from Figure 2.7, one obtains the spectrum shown in Figure 2.8. Note that the 3rd order IMD product contributes to the signals at f_m, $2f_m$ and $3f_m$ Hz, while the 5th order IMD product contributes to the signals at $2f_m$, $3f_m$ and $4f_m$ Hz. However, at f_m Hz, the A'_uB and $B'A_l$ amplitudes dominate over the C'_uA_u amplitude. Also, at $2f_m$ Hz the C'_uB amplitude dominates over the A'_uA_l and D'_uA_u amplitudes. Similarly, at $3f_m$ Hz, D'_uB dominates over C'_uA_l.

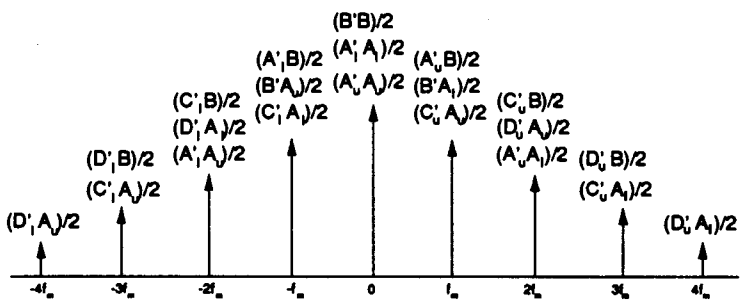

Figure 2.8. Spectrum of Complex Convolution

Therefore, by bandpass filtering the $2f_m$ and $3f_m$ signals and detecting the resulting power, one obtains the relative 3rd and 5th order IMD power generated by the power amplifier.

Next, let's examine the complex convolution result using the results of section 2.3. Start by rewriting equations (2.27) and (2.29) in a simpler form, respectively as,

$$\tilde{V}_m(t) = B \cdot \Re e\{e^{j\omega_c t}\} + AB \cdot \Re e\{e^{j\omega_c t} \cdot \cos(\omega_m)t\} \tag{2.30}$$

$$\begin{aligned}\tilde{V}_a(t) = {} & \Re e\{(\delta_{1i} + j\delta_{1q}) \cdot \exp(j\omega_c t)\} + \Re e\{(\delta_{2i} + j\delta_{2q}) \cdot \exp(j\omega_c t) \cdot 2\cos(\omega_m)t\} \\ & + \Re e\{(\delta_{3i} + j\delta_{3q}) \cdot \exp(j\omega_c t) \cdot 2\cos(2\omega_m)t\} \\ & + \Re e\{(\delta_{4i} + j\delta_{4q}) \cdot \exp(j\omega_c t) \cdot 2\cos(3\omega_m)t\}\end{aligned} \tag{2.31}$$

where the δ coefficients in equation (2.31) denote the power amplifier's in-phase and quadrature components. Recall that the four terms of equation (2.31) represent the carrier, sideband modulation, 3rd order IMD product and 5th order IMD product, respectively. Multiplying the real bandpass AM input signal, equation (2.30), with the carrier term of equation (2.31) produces

$$\tilde{V}_m(t) \cdot \Re e\{(\delta_{1i} + j\delta_{1q})e^{j\omega_c t}\} = \frac{B}{2}\delta_{1i} + \frac{A}{4}\delta_{1i}\cos(\omega_m)t + \frac{A}{4}\delta_{1i}\cos(-\omega_m)t \tag{2.32}$$

In equation (2.32), the components at higher frequencies are ignored for ease of representation. Note that there is no contribution from the quadrature component of the power amplifier. In order to obtain the contribution of the quadrature component of the power amplifier, the real bandpass input signal has to be passed through a 90° phase shifter. Multiplying the real bandpass AM input signal phase shifted by 90°, $\hat{V}_m(t)$, with the carrier term of equation (2.31) produces

$$\hat{V}_m(t) \cdot \Re e\{(\delta_{1i} + j\delta_{1q})e^{j\omega_c t}\} = \frac{B}{2}\delta_{1q} + \frac{A}{4}\delta_{1q}\cos(\omega_m)t + \frac{A}{4}\delta_{1q}\cos(-\omega_m)t \tag{2.33}$$

The higher frequency components are ignored in equation (2.33) for ease of representation. Observe that the result of equation (2.33) contains solely the contributions of the quadrature component of the power amplifier. Similarly, multiplication of the real bandpass AM input signal phase shifted by 90° with the last three terms of equation (2.31) generates the remaining quadrature component contributions.

Therefore, this analysis has shown that both the in-phase and quadrature contributions of the power amplifier can be produced by a quadrature demodulation process. A block diagram of the quadrature demodulation process is illustrated in Figure 2.8.

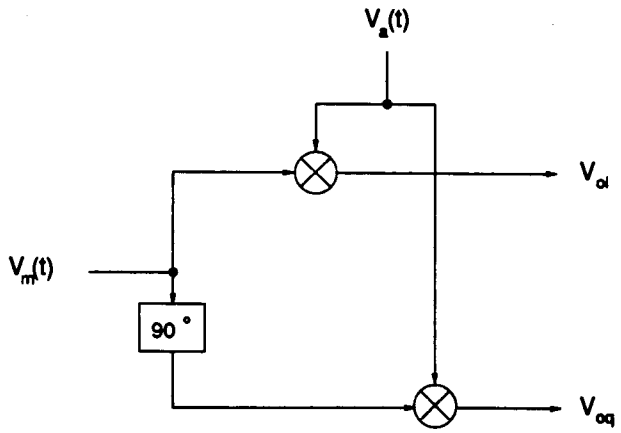

Figure 2.9. Block Diagram of IMD Quadrature Demodulator

In Figure 2.9, $V_{oi}(t)$ and $V_{oq}(t)$ denote the in-phase and quadrature demodulated signals, respectively.

3 OPTIMIZATION METHODS

There are two general categories for classification of optimization methods, direct search methods and gradient methods. This chapter presents an in-depth analysis of optimization techniques from both categories. Specifically, Hooke and Jeeves' method, steepest descent technique, Newton's method, and Davidon-Fletcher-Powell method are examined.

3.1 Direct Search Methods

Direct search methods are used in unconstrained minimization problems. The direct search methods are in general robust methods and they only require the evaluation of the function that is to be minimized.

3.1.1 Hooke and Jeeves Method

Hooke and Jeeves method is a pattern search method that falls in the group of direct search methods. Hooke and Jeeves method consists of exploratory steps and pattern moves about a base point. Given an initial starting point, exploratory steps are performed, one coordinate at a time, in order to acquire information about the local behavior of the function that is to be minimized. It is obvious that explorations can be performed until the minimum is found, but this approach would be very inefficient. Instead, Hooke and Jeeves suggested that the exploratory steps be followed by pattern moves along the approximate gradient direction [13].

Consider the function $F(\mathbf{x})$ where $\mathbf{x} = (x_1, x_2, \ldots, x_n)$. Given a starting point $\mathbf{x}^k$, explorations are performed in all coordinates of $\mathbf{x}^k$ until a temporary point $\mathbf{x}^{k+1}$ is obtained such that $F(\mathbf{x}^{k+1}) < F(\mathbf{x}^k)$. A pattern move is now performed along the approximate gradient direction $\mathbf{s}^k = \mathbf{x}^{k+1} - \mathbf{x}^k$. Taken the direction $\mathbf{s}^k$ into account, the pattern point $\mathbf{x}^{k+2}$ is given by

$$\mathbf{x}^{k+2} = \mathbf{x}^{k+1} + \mathbf{s}^k \tag{3.1}$$

The process continues with alternating exploration steps and pattern moves until the function minimum is found. The Hooke and Jeeves iteration process is as follows [14]:

i) set $k = 0$; given initial base point $\mathbf{x}^0$, evaluate $F(\mathbf{x}^0)$

ii) perform an exploration about $\mathbf{x}^k$ and obtain a temporary $\mathbf{x}^{k+1}$

iii) if $F(\mathbf{x}^{k+1}) < F(\mathbf{x}^k)$ accept $\mathbf{x}^{k+1}$ as the new base point; else if $\lambda > \tau$ (τ is a predetermined λ_{min}), the function minimum is$\mathbf{x}^k$; else decrease λ and return to step ii)

iv) calculate pattern point $\mathbf{x}^{k+2} = \mathbf{x}^{k+1} + \mathbf{s}^k = 2\mathbf{x}^{k+1} - \mathbf{x}^k$ and evaluate $F(\mathbf{x}^{k+2})$

v) explore pattern point $\mathbf{x}^{k+2}$ and obtain a temporary point $\mathbf{x}^{k+3}$

vi) if $F(\mathbf{x}^{k+3}) < F(\mathbf{x}^{k+1})$ accept $\mathbf{x}^{k+3}$ as the new base point; else if $\lambda > \tau$, the function minimum is $\mathbf{x}^{k+1}$; else decrease λ, set $k = k + 1$, and return to step ii)

As mentioned earlier, Hooke and Jeeves' method has a slow convergence rate, but at the same time it is a robust method and it eventually converges to the function minimum.

3.2 Gradient Methods

The gradient methods are different from the direct search methods, in that descent directions are generated at each step. To evaluate the descent directions, the first and for some methods the second derivatives have to be computed at each step. The evaluation of the derivatives denotes an increase in the computation performed to find the descent directions, but at the same time it denotes a faster convergence. Some gradient techniques make use of previous information in finding the direction of descent which further improves the accuracy of the descent steps.

Every descent technique is made up of three general parts. First step is to find a direction of descent $\mathbf{s}^k$. Second, a descent steplength λ^k is calculated. Finally, using the direction of descent and the descent steplength, the descent step $\mathbf{x}^{k+1} = \mathbf{x}^k + \lambda^k \mathbf{s}^k$ can be calculated [13]. The descent techniques vary in the way the direction of descent is computed. The following subsections examine three different descent techniques.

3.2.1 Steepest Descent Technique

In order to select the descent direction, the gradient of the function has to be evaluated. One important property of the gradient is that if $F(\mathbf{x})$ is a differentiable function, then for any point $\mathbf{x}^k$, the vector $-\nabla F(\mathbf{x}^k)$ will point in the direction of most rapid decrease of $F(\mathbf{x}^k)$ [15]. Using this gradient property, the french mathematician Cauchy suggested that the descent direction be

$$\mathbf{s}^k = -\nabla F(\mathbf{x}^k) \tag{3.2}$$

Having the value of the descent direction, the next step is to find a descent steplength λ^k. There are two alternatives for the computation of the descent steplength. One could use the optimal step alternative which finds a λ^k such that $F(\mathbf{x}^k + \lambda^k \mathbf{s}^k) = \min_{\lambda} F(\mathbf{x}^k + \lambda^k \mathbf{s}^k)$. The second choice is to use the non-optimal step alternative which finds a λ^k such that $F(\mathbf{x}^k + \lambda^k \mathbf{s}^k) \leq F(\mathbf{x}^k)$. In order to speed the rate of convergence, the non-optimal step alternative will be used. The iteration steps for finding λ^k are [13]:

i) set $\lambda^k = \lambda_{start}$

ii) evaluate $F(\mathbf{x}^k + \lambda^k \mathbf{s}^k)$

iii) if $F(\mathbf{x}^k + \lambda^k \mathbf{s}^k) < F(\mathbf{x}^k)$ set $\lambda_{start} = \lambda^k$; otherwise reduce λ^k by 1/2 and repeat from step ii)

Note that by keeping track of the current λ^k value, memory is added to the steepest descent technique, since the starting value for λ^{k+1} will be λ^k.

The iteration steps for the steepest descent technique are [13]:

i) start with k = 0; given $\mathbf{x}^0$ calculate $F(\mathbf{x}^0)$

ii) calculate the gradient $\nabla F(\mathbf{x}^k)$

iii) calculate the current descent vector $\mathbf{s}^k = -\nabla F(\mathbf{x}^k)$. Normalize $\mathbf{s}^k$ such that $\| \mathbf{s}^k \| = 1$.

iv) find the descent step length λ^k such that $F(\mathbf{x}^k + \lambda^k \mathbf{s}^k) < F(\mathbf{x}^k)$

v) perform the current descent step $\mathbf{x}^{k+1} = \mathbf{x}^k + \lambda^k \mathbf{s}^k$

vi) evaluate $F(\mathbf{x}^{k+1})$

vii) if $F(\mathbf{x}^{k+1}) - F(\mathbf{x}^k) < \varepsilon_1$ (where ε_1 is a predetermined tolerance) terminate the process; otherwise, proceed to step viii).

viii) accept the new point $\mathbf{x}^{k+1}$, set $k = k + 1$, and repeat from step ii).

The steepest descent technique is a relatively simple technique, but it possesses a few disadvantages. First, the rate of convergence is slow due to the fact that each iteration step is locally optimal and thus the global properties of the function are not exploited. Also, perturbations resulting from round-off error in the computer can cause incorrect descent directions to be computed [14].

Since consecutive descent direction are orthogonal, the rate of convergence can be increased by setting $\mathbf{s}^k = \mathbf{x}^k - \mathbf{x}^{k-2}$ for $k \geq 2$. This acceleration technique was developed by Forsythe and Motzkin [13].

3.2.2 Newton's Method

Newton's method was developed on the assumption that the function $F(\mathbf{x})$ to be minimized can be approximated by a quadratic function. Start by assuming that the function $F(\mathbf{x})$ to be minimized is a twice continuously differentiable function. Then, the function $F(\mathbf{x})$ can be approximated by a quadratic function, $F_k(\mathbf{x})$, obtained by writing a second order Taylor series expansion about $\mathbf{x}^k$ as [13]

$$F_k(\mathbf{x}) = F(\mathbf{x}^k) + \nabla F(\mathbf{x}^k) \cdot (\mathbf{x} - \mathbf{x}^k) + \frac{1}{2}(\mathbf{x} - \mathbf{x}^k) \cdot H(\mathbf{x}^k)(\mathbf{x} - \mathbf{x}^k) \tag{3.3}$$

where $H(\mathbf{x}^k)$ is the Hessian matrix at the point $\mathbf{x}^k$. Note that the Hessian matrix is symmetric and positive definite. The definition of positive definiteness states that if a matrix H is an n x n symmetric matrix, then it is positive definite if $\mathbf{x} \cdot H\mathbf{x} > 0$ for all $\mathbf{x} \in R^n, \mathbf{x} \neq 0$.

Having the approximate function $F_k(\mathbf{x})$, the next step is to select $\mathbf{x}^{k+1}$ which minimizes the approximate function $F_k(\mathbf{x})$. In doing this, the following expression is obtained

$$\nabla F_k(\mathbf{x}^{k+1}) = \nabla F(\mathbf{x}^k) + H(\mathbf{x}^k)(\mathbf{x}^{k+1} - \mathbf{x}^k) = 0 \tag{3.4}$$

Rearranging equation (3.4) the recurrence formula for Newton's method becomes

$$\mathbf{x}^{k+1} = \mathbf{x}^k - [H(\mathbf{x}^k)]^{-1}\nabla F(\mathbf{x}^k) \tag{3.5}$$

From equation (3.5) it can be seen that the descent direction $\mathbf{s}^k$ is given by

$$\mathbf{s}^k = -[H(\mathbf{x}^k)]^{-1}\nabla F(\mathbf{x}^k) \tag{3.6}$$

Indeed, $\mathbf{s}^k$ is a descent direction since the directional derivative $(\mathbf{s}^k)^T\nabla F(\mathbf{x}^k)$ is negative, as shown by the relation

$$(\mathbf{s}^k)^T\nabla F(\mathbf{x}^k) = -[\nabla F(\mathbf{x}^k)]^T [H(\mathbf{x}^k)]^{-1}\nabla F(\mathbf{x}^k) < 0$$

The iteration process for Newton's method is as follows [13]:

i) start with k = 0; given $\mathbf{x}^0$ calculate $F(\mathbf{x}^0)$

ii) calculate the gradient $\nabla F(\mathbf{x}^k)$

iii) calculate the Hessian matrix $H(\mathbf{x}^k)$

iv) evaluate $\mathbf{s}^k$ by solving $H(\mathbf{x}^k)\mathbf{s}^k = -\nabla F(\mathbf{x}^k)$ and normalize $\mathbf{s}^k$ such that $\|\mathbf{s}^k\| = 1$

v) compute the directional derivative; if $(\mathbf{s}^k)^T\nabla F(\mathbf{x}^k) \geq 0$ set $\mathbf{s}^k = -\mathbf{s}^k$

vi) find the descent step length λ^k such that $F(\mathbf{x}^k + \lambda^k\mathbf{s}^k) < F(\mathbf{x}^k)$

vii) perform the current descent step $\mathbf{x}^{k+1} = \mathbf{x}^k + \lambda^k\mathbf{s}^k$

viii) evaluate $F(\mathbf{x}^{k+1})$

ix) if $F(\mathbf{x}^{k+1}) - F(\mathbf{x}^k) < \varepsilon_1$ (where ε_1 is a predetermined tolerance) terminate the process; otherwise, proceed to step x).

x) accept the new point $\mathbf{x}^{k+1}$, set $k = k + 1$, and repeat from step ii).

Just like Newton's method for univariate functions, Newton's method applied to multivariate functions has a fast convergence rate as long as the initial starting point is close to the global minimum and the function $F(\mathbf{x})$ to be minimized is close to the form of a quadratic. The drawback of Newton's method is the large amount of computation power needed for the

evaluation of the second order derivatives [15]. The computation power is greatly increased in cases where analytical expressions are not available and numerical differentiation has to be performed.

3.2.3 Davidon-Fletcher-Powell (DFP) Method

As discussed in the previous two gradient methods, the main computational power is used to evaluate function, gradient, and Hessian matrix values. Out of these three values, the evaluation of the Hessian matrix values is the most costly. The method developed to avoid the repeated computation of the Hessian matrix is Broyden's method. Again, the assumption is that the function $F(\mathbf{x})$ to be minimized is a twice continuously differentiable function. Broyden's method defines a linear function

$$l_k(\mathbf{x}) = \nabla F(\mathbf{x}^k) + D_k(\mathbf{x} - \mathbf{x}^k) \tag{3.7}$$

which approximates the function $F(\mathbf{x})$. Note that equation (3.7) is comparable with equation (3.5), the difference being that the Hessian matrix of equation (3.5) is replaced by the matrix D_k in equation (3.7). D_k is a positive definite n x n matrix that approximates the Hessian matrix.

To obtain $\mathbf{x}^{(k+1)}$, the linear system $l_k(\mathbf{x}) = 0$ is solved and the following recurrence formula is obtained.

$$\mathbf{x}^{k+1} = \mathbf{x}^k - D_k^{-1}\nabla F(\mathbf{x}^k) \tag{3.8}$$

Let me now explain how the matrix D_k is evaluated. In practice, the identity matrix I_n is usually chosen as the initial D_0 matrix. At every subsequent step k, the initial identity matrix is updated in a fashion so that the matrix D_k approximates the Hessian matrix. The derivation of the formula used to update the D_k matrix starts by making use of the Secant method.

Consider the function $g(x) = \nabla F(x)$ (i.e. function of one variable case). Knowing two points $A = (x^{k-1}, g(x^{k-1}))$ and $B = (x^k, g(x^k))$, the linear approximation of $g(x)$ passing through the points A and B is

$$l_k(x) = g(x^k) + D_k(x - x^k) \tag{3.9}$$

Point $C = (x^{k+1}, g(x^{k+1}))$ can be found by solving $l_k(x) = 0$. Now, the linear approximation of $g(x)$ passing through the points B and C is

$$l_{k+1}(x) = g(x^{k+1}) + D_{k+1}(x - x^{k+1}) \tag{3.10}$$

Equation (3.10) can be applied to the n dimensional space, yielding

$$l_{k+1}(\mathbf{x}) = g(\mathbf{x}^{k+1}) + D_{k+1}(\mathbf{x} - \mathbf{x}^{k+1}) \tag{3.11}$$

Note that D_{k+1} is selected such that $l_{k+1}(\mathbf{x}^k) = g(\mathbf{x}^k)$. Applying this to equation (3.11) generates the Secant condition

$$D_{k+1}(\mathbf{x}^{k+1} - \mathbf{x}^k) = g(\mathbf{x}^{k+1}) - g(\mathbf{x}^k) \tag{3.12}$$

which has to be satisfied by the proper selection of D_{k+1}. To compute D_{k+1}, we start by writing

$$D_{k+1} = D_k + (D_{k+1} - D_k) = D_k + U_k \tag{3.13}$$

where U_k is the update matrix. Let $U_k = \mathbf{a}^k \cdot (\mathbf{b}^k)^T$ (where $\mathbf{a}^k$ and $\mathbf{b}^k$ are column vectors). Substituting equation (3.13) into (3.12) produces

$$D_k(\mathbf{x}^{k+1} - \mathbf{x}^k) + (\mathbf{x}^k \cdot (\mathbf{b}^k)^T)(\mathbf{x}^{k+1} - \mathbf{x}^k) = g(\mathbf{x}^{k+1}) - g(\mathbf{x}^k) \tag{3.14}$$

from which

$$\mathbf{a}^k = \frac{g(\mathbf{x}^{k+1}) - g(\mathbf{x}^k) - D_k(\mathbf{x}^{k+1} - \mathbf{x}^k)}{(\mathbf{b}^k)^T \cdot (\mathbf{x}^{k+1} - \mathbf{x}^k)} = f(\mathbf{b}^k) \tag{3.15}$$

Equation (3.15) shows that in order to compute the update matrix U_k, all is left to do is to find the value of $\mathbf{b}_k$. To find $\mathbf{b}_k$, start by examining the difference

$$l_{k+1}(\mathbf{x}) - l_k(\mathbf{x}) = g(\mathbf{x}^{k+1}) - g(\mathbf{x}^k) - D_{k+1}(\mathbf{x}^{k+1} - \mathbf{x}^k) + U_k(\mathbf{x} - \mathbf{x}^k) \tag{3.16}$$

The Secant condition of equation (3.12) states that

$$g(\mathbf{x}^{k+1}) - g(\mathbf{x}^k) - D_{k+1}(\mathbf{x}^{k+1} - \mathbf{x}^k) = 0$$

hence,

$$l_{k+1}(\mathbf{x}) - l_k(\mathbf{x}) = (\mathbf{b}^k)^T \cdot (\mathbf{x} - \mathbf{x}^k)\mathbf{a}^k \tag{3.17}$$

Broyden's method requires that the two linear approximation equations $l_k(\mathbf{x})$ and $l_{k+1}(\mathbf{x})$ be equal. This requirement applied to equation (3.17) generates

$$(\mathbf{b}^k)^T \cdot (\mathbf{x} - \mathbf{x}^k)\mathbf{a}^k = 0 \tag{3.18}$$

Equation (3.18) is satisfied when $\mathbf{b}^k$ is orthogonal to $\mathbf{x} - \mathbf{x}^k$. The selection of $\mathbf{b}^k = \mathbf{x}^{k+1} - \mathbf{x}^k$ satisfies equation (3.18) since $(\mathbf{x}^{k+1} - \mathbf{x}^k) \cdot (\mathbf{x} - \mathbf{x}^k) = 0$ as a result of the $l_k(\mathbf{x}) = l_{k+1}(\mathbf{x})$ requirement.

Finally, the value of the update matrix U_k can be evaluated since both $\mathbf{a}^k$ and $\mathbf{b}^k$ values are known

$$\mathbf{b}^k = \mathbf{x}^{k+1} - \mathbf{x}^k$$

$$\mathbf{a}^k = \frac{g(\mathbf{x}^{k+1}) - g(\mathbf{x}^k) - D_k\mathbf{b}^k}{(\mathbf{b}^k)^T \cdot \mathbf{b}^k}$$

As shown by equation (3.13), knowing the value of the update matrix, implies that the value of the D_{k+1} matrix is also known. Broyden's method can now be applied (i.e. the recurrence formula of equation (3.8)) to minimize the function $F(\mathbf{x})$.

One disadvantage of Broyden's method lies in the computation needed to evaluate D_k^{-1}. A second disadvantage of Broyden's method is that if D_{k+1} is positive definite, the Secant condition can't be satisfied [15]. The DFP method avoids the computational disadvantage by satisfying the inverse Secant condition

$$D_{k+1}\mathbf{y}^k = \mathbf{d}^k \tag{3.19}$$

where $\mathbf{y}^k = g(\mathbf{x}^{k+1}) - g(\mathbf{x}^k)$ and $\mathbf{d}^k = \mathbf{x}^{k+1} - \mathbf{x}^k$. Hence, the DFP method updates the inverse of the D_k matrix. The recurrence formula for the DFP method becomes

$$\mathbf{x}^{k+1} = \mathbf{x}^k - D_k \nabla F(\mathbf{x}^k) \tag{3.20}$$

To get around the second disadvantage of Broyden's method, the DFP method uses

$$D_{k+1} = D_k + \alpha_k(\mathbf{a}^k \cdot (\mathbf{a}^k)^T) + \beta_k(\mathbf{b}^k \cdot (\mathbf{b}^k)^T) \tag{3.21}$$

for update of the D_{k+1} matrix. To find the α_k and β_k coefficients, apply the inverse Secant condition (3.19) to (3.21) to obtain

$$\mathbf{d}^k = D_k\mathbf{y}^k + \alpha_k(\mathbf{a}^k \cdot (\mathbf{a}^k)^T)\mathbf{y}^k + \beta_k(\mathbf{b}^k \cdot (\mathbf{b}^k)^T)\mathbf{y}^k \tag{3.22}$$

Setting $\mathbf{a}^k = \mathbf{d}^k$ and $\mathbf{b}^k = D_k\mathbf{y}^k$ yields

$$\mathbf{d}^k - D_k\mathbf{y}^k = \alpha_k(\mathbf{d}^k \cdot (\mathbf{d}^k)^T)\mathbf{y}^k + \beta_k\left((D_k\mathbf{y}^k) \cdot (D_k\mathbf{y}^k)^T\right)\mathbf{y}^k \tag{3.23}$$

Equation (3.23) is satisfied if

$$\alpha_k(\mathbf{d}^k)^T \cdot \mathbf{y}^k = 1 \quad \Rightarrow \quad \alpha_k = \frac{1}{(\mathbf{d}^k)^T \cdot \mathbf{y}^k}$$

$$\beta_k(\mathbf{y}^k)^T D_k \mathbf{y}^k = -1 \quad \Rightarrow \quad \beta_k = -\frac{1}{(\mathbf{y}^k)^T D_k \mathbf{y}^k}$$

Therefore, the D_{k+1} update equation for the DFP method becomes

$$D_{k+1} = D_k + \frac{\mathbf{d}^k \cdot (\mathbf{d}^k)^T}{(\mathbf{d}^k)^T \cdot \mathbf{y}^k} - \frac{(D_k \mathbf{y}^k) \cdot (D_k \mathbf{y}^k)^T}{(\mathbf{y}^k)^T D_k \mathbf{y}^k} \tag{3.24}$$

The iteration process for the DFP method is as follows [13]:

i) start with $k = 0$; given $\mathbf{x}^0$ calculate $F(\mathbf{x}^0)$

ii) calculate the gradient $\nabla F(\mathbf{x}^k)$

iii) compute the approximating Hessian matrix D_k; start with $D_0 = I_n$ (where I_n is the n x n identity matrix). For subsequent steps update the D_k matrix using

$$D_k = D_{k-1} + \frac{\mathbf{d}^{k-1} \cdot (\mathbf{d}^{k-1})^T}{(\mathbf{d}^{k-1})^T \cdot \mathbf{y}^{k-1}} - \frac{\left(D_{k-1}\mathbf{y}^{k-1}\right) \cdot \left(D_{k-1}\mathbf{y}^{k-1}\right)^T}{(\mathbf{y}^{k-1})^T D_k \mathbf{y}^{k-1}}$$

where $\mathbf{d}^{k-1} = \mathbf{x}^k - \mathbf{x}^{k-1}$ and $\mathbf{y}^{k-1} = \nabla F(\mathbf{x}^k) - \nabla F(\mathbf{x}^{k-1})$

iv) evaluate $\mathbf{s}^k$ by solving $\mathbf{s}^k = -D_k \nabla F(\mathbf{x}^k)$ and normalize $\mathbf{s}^k$ such that $\| \mathbf{s}^k \| = 1$

v) compute the directional derivative; if $(\mathbf{s}^k)^T \nabla F(\mathbf{x}^k) \geq 0$ set $\mathbf{s}^k = -\mathbf{s}^k$. Also set the $D_k = I_n$ since the D_k is no longer positive definite.

vi) find the descent step length λ^k such that $F(\mathbf{x}^k + \lambda^k \mathbf{s}^k) < F(\mathbf{x}^k)$

vii) perform the current descent step $\mathbf{x}^{k+1} = \mathbf{x}^k + \lambda^k \mathbf{s}^k$

viii) evaluate $F(\mathbf{x}^{k+1})$

ix) if $F(\mathbf{x}^{k+1}) - F(\mathbf{x}^k) < \varepsilon_1$ (where ε_1 is a predetermined tolerance) terminate the process; otherwise, proceed to step x).

x) accept the new point $\mathbf{x}^{k+1}$, set $k = k + 1$, and repeat from step ii).

4 PREDISTORTER SIMULATION

So far, Chapter 2 of this thesis provided the mathematical background on the reduction of the 3rd and 5th order IMD products of a power amplifier. Also, Chapter 3 described several optimization techniques that can be used to adaptively minimize the power amplifier's out-of-band power. Next step is to simulate the performance of the adaptive predistorter. This chapter describes the simulation model used and it discusses the simulation results obtained for various optimization techniques.

4.1 Power Amplifier Characterization

As mentioned in Chapter 1, high power efficiency is desirable for mobile communication applications. Class AB power amplifiers offer a high power efficiency at the expense of a decrease in linearity. One could generate higher IMD products by operating the power amplifier in the nonlinear region, hence being able to show a reduction in the IMD products as a result of adaptive predistortion. The AM-AM and AM-PM nonlinearities of an 800 MHz, 5 Watt, class AB power amplifier were measured and are shown in Figure 4.1.

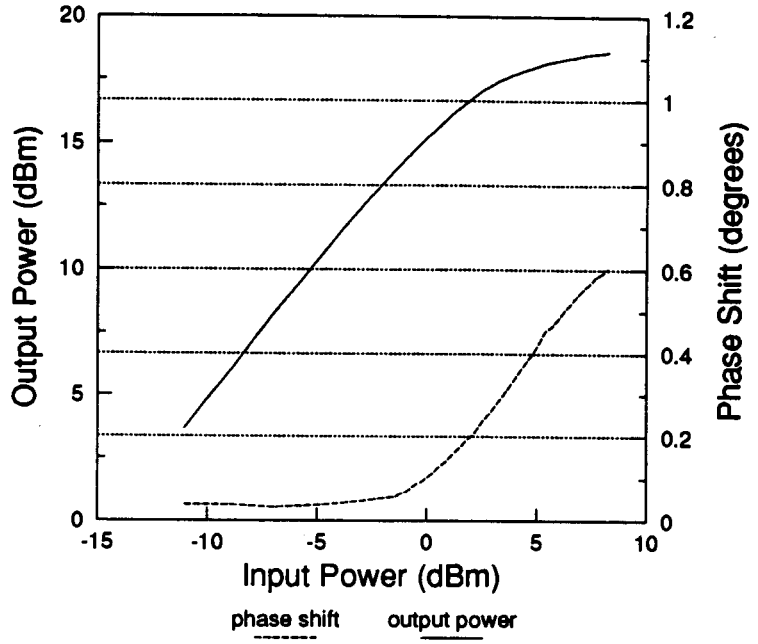

Figure 4.1. AM-AM and AM-PM Characteristics of a Class AB Power Amplifier

The complex gain of the class AB power amplifier was derived from the AM-AM and AM-PM measurements and is shown in Figure 4.2.

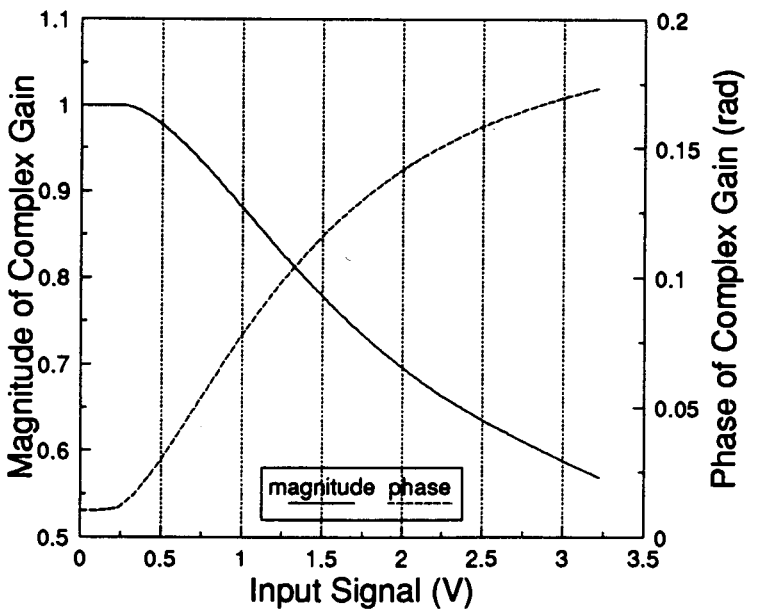

Figure 4.2. Complex Gain of the Class AB Power Amplifier

Next, the complex gain of the predistorter, corresponding to the characteristics of the class AB power amplifier, were found using the composite complex gain model described in section 2.2. Based on Figure 2.4, the composite gain is

$$F[x_m(t)] \cdot G[x_m(t) \cdot |F[x_m(t)]|^2] = K_1 \tag{4.1}$$

where $x_m(t)=|V_m(t)|^2$, and K_1 is the desired constant magnitude of the composite gain. The complex gain of the predistorter is found by solving equation (4.1) for discrete values of the complex gain. Then, to obtain the F_1 and F_2 functions, the real and imaginary parts of the predistorter's complex gain were interpolated by two 2nd order polynomials using a least squares approximation. For a K_1 of 0.9, the measured and interpolated F_1 and F_2 functions are illustrated in Figures 4.3 and 4.4.

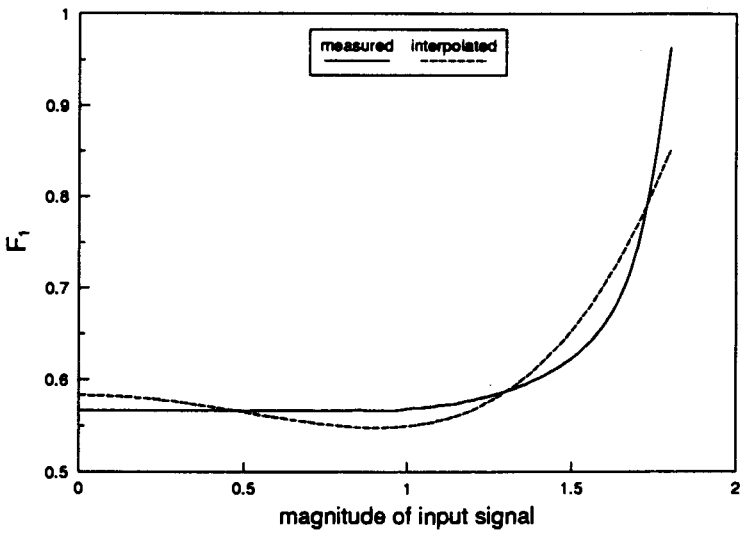

Figure 4.3. Measured and Interpolated F_1 Function

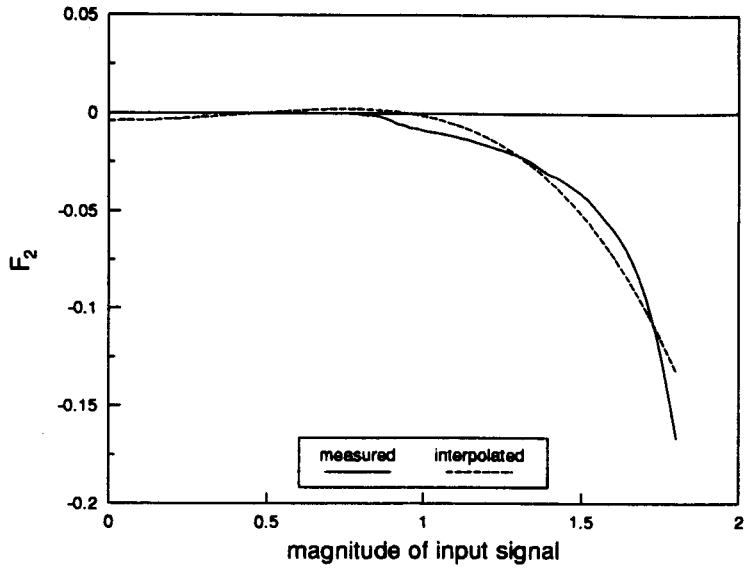

Figure 4.4. Measured and Interpolated F_2 Function

The interpolating equations for the F_1 and F_2 functions are

$$F_1[x_m(t)] = 0.58315 - 0.08498 \cdot x_m(t) + 0.05169 \cdot x_m^2(t) \tag{4.2}$$

$$F_2[x_m(t)] = -0.00395 + 0.0214 \cdot x_m(t) - 0.01887 \cdot x_m^2(t)$$

Note that the F_1 and F_2 functions of equation (4.2) were obtained so as to find the gain coefficients, α_{11} and α_{21}. The remaining four α coefficients will only be used as initial estimates. The adaptation algorithms will find the optimum values for the nonlinear coefficients.

4.2 Simulation Model

The model used to simulate the adaptive predistorter linearizer is shown in Figure 4.5.

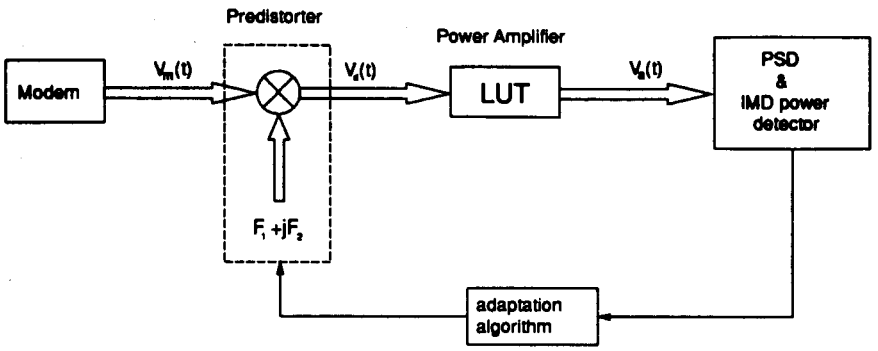

Figure 4.5. Simulation Model

The simulation was performed using a 16 QAM input signal. A raised cosine pulse with a roll-off of 0.5, Hamming windowed to seven symbols, was used for the pulse shape of the transmit filter. Using a_k as the symbol sequence, T as the symbol rate and g(t) as the pulse shape of the transmit filter, the complex envelope of the 16 QAM bandpass input signal can be expressed as

$$V_m(t) = \sum_{k=-\infty}^{\infty} a_k g(t - nT) \tag{4.3}$$

As illustrated in Figure 4.5, the predistorter is implemented using the complex gain model. The predistorted signal $V_d(t)$ is the result of the complex multiplication between the complex 16 QAM vectors and the complex gain of the predistorter $F[x_m(t)]$.

The power amplifier is represented by a look-up-table (LUT). The LUT contains 1000 entries of the power amplifier's complex gain (magnitude and phase) as a function of input power. As described in the previous section, the power amplifier's complex gain was derived from the AM-AM and AM-PM measurements. Based on the magnitude of each predistorted vector, the corresponding complex gain of the power amplifier is extracted from the LUT. Note that if the corresponding entry is not found in the LUT, the simulation interpolates between two adjacent entries to find the power amplifier's complex gain.

Each predistorted complex vector is multiplied by its matching complex gain vector $G[x_d(t)]$, generating the power amplifier's output complex vector. Next, the PSD of the power amplifier's output signal is evaluated. Having found the PSD, all the points above a reference level of -65 dBc in the bandwidth $|f_H - f_L|$ are averaged to obtain the average power of the IMD products, IM_o. The low frequency cut-off f_L is equal to the bandwidth of the 16 QAM signal and the high frequency cut-off f_H is selected to ensure that the 3rd and 5th order IMD products are included. The PSD and power evaluator module was written by Kandola [16]. The adaptation algorithm adjusts the coefficients of the predistorter's complex gain so as to minimize the IM_o power value.

4.2.1 Uncertainty in the IM_o Evaluation

The optimization methods will minimize the power amplifier's out-of-band power based on the IM_o power value, meaning that no analytic function is available. Therefore, the accuracy of the IM_o power value is crucial to the convergence of the adaptation algorithms especially for the gradient techniques where the gradients will be calculated using numerical methods (i.e. secant method). An experiment was performed to find the uncertainty in the evaluation of the IM_o power value. The IM_o power value was evaluated 100 times for a particular set of α coefficients. This procedure was repeated for different number of symbols ranging from 5,000 to 30,000. The results of this experiment are shown in Figure 4.6.

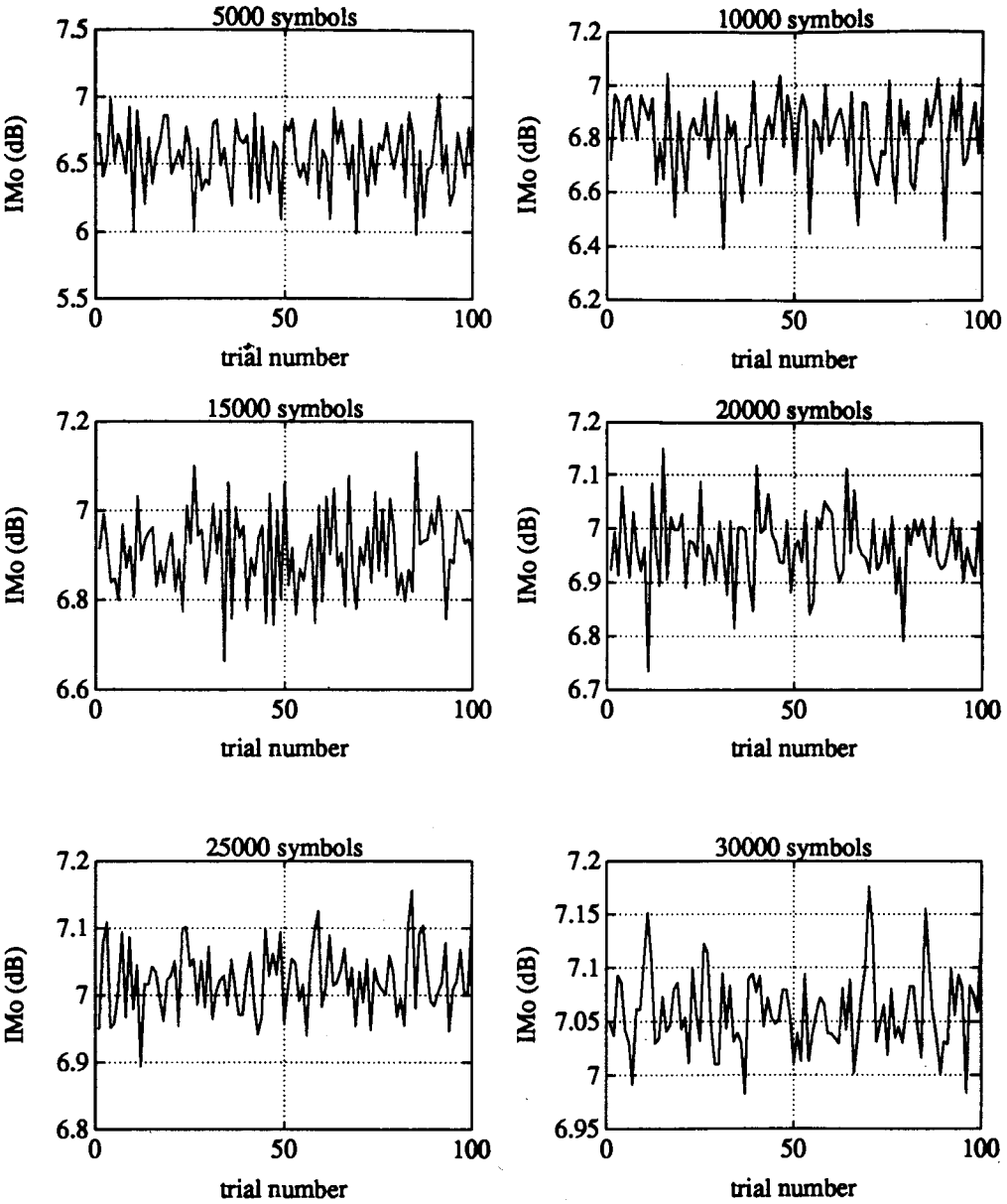

Figure 4.6. IMo Measurements for 5000 to 30000 Symbols

The minimum, maximum, mean and variance for each set of measurements were calculated and the results are summarized in Table 4.1.

Table 4.1. Statistic Results of IM_o Evaluation

# of symbols	5000	10000	15000	20000	25000	30000
# of trials	100	100	100	100	100	100
Minimum	5.977	6.3915	6.6637	6.7344	6.8932	6.9816
Mean	6.5484	6.8122	6.9091	6.9657	7.0223	7.0595
Maximum	7.021	7.0461	7.1299	7.1495	7.1557	7.1759
Variance	0.2429	0.1428	0.0911	0.0686	0.0500	0.0371

As shown in Table 4.1, the higher the number of symbols the higher the accuracy of the IM_o power value. A trade-off has to be made between the desired accuracy and the convergence rate, since the higher the number of symbols, the longer it takes to evaluate the IM_o power values, hence, the longer it takes the adaptation algorithm to converge to the optimum coefficients for minimum IMD products.

4.2.2 Relationship Between the α Coefficients and IM_o Power Value

It was shown by Kandola [16] that the IM_o power value has a quadratic dependence on the α_3 and α_5 coefficients. It is desirable for the IM_o power value to have a quadratic dependence on the α coefficients, since the adaptation algorithms can find the optimum coefficients (i.e. lowest IM_o power value) with ease.

To examine the relationship between the α_3 coefficients and the IM_o power value, the α_5 coefficients were set to their optimum values and the α_{13} and α_{23} are varied, evaluating the IM_o value every time a coefficient was altered. Similarly, by keeping the α_3 coefficients constants and varying α_{15} and α_{25} the relationship between the IM_o power value and the α_5 coefficients was found. For every IM_o power value evaluation 10,000 symbols were processed. The surface and corresponding contour plots for the α_3 and α_5 planes are shown in Figures 4.7 to 4.10.

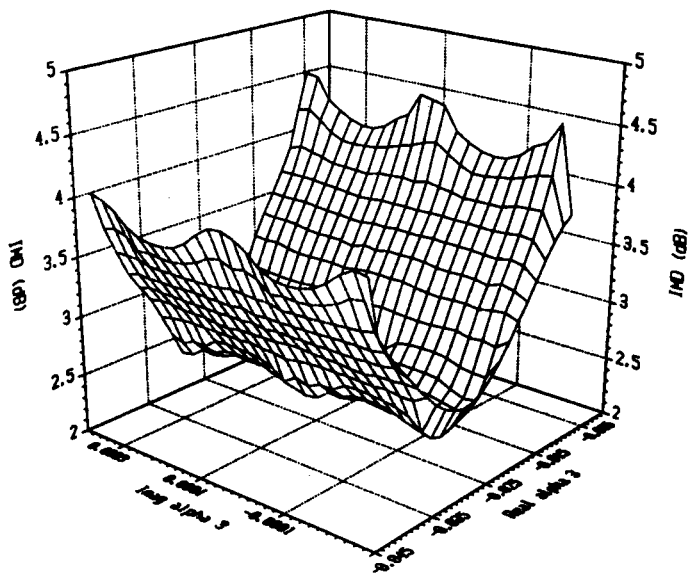

Figure 4.7. Simulated Surface Plot of α_3 Plane

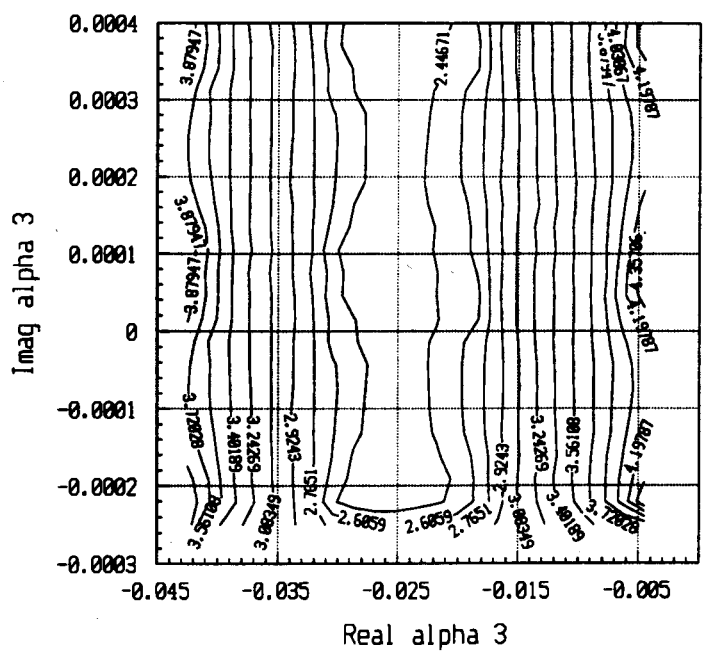

Figure 4.8. Simulated Contour Plot of α_3 Plane

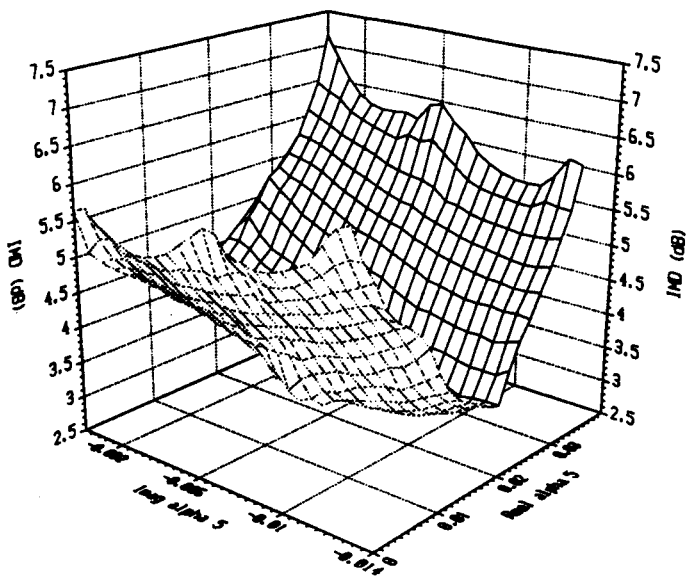

Figure 4.9. Simulated Surface Plot of α_5 Plane

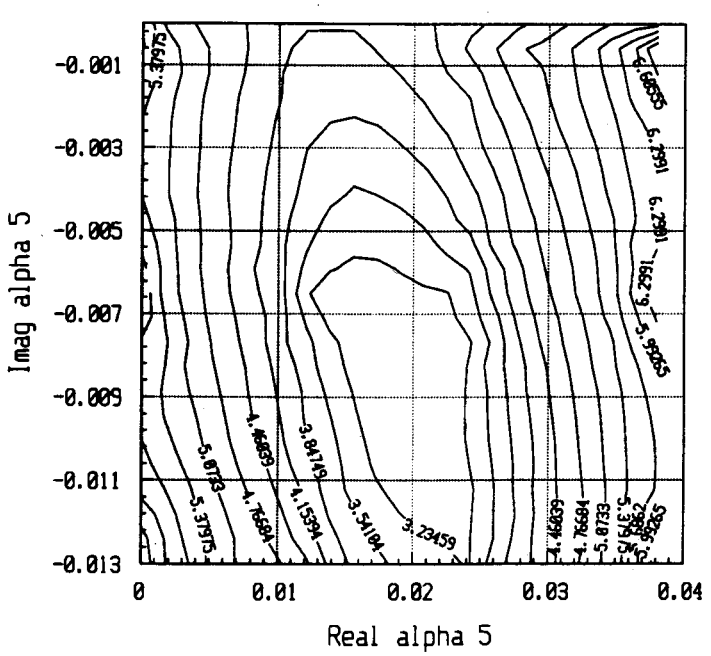

Figure 4.10. Simulated Contour Plot of α_5 Plane

The surface plots, Figures 4.7 and 4.9, reflect a quadratic behavior of the IM_o power value as a function of the α_3 and α_5 coefficients. This agrees with the theoretical results derived by Kandola [16], which showed the quadratic dependence of the α coefficients on the IM_o power value.

4.3 Simulation Results

This section presents the simulation results obtained for Hooke and Jeeves method, steepest descent technique, Newton's method and DFP method. The results to be presented were obtained performing four variable optimization. This is referred to as optimization in four dimensions (4D). It is possible to perform the optimization in two dimensions (2D). In this case, the α_3 coefficients are optimized while the α_5 coefficients are kept constant. Then the α_3 coefficients are kept at their newly found temporary optimum values, and the α_5 coefficients are optimized. This process is repeated until the global minimum IM_o power value is found. It was found by experimentation that the alternating 2D optimization has to process considerably more symbols than the 4D optimization, hence its convergence time is greatly increased.

4.3.1 Hooke and Jeeves Method

Hooke and Jeeves' algorithm was implemented as described by the pseudocode of section 3.1.1. Three stopping conditions were used to stop Hooke and Jeeves optimization. First, if the exploration step sizes were decreased below preset limits, $\mathbf{k}_{min}$, the optimization stops. Second, if no $\mathbf{x}^{k+1}$ is found such that $F(\mathbf{x}^{k+1}) \leq F(\mathbf{x}^k)$ the optimization stops. As shown in section 4.2.1 the uncertainty in the IM_o power value could affect the rate of convergence. Since 10,000 symbols were processed for evaluating each IM_o power value, $|F(\mathbf{x}^{k+1} - F(\mathbf{x}^k)| < \varepsilon$, where ε is a preset tolerance that takes the variance for 10,000 symbols into account, was used as the third stopping condition.

At the start of the optimization, all the α_3 and α_5 coefficients were initialized to zero (i.e. no predistortion). Figures 4.11 and 4.12 show the convergence of the four α coefficients and the convergence of the IM_0 power value, respectively.

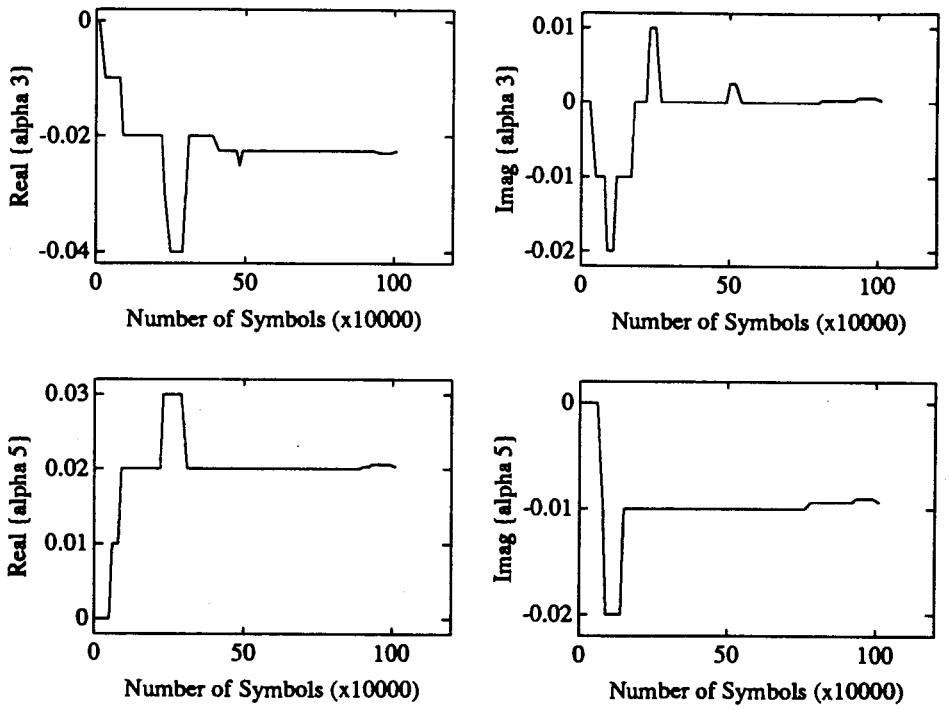

Figure 4.11. Coefficient Convergence for Hooke and Jeeves' Method

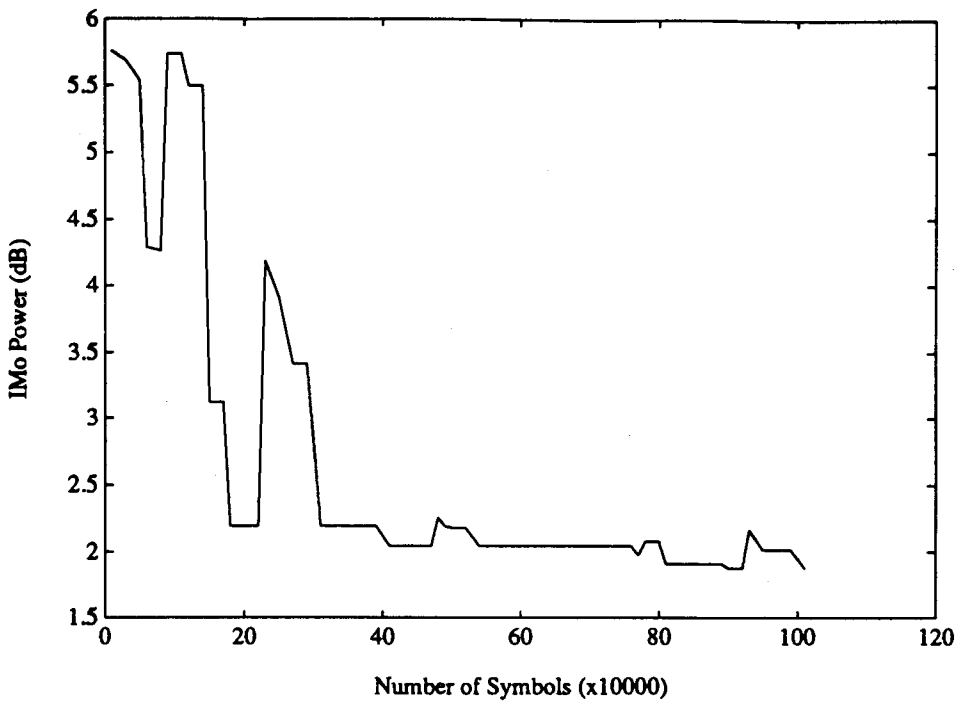

Figure 4.12. IMo Power Value Convergence for Hooke and Jeeves' Method

The total number of symbols that have to be processed by Hooke and Jeeves method before the optimum coefficients yielding the lowest IM_o power value are found is 1,010,000 symbols. To show the reduction in the power amplifier's out-of-band emissions, the PSD of the power amplifier's output without predistortion and with the optimum coefficients found by Hooke and Jeeves' optimization are illustrated in Figure 4.13.

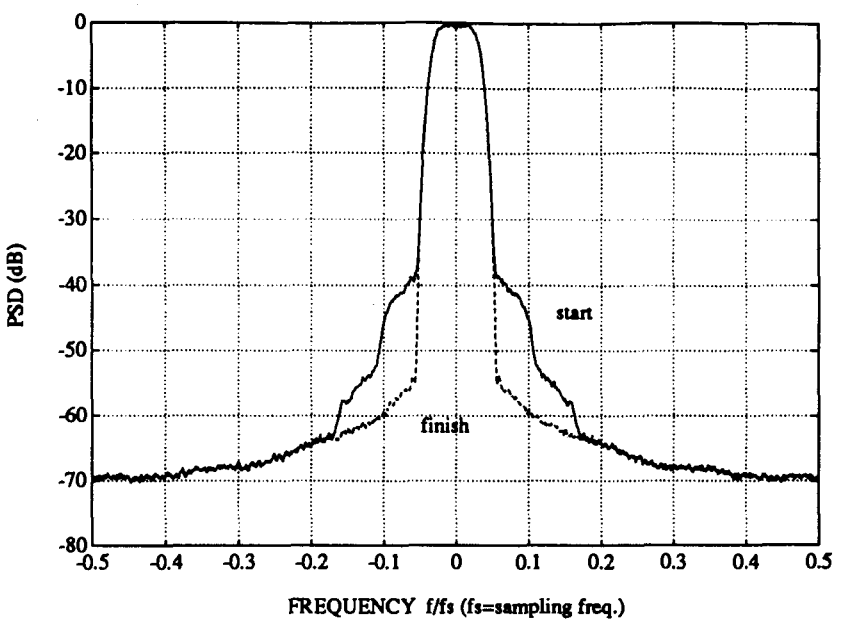

Figure 4.13. PSD for 16 QAM Input Signal Before and After Hooke and Jeeves Optimization

The optimum predistorter nonlinear functions found by the Hooke and Jeeves' method are

$$F_1[x_m(t)] = 0.58315 - 0.0225x_m(t) + 0.0203125x_m^2(t)$$

$$F_2[x_m(t)] = -0.00395 + 0.0003125x_m(t) - 0.009375x_m^2(t)$$

4.3.2 Steepest Descent Technique

The gradients needed by the steepest descent technique were calculated using the secant method approximation. Therefore, the value of the step size, h, used by the secant method to approximate the gradient has to be large enough to ensure that the uncertainty in the IM_o power value does not affect the accuracy of the gradient.

The number of symbols to be processed for each IM_o power value evaluation is set to 10,000 at the beginning of the optimization. The value of the step size h, is reduced and the number of symbols is doubled once the IM_o power value is less than 4 dB. This is done so as to

reduce the uncertainty in the IM_o power value and to increase the accuracy of the gradient evaluations. The stopping criteria are similar to the Hooke and Jeeves' stopping criteria with the exception that a lower limit is now set on the descent steplength λ^k.

Again the α coefficients were initialized to zero (i.e. no predistortion) at the start of the optimization. Figures 4.14 and 4.15 show the convergence of the four α coefficients and the convergence of the IM_o power value, respectively.

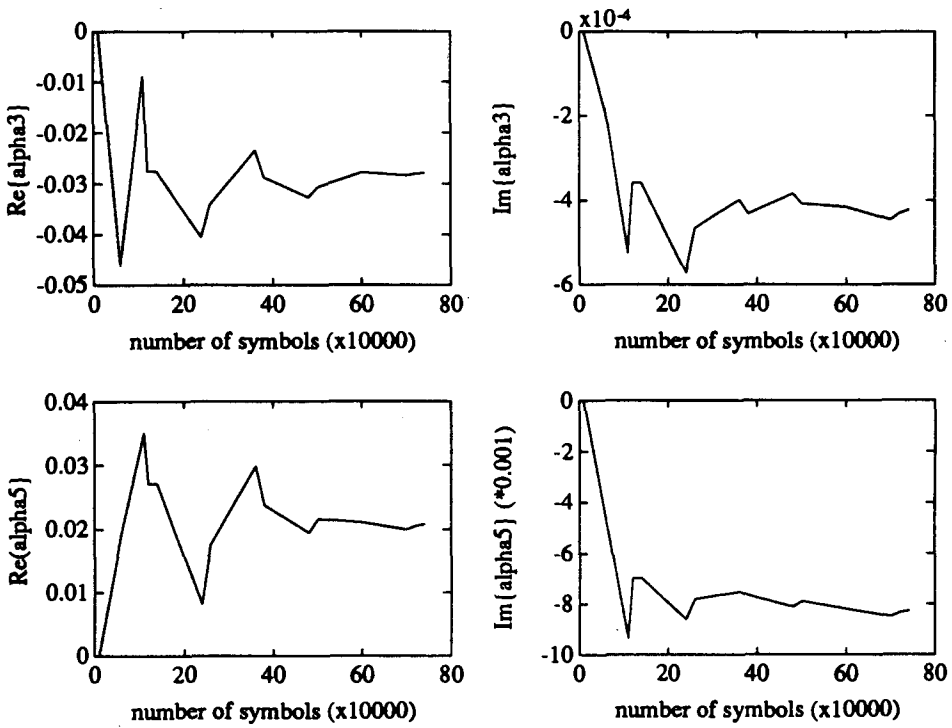

Figure 4.14. Coefficient Convergence for Steepest Descent Technique

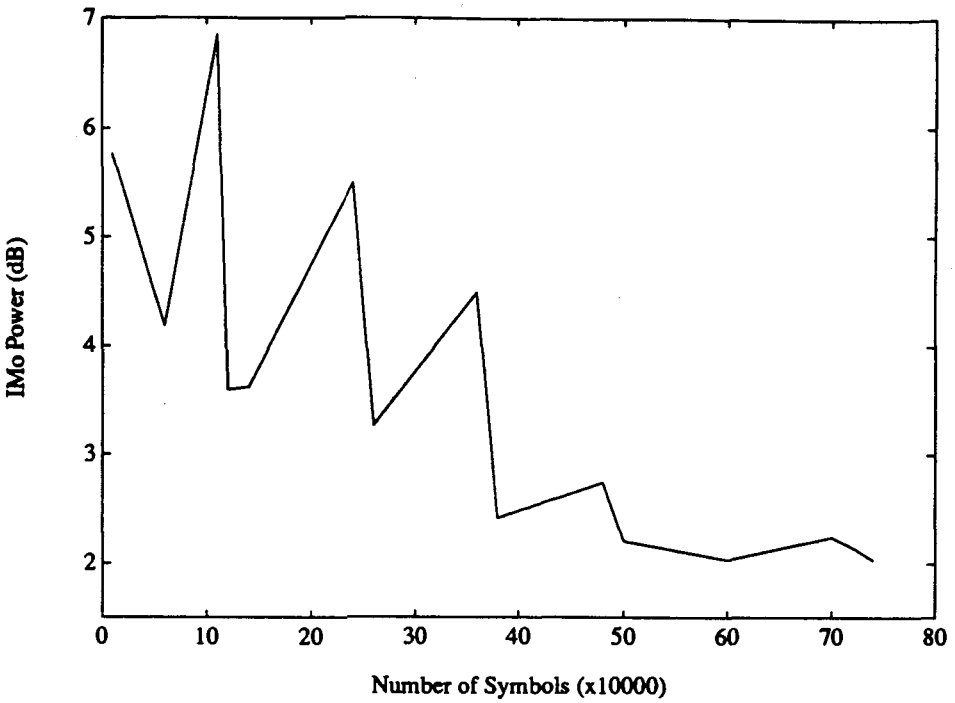

Figure 4.15. IMo Power Value Convergence for Steepest Descent Technique

The total number of symbols that have to be processed by the steepest descent technique before the optimum coefficients yielding the lowest IM_o power value are found is 740,000 symbols. To show the reduction in the power amplifier's out-of-band emissions, the PSD of the power amplifier's output without predistortion and with the optimum coefficients found by steepest descent optimization are illustrated in Figure 4.16.

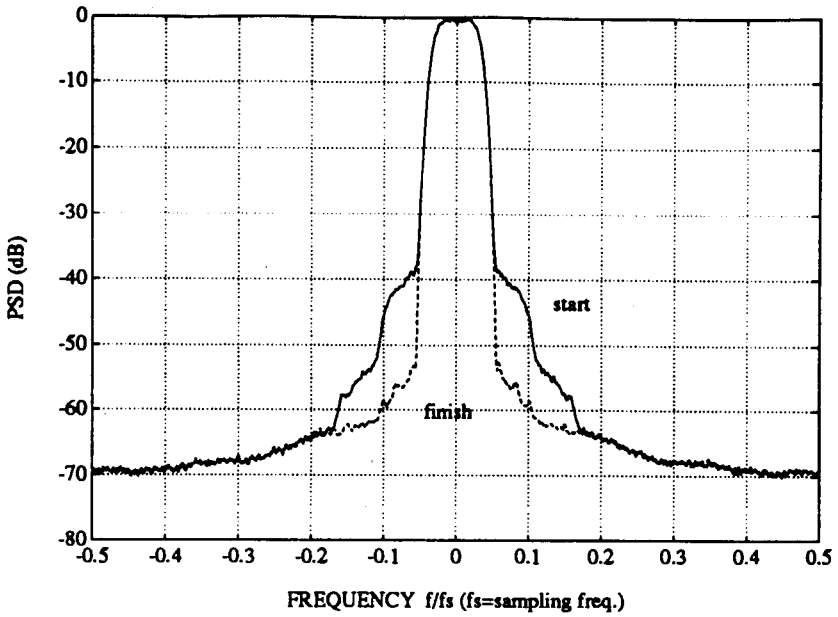

Figure 4.16. PSD for 16 QAM Input Signal Before and After Steepest Descent Optimization

The optimum predistorter nonlinear functions found by the steepest descent method are

$$F_1[x_m(t)] = 0.58315 - 0.0278546x_m(t) + 0.02076919x_m^2(t)$$

$$F_2[x_m(t)] = -0.00395 - 0.00042359x_m(t) - 0.00827705x_m^2(t)$$

4.3.3 Newton's Method

As described in section 3.2.2, Newton's method requires the computation of second order derivatives. Using the secant method to approximate the derivatives proved to be inadequate in this case since the uncertainty of the IM_o power value made it impossible to obtain accurate approximations. As a result of this, results showing the convergence of the four α coefficients and the convergence of the IM_o power value could not be obtained.

However, one could still use Newton's method to reduce the IM_o power value. By collecting data in the α_3 and α_5 planes, a relationship between the α coefficients and the IM_o power level can be found. Hence, two functions of the form

$$P(x,y) = Ax^2 + By^2 + Cx + Dy + Exy + F$$

can be fitted to the α_3 and α_5 plane data, respectively, using a least squares fit. Newton's method can now be applied to the two analytic functions. The two functions fitted to the data collected for the α_3 and α_5 planes are

$$P(\alpha_{13}, \alpha_{23}) = 1.066 \cdot 10^5 \alpha_{13}^2 + 2.486 \cdot 10^5 \alpha_{23}^2 - 92\alpha_{13} - 1.734 \cdot 10^3 \alpha_{23} - 7.515 \cdot 10^4 \alpha_{13}\alpha_{23} + 12$$

$$P(\alpha_{15}, \alpha_{25}) = 4.865 \cdot 10^8 \alpha_{13}^2 + 5.281 \cdot 10^8 \alpha_{25}^2 + 4.275 \cdot 10^4 \alpha_{15} + 7.236 \cdot 10^4 \alpha_{25} - 8.042 \cdot 10^3 \alpha_{15}\alpha_{25} + 12$$

The relationship between the α coefficients and the IM_o power level can be used to obtain a more accurate starting approximation of the Hessian matrix used by the DFP method, hence, increasing the rate of convergence. Recall that the identity matrix is used as the starting approximation of the Hessian matrix in the DFP method.

4.3.4 Davidon-Fletcher-Powell (DFP) Method

The secant method was used again to approximate the needed gradient values. The value of the step size, h, proved to be critical, just like for the case of the steepest descent technique. The feature that was added to the DFP method, was to make the step size, h, dependent on the current α coefficient (i.e. $h = 20\% \cdot \alpha$). The stopping criteria are exactly the same as the stopping criteria for the steepest descent technique. Also, the optimization was initialized to process 10,000 symbols for each IM_o power evaluation. The step size, h, is reduced by a factor of 1/2 and the number of symbols is doubled when the IM_o power values becomes less than 4 dB.

Just like for the previous two optimization methods, the α coefficients were initialized to zero (i.e. no predistortion) at the start of the optimization. Figures 4.17 and 4.18 show the convergence of the four α coefficients and the convergence of the IM_o power value, respectively.

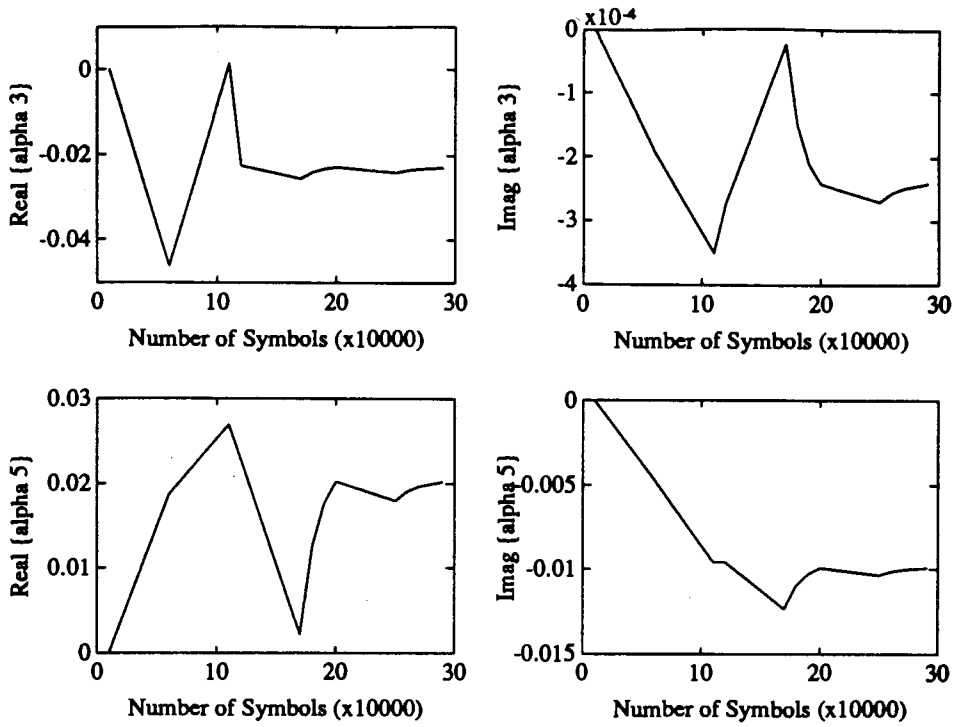

Figure 4.17. Coefficient Convergence for the DFP Optimization

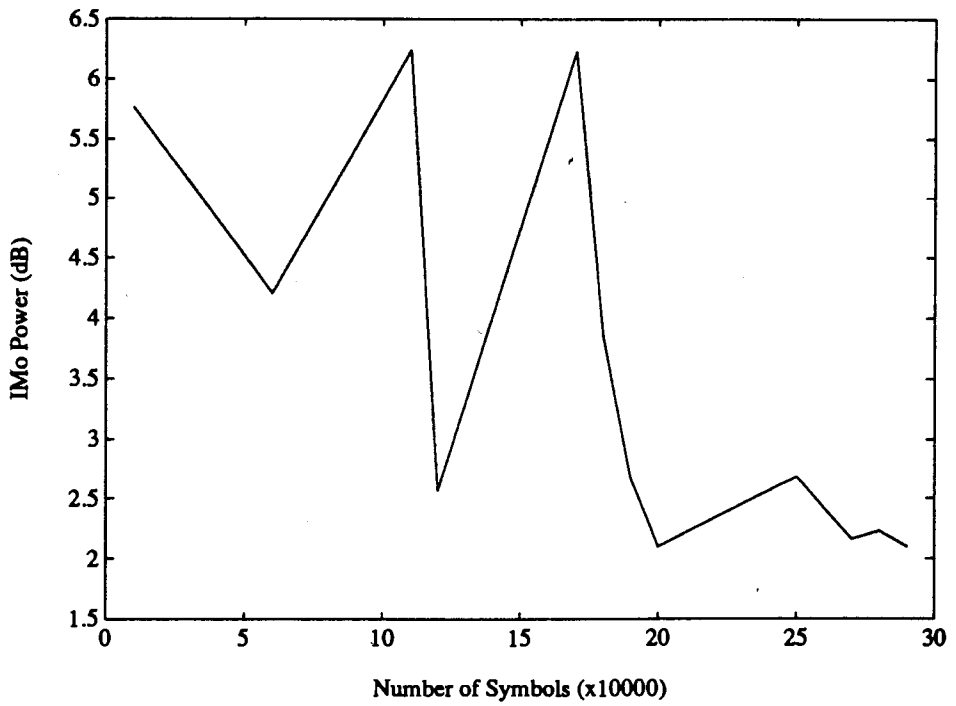

Figure 4.18. IMo Power Value Convergence for the DFP Optimization

The total number of symbols that have to be processed by the DFP method before the optimum coefficients yielding the lowest IM_o power value are found is 290,000 symbols. To show the reduction in the power amplifier's out-of-band emissions, the PSD of the power amplifier's output without predistortion and with the optimum coefficients found by the DFP optimization are illustrated in Figure 4.19.

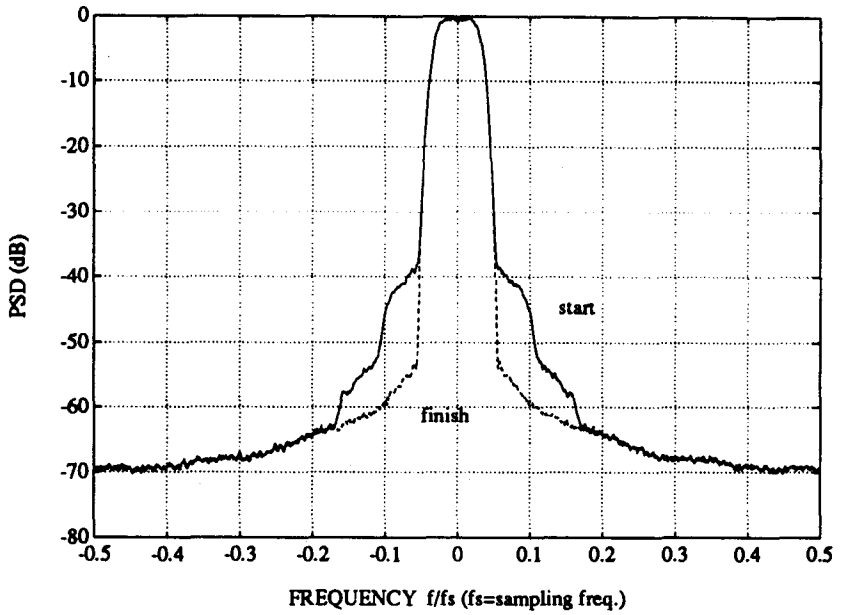

Figure 4.19. PSD for 16 QAM Input Signal Before and After the DFP Optimization

The optimum predistorter nonlinear functions found by the DFP method are

$$F_1[x_m(t)] = 0.58315 - 0.02279744x_m(t) + 0.02026443x_m^2(t)$$

$$F_2[x_m(t)] = -0.00395 - 0.00024035x_m(t) - 0.00991707x_m^2(t)$$

4.4 Comparison of Simulation Results

To compare the performance of the Hooke and Jeeves, steepest descent and DFP optimization methods, a graph of the IM_o power value convergence versus the number of symbols processed was plotted. This time, only the IM_o power values after pattern moves were indicated, not showing the exploration steps. The plot comparing the convergence of the Hooke and Jeeves,

steepest descent and DFP optimization methods is presented in Figure 4.20. Note that all the results were obtained having the power amplifier operate at a 6 dB output back-off, OBO, power. The OBO power is evaluated using $OBO=10\log(P_{sat}/P_{av})$, where P_{av} is the average amplifier output power for the entire simulation.

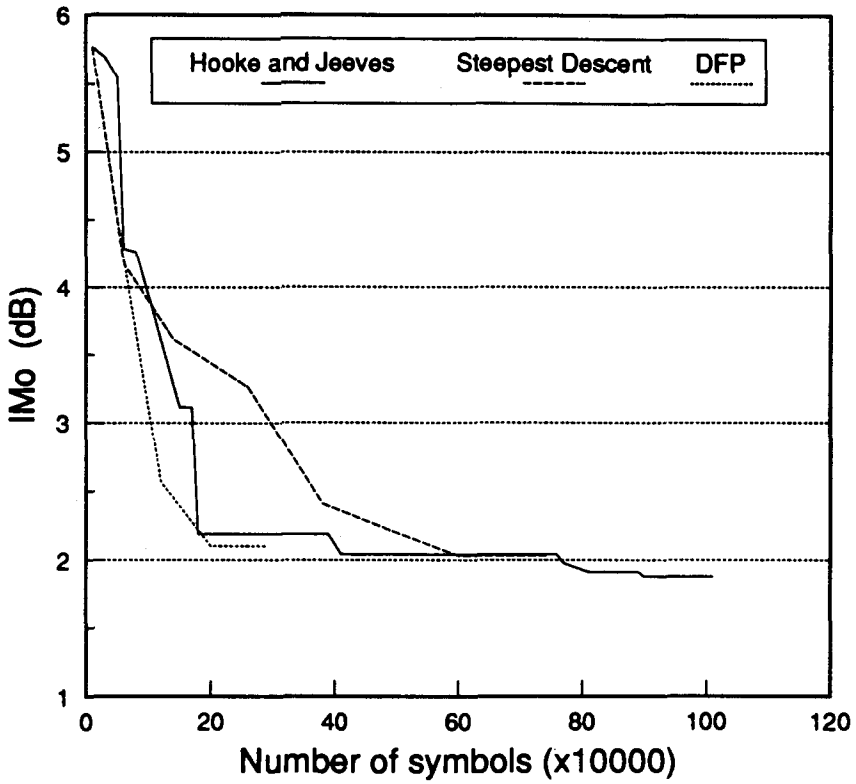

Figure 4.20. Convergence Comparison Plot

As illustrated in Figure 4.20, the DFP technique possesses the fastest convergence rate, finding the minimum IM_o power value after processing 290,000 symbols. Steepest descent technique has the second fastest convergence rate needing to process 740,000 symbols before the minimum IM_o power value was found. Hooke and Jeeves' method has the slowest convergence, needing to process 1,010,000 symbols in order to find the minimum IM_o power value.

Recall that in order to use Newton's method analytical functions for the α_3 and α_5 planes have to be found. For a rough approximation of the two functions, at least 100 IM_o power values have to be computed in each plane. At 10,000 symbols processed per IM_o power value

evaluation, 2,000,000 symbols have to be processed in total. Since Hooke and Jeeves' method has the slowest convergence rate (i.e. needs 1,010,000 symbols) out of the other three optimization methods, it is obvious that fitting functions to the α_3 and α_5 planes so that Newton's method could be used is not a good approach, unless prior knowledge of the approximate coefficients is known.

To further show the increased convergence rate of the DFP method over the Hooke and Jeeves' and steepest descent methods, a plot showing the PSD at the power amplifier's output after 120,000 processed symbols is illustrated in Figure 4.21. As seen from Figure 4.21, the Hooke and Jeeves and steepest descent optimization methods reduce the out-of-band power skirts by 8 dB, while the DFP method reduces the out-of-band power skirts by almost 13 dB. This clearly indicates the increased convergence rate of the DFP method.

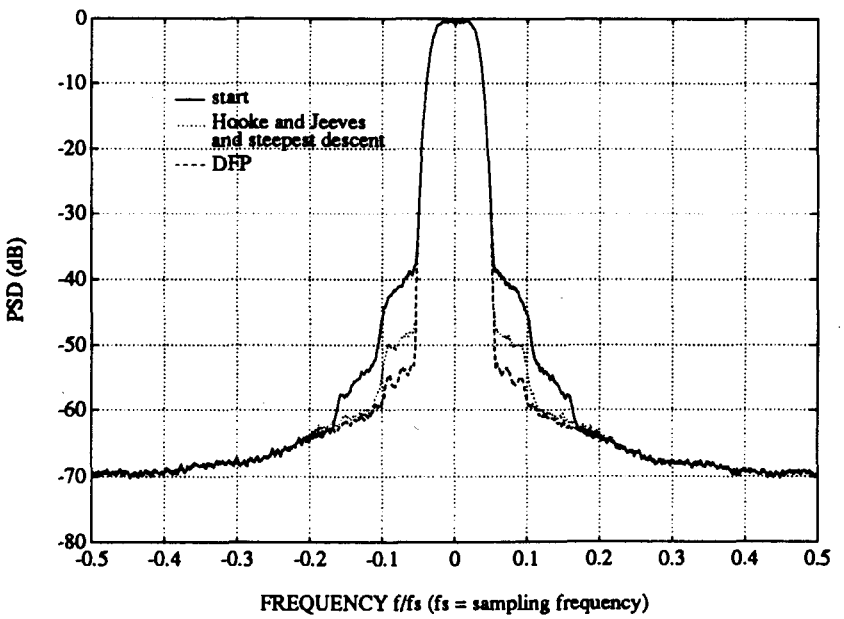

Figure 4.21. PSD After 120,000 Symbols

The difference between the power amplifier's output PSD obtained by using Hooke and Jeeves', steepest descent and DFP optimization methods is almost unnoticeable as shown by Figure 4.22.

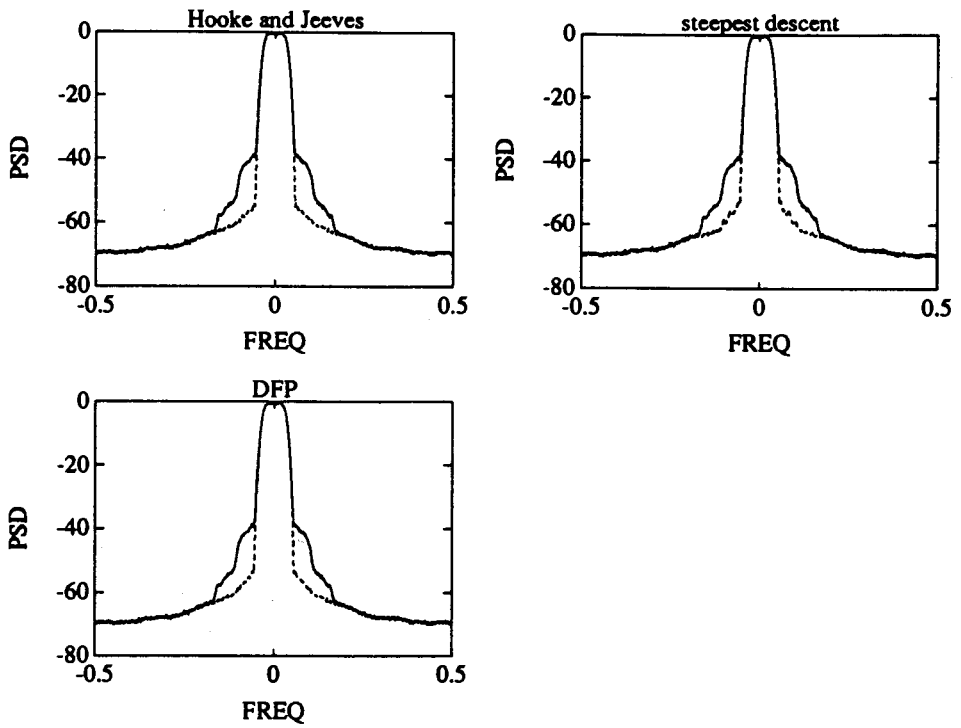

Figure 4.22. PSD at Beginning and End of Optimizations

A plot showing the spectra at the input of the power amplifier and at the output of the power amplifier without and with predistortion is illustrated in Figure 4.23.

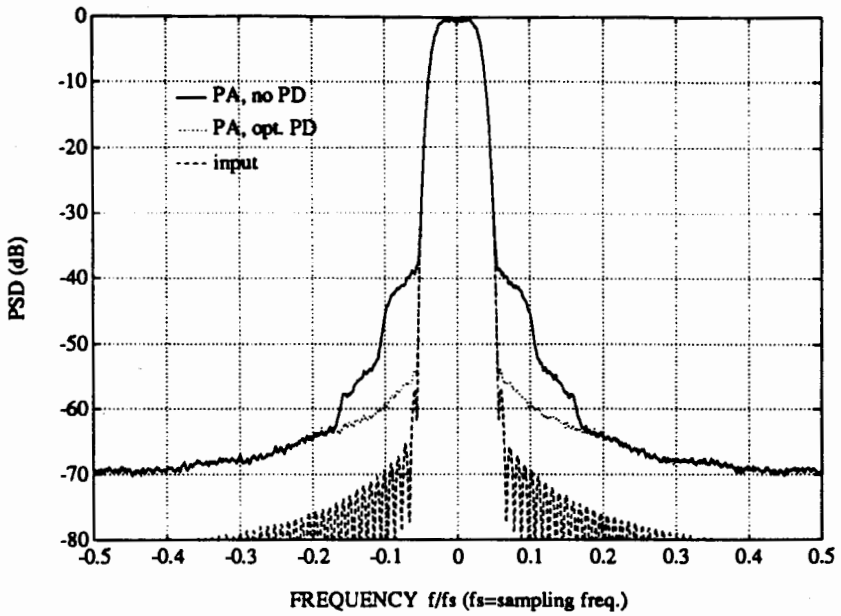

Figure 4.23. PSD at the Input and Output of the Power Amplifier

Note that as a result of the optimizations, a reduction of 15 dB in the power amplifier's IMD skirts was obtained. Overall, the simulated optimization results show that Hooke and Jeeves, steepest descent and DFP methods converge to the minimum IM_o power value and that adaptive predistortion could lower the power amplifier's IMD skirts.

5 HARDWARE IMPLEMENTATION

Having presented the simulation results for the adaptive predistorter in the previous chapter, this chapter outlines the design and implementation of the adaptive analog predistorter. A TMS320 digital signal processing (DSP) board was already being used as an OQPSK modulator. An additional software routine enabled the DSP board to generate the 16 QAM signal needed for the testing of the adaptive predistorter. A raised cosine pulse with a roll-off of 0.33, Kaiser windowed to 7 symbols, was used for the pulse shape of the transmit filter. The achievable data rate for the 16 QAM signal with the TMS320 is 62.5 kbit/second.

5.1 Predistorter

The predistorter module is made up of a quadrature modulator and two second order nonlinear functions. The block diagram is illustrated in Figure 5.1.

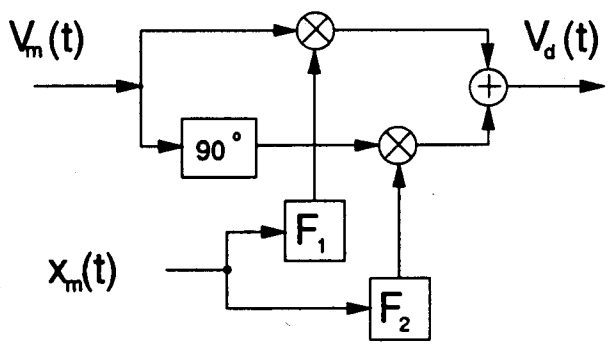

Figure 5.1. Block Diagram of Predistorter

A quadrature modulator operating in the 55-90 MHz frequency range was used. The manufacturer's specifications for the quadrature modulator are shown in Table 5.1.

Table 5.1. Manufacturer's Specifications for the Quadrature Modulator

Insertion Loss max.	10 dB
VSWR nominal	1.8 : 1
Impedance nominal	50 Ω
Null Depth min.	50 dB
Bias Voltages	±15 V DC ±1%, 8 mA max.
Control Range Linear Range	±10 V @ 10 mA ±2 V
Modulation Frequency	DC to 100 kHz
RF Level max.	+10 dBm
Temperature Range	0°C to +70°C

The F_1 and F_2 functions were implemented using operational amplifiers (op amps) and linear four-quadrant multipliers. Given an input signal x, F(x) is implemented using nested multiplication as $F(x)=\alpha_1+x(\alpha_3+\alpha_5 x)$. Nested multiplication, reduces the number of components needed to implement the F_1 and F_2 functions. Figure 5.2 shows a block diagram of the circuit configuration for the F_1 and F_2 functions. Note that the input signal, denoted by x in the above equation, is actually the magnitude squared of the I and Q channels (i.e I^2+Q^2) and is generated on a separate output line by DSP modem board.

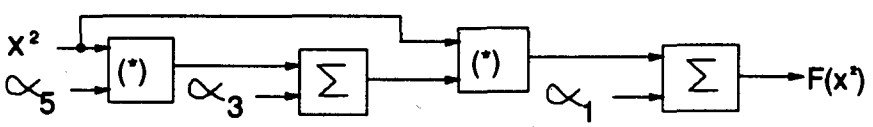

Figure 5.2. Block Diagram of the F1 or F2 Function Using Nested Multiplication

Using Motorola LF357J op amps and Motorola MC1494 linear four-quadrant multipliers [17], the F_1 and F_2 circuits were implemented as illustrated by the circuit schematic of Figure C.1 (Appendix C).

5.2 IMD Quadrature Demodulator and Power Detector

Having shown, in section 2.3, that by first, convolving the power amplifier's output with the real bandpass input signal, and then by bandpass filtering the 3rd and 5th order IMD contributions one could measure the power amplifier's relative out-of-band power, this section provides the implementation details of the IMD quadrature demodulator and power detector circuits.

5.2.1 IMD Quadrature Demodulator Circuit

Mathematically the IMD quadrature demodulation was performed as a complex convolution in the frequency domain between two signals, the real bandpass input signal and the real bandpass power amplifier's output signal. In the time domain this is achieved by quadrature mixing the two signals. The complete mathematical derivation of the quadrature mixing process showing the same resulting spectrum as the convolution technique is presented in Appendix B.

The block diagram of the implemented IMD quadrature demodulator circuit is drawn in Figure 5.3. Note that an in-phase and a quadrature path is needed to account for the in-phase and quadrature nonlinearities generated by the power amplifier.

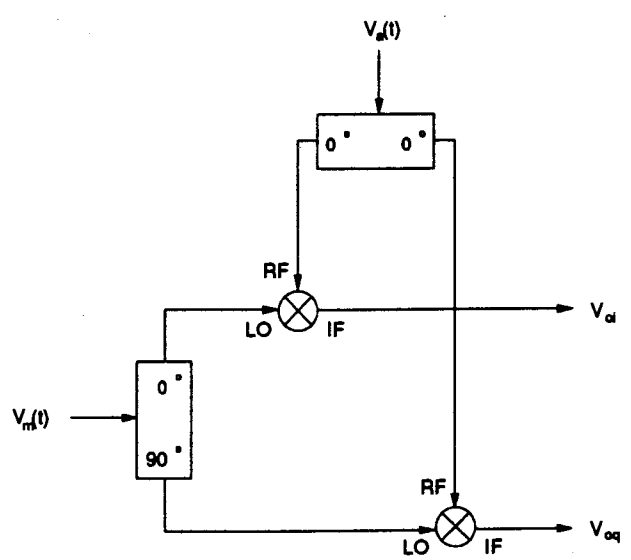

Figure 5.3. Block Diagram of IMD Quadrature Demodulator Circuit

The IMD quadrature demodulator was implemented using Mini-Circuits [18] components. As shown in Figure 5.3, two level 10 mixers (TFM-150), a 90° power splitter (PSCQ-2-70) and a 0° power splitter (PSC-2-4) were utilized. Next, the power contributed by the 3rd and 5th order IMD products in both the I and the Q channels had to be evaluated. To minimize the complexity of the circuitry, an analog multiplexer HCF4066 [19] was used to multiplex the information going to the power detector circuitry. The block diagram of the I and Q channel multiplexer circuit is illustrated in Figure 5.4.

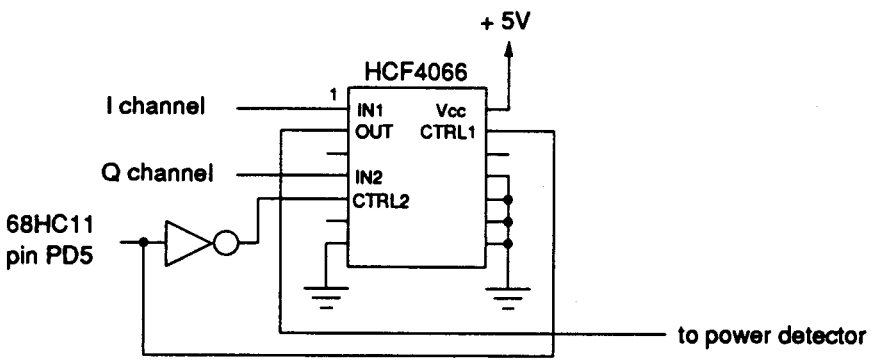

Figure 5.4. Block Diagram of I and Q Multiplexer Circuit

As shown in Figure 5.4, the micro-controller determines whether the I or the Q channel output is to be fed to the power detector circuit.

5.2.2 Power Detector

Having quadrature demodulated the power amplifier's spectrum to baseband, the power contained at the 3rd and 5th order IMD frequencies has to be measured. The IMD signals contained in the quadrature demodulated spectrum were quite weak, in the -70 dBm range, hence, they had to be amplified prior to any power measurements.

Initially, a circuit made up of op-amps and a peak detector was used to amplify the baseband signal and detect the IMD power. However, since the signal had to be amplified by at least 70 dB before the power could be detected, the op-amps were operating close to saturation, making the power measurements unreliable.

The alternate solution was to use the IF amplifiers and received signal strength indicator incorporated in a Signetics NE604 [20] low power FM IF system. The NE604 has two independent limiting amplifiers capable of 90 dB total gain. Also, the received signal strength indicator is usable over a 90 dB range and has a 1.5 dB accuracy. The frequency components corresponding to the 3rd and 5th order IMD products are filtered out of the baseband signal and the NE604 is used to generate a voltage proportional to the power contained in the 3rd and 5th order IMD product band. A basic diagram of the power detector system is shown in Figure 5.5.

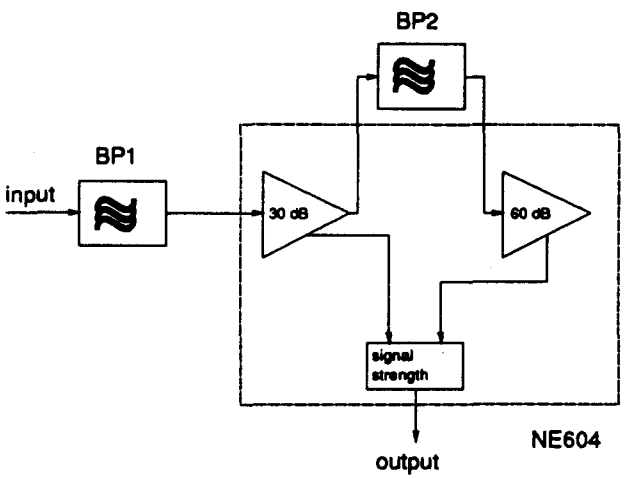

Figure 5.5. Basic Diagram of Power Detector System

The two blocks denoted BP1 and BP2 in Figure 5.5, are bandpass filters designed to pass the 3rd and 5th order IMD products. The bandpass filters not only separate the IMD products from the baseband signal spectrum, but they also ensure that the two limiting amplifiers will not saturate. The complete schematic of the implemented power detector circuit is presented in Figure C.2 (Appendix C).

5.2.2.1 Bandpass Filter

As shown earlier, the baseband signal contains 3rd or 5th order IMD components that have to be bandpass filtered. The baseband signal frequencies up to twice the symbol rate do not contain any usable IMD contributions, hence they have to be rejected. The first bandpass filter, labelled BP1 in Figure 5.5, was designed [21] to have cutoff frequencies f_L=29 kHz and f_H=54 kHz. Since one of the reasons for using this filter was to ensure that the first NE604 amplifier does not saturate, the requirements for the high frequency attenuation were not too stringent. The BP1 filter was implemented with a 14th order passive filter (i.e. a 10th order high pass followed by a 4th order low pass). The simulated and measured frequency response plots of the BP1 filter are shown in Figures 5.6 and 5.7.

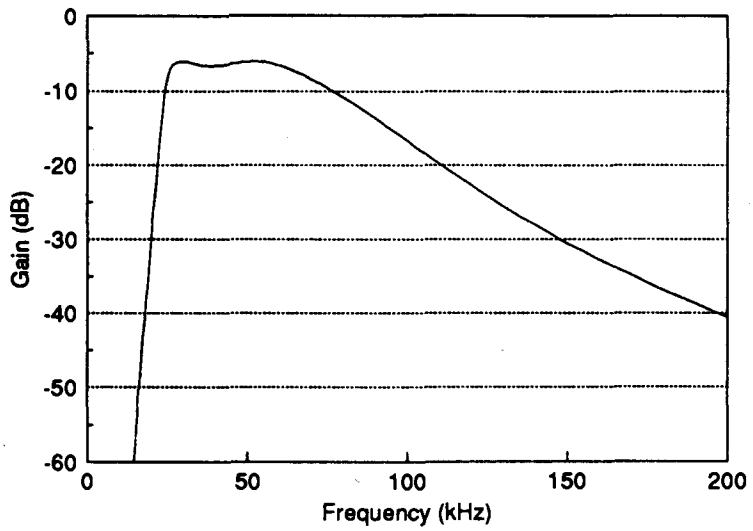

Figure 5.6. Simulated Frequency Response of BP1 Filter

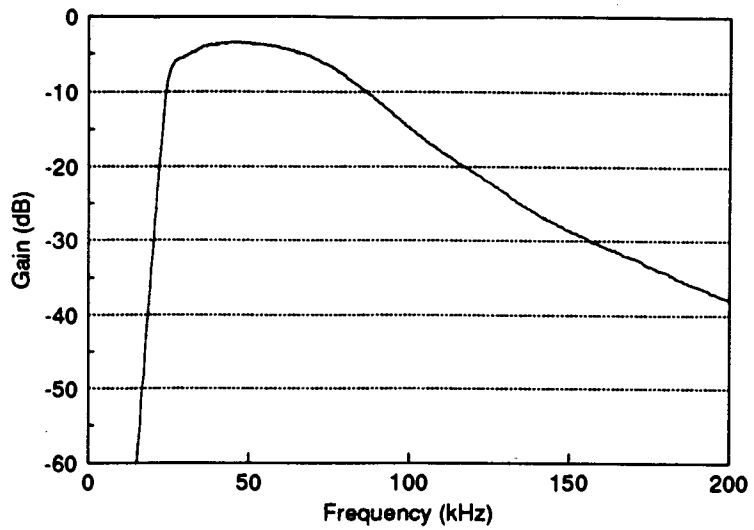

Figure 5.7. Measured Frequency Response of BP1 Filter

Note that the low frequency rejection is in excess of 50 dB at 1/2 f_L. Also, in order to match to the impedance of the I and Q separator circuit, the filter was designed for 50 Ω input and output impedances. The schematic of the passive BP1 filter is drawn in Figure 5.8.

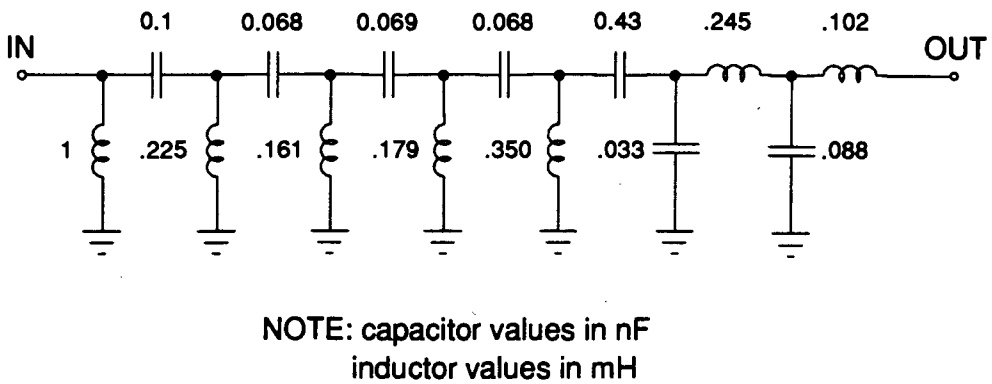

Figure 5.8. Schematic of BP1 Filter

The second bandpass filter, labelled BP2 in Figure 5.5, is connected between the two amplifiers of the NE604. Apart from ensuring that the second amplifier does not saturate, the BP2 filter has tight rejection requirements. The cutoff frequencies are f_L=29 kHz and f_H=51 kHz. The simulated and measured frequency response of the BP2 filter are presented in Figures 5.9 and 5.10.

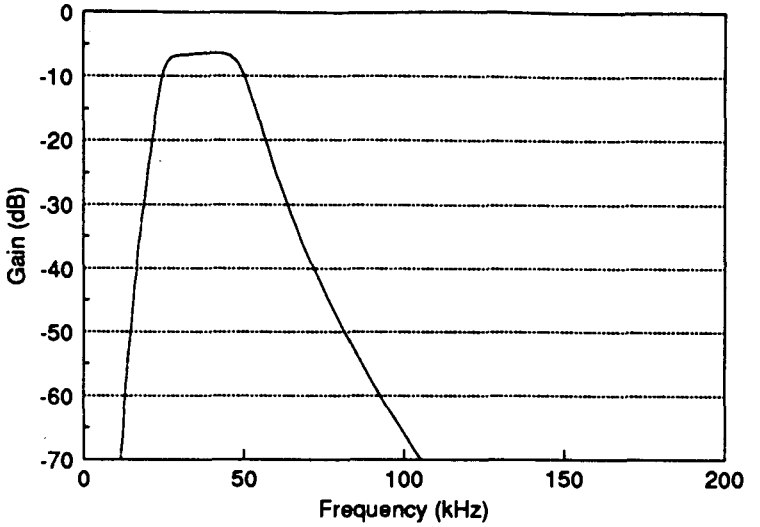

Figure 5.9. Simulated Frequency Response of BP2 Filter

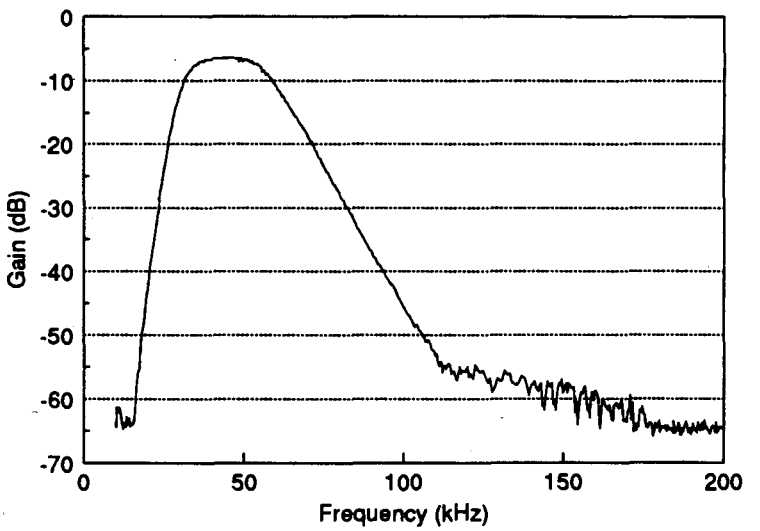

Figure 5.10. Measured Frequency Response of the BP2 Filter

The response shown in Figures 5.9 and 5.10 was obtained with a passive 20th order bandpass filter (a 10th order high pass followed by a 10th order low pass). Since the input and output impedances of the NE604's amplifiers were approximately 1500 Ω, the BP2 filter was designed to have 1500 Ω impedance. The schematic of the BP2 filter is drawn in Figure 5.11.

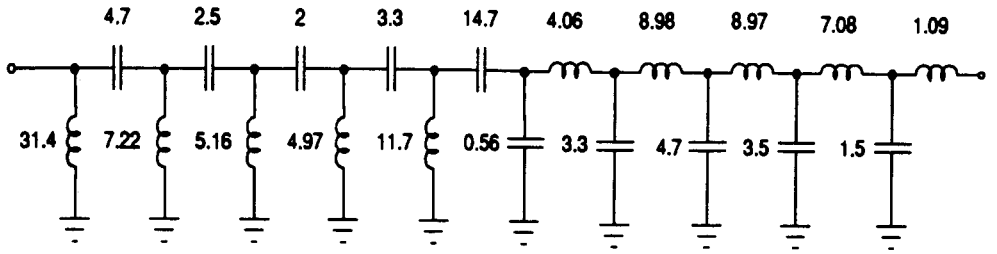

NOTE: capacitor values in nF
inductor values in mH

Figure 5.11. Schematic of BP2 Filter

5.3 Micro-controller and Interface Circuitry

Recall that the micro-controller is a very important part of the linearizer, since it controls the information flow between the nonlinear function generator circuit, IMD quadrature demodulator, power detector circuit and adaptation algorithm. This section describes the design and implementation of the analog to digital converter (ADC) circuit, digital to analog converter (DAC) circuit and the necessary circuits for micro-controller interface.

The Motorola MC68HC11 EVB [22] was the micro-controller used for the adaptive predistorter implementation. The MC68HC11 is run by a 2.1MHz clock, giving a 476 ns instruction cycle. The following sub-sections present the design and implementation of the DAC, ADC and interface circuits.

5.3.1 Design of DAC Interface Circuit

The DAC circuit allows the adaptation algorithm to alter the α_3 and α_5 coefficients of the F_1 and F_2 functions. Since the MC68HC11 is an 8 bit micro-controller, an 8 bit DAC had to be selected. The Texas Instruments TLC7528C [23] 8 bit dual DAC was chosen. The TLC7528C has a 100 ns settling time, fast enough to be used with the MC68HC11 EVB. Also, each TLC7528C is a dual DAC, meaning that only two integrated circuits are needed to control the four α coefficients.

A control logic circuit was designed to allow individual adjustment of the α_3 and α_5 coefficients. Port C of the MC68HC11 EVB was designated as the data bus, while the 8 bits of port B were used as control bits and were encoded as shown in Table 5.2. Note that A1 and B1 refer to the A or B DAC on the first TLC7528C, while A2 and B2 refer to the A or B DAC on the second TLC7528C.

Table 5.2. Control Logic for the DAC Interface Circuit

BITS								DAC #1		DAC #2	
B 7	B 6	B 5	B 4	B 3	B 2	B 1	B 0	A1	B1	A2	B2
0	1	0	0	0	0	0	0	write	hold	hold	hold
0	1	0	0	1	0	0	0	hold	write	hold	hold
0	0	1	0	0	0	0	1	hold	hold	write	hold
0	0	1	1	0	0	0	1	hold	hold	hold	write
1	1	1	1	1	1	1	1	hold	hold	hold	hold

Using a -1.28 V reference for the DACs, allows the variation of the α_3 and α_5 coefficients in 0.005 V steps from 0 to 1.28 V. Since the α_3 and α_5 coefficients had to be altered through both positive and negative values, a -0.64 V offset was incorporated into each α coefficient output line, meaning that each α coefficient could be changed from -0.64 V to 0.64 V in 0.005 V increments. Note that if a larger control range for the α coefficients is desired, the DACs reference and the offset voltage can be easily changed. The complete schematic of the DAC circuits is presented in Figure C.3 (Appendix C).

5.3.2 Design of ADC Interface Circuit

The power detector circuit generates a voltage level, IM_o power level, proportional to the power in the 3rd and 5th order IMD products. The optimization algorithm adjusts the α coefficients so as to minimize this voltage level. The micro-controller has to relay the voltage level to the optimization algorithm, hence an ADC is needed to convert the analog voltage level to a digital level.

The National Semiconductor ADC0841 [24] was chosen since it has micro-controller interface control lines. The ADC0841 is an 8 bit successive approximation ADC. The original design used two ADC, one for the I channel IM_o power value and one for the Q channel IM_o power value. The final design uses a single power detector and an analog multiplexer to select the I or the Q channel IM_o power value, hence only one ADC is needed.

The ADC was connected in the continuous conversion configuration meaning that the most up-to-date IM_o power value is always available at the micro-controller's input. Note that port E of the MC68HC11 was used as the input data bus transferring information from the ADC. The complete schematic of the ADC interface circuit is illustrated C.4 (Appendix C).

5.4 Adaptation Control Interface

The simulations outlined in Chapter 4, used C routines for the various optimization methods. Since the optimization methods were already implemented in C, a main control program was written using TurboC. The main control program is interfaced with the 68HC11 micro-controller via the RS232 port and it allows the user complete control over the operation of the predistorter linearizer.

The control program allows the user to select either static or adaptive operation of the predistorter. For adaptive operation, the user can select either one of the three optimization techniques discussed earlier, Hooke and Jeeves', steepest descent or DFP. For static predistortion, the user can adjust any of the α coefficients manually. The value of the power amplifier's out-of-band power is displayed on the monitor to guide the user in reducing its value.

A routine is available to disable the predistorter, by setting the α_3 and α_5 coefficients to zero. Also, routines to characterize the α_3 or α_5 planes for any power amplifier have been included in the main control routine. These routines vary the α coefficients measuring the IM_o

power value every time a coefficient is varied. From the contour plot obtained as a result of this process, the user can find the optimum value of the α coefficients for a minimum IM_o power value. A flow chart of the main control program is shown in Figure 5.12.

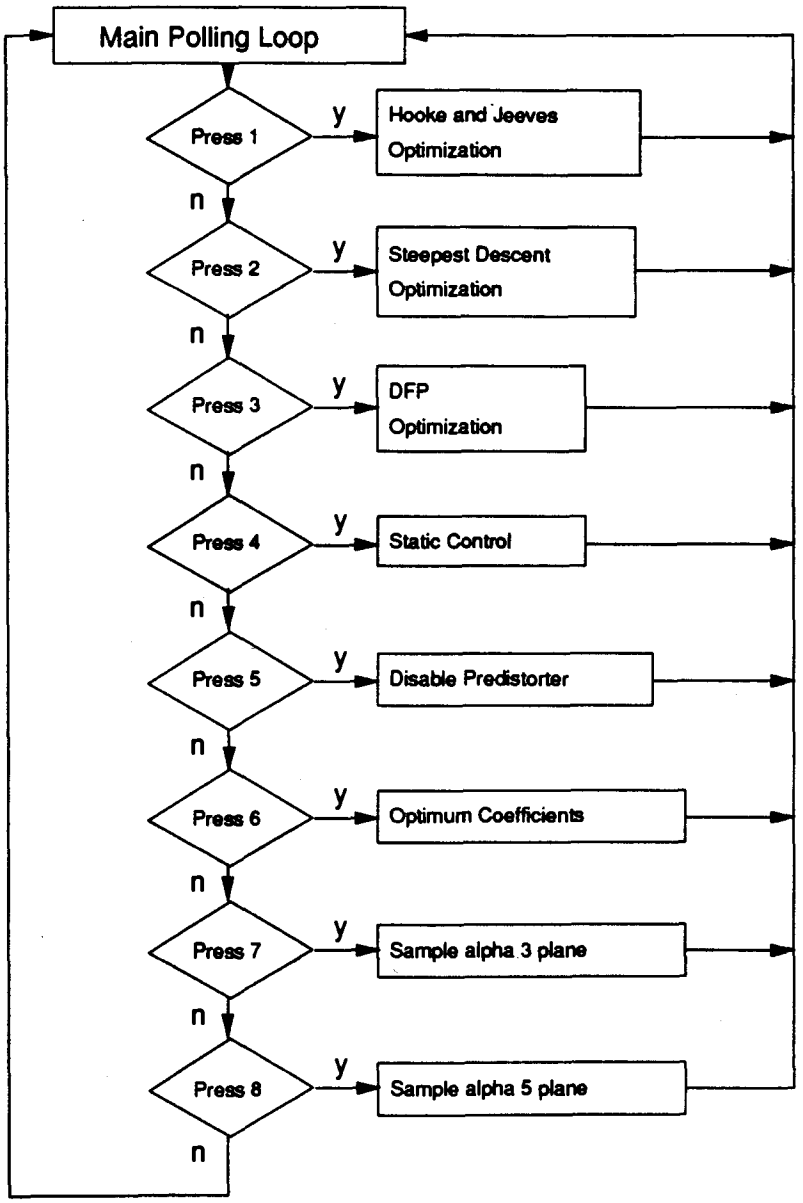

Figure 5.12. Flow Chart for Main Control Routine

6 PERFORMANCE OF IMPLEMENTED ADAPTIVE PREDISTORTER

This chapter presents the results obtained with the implemented analog adaptive predistorter, using a 16 QAM input signal. First, the experimental set-up is presented and some of the problems encountered in getting the adaptive analog predistorter operational are discussed. This is followed by the results obtained with the Hooke and Jeeves, steepest descent and DFP optimization methods. The chapter is ended with a comparison of the three optimization methods for rate of convergence and IMD skirts reduction.

6.1 Experimental Set-up

The experimental set-up used to test the performance of the adaptive analog predistorter is illustrated in Figure 6.1.

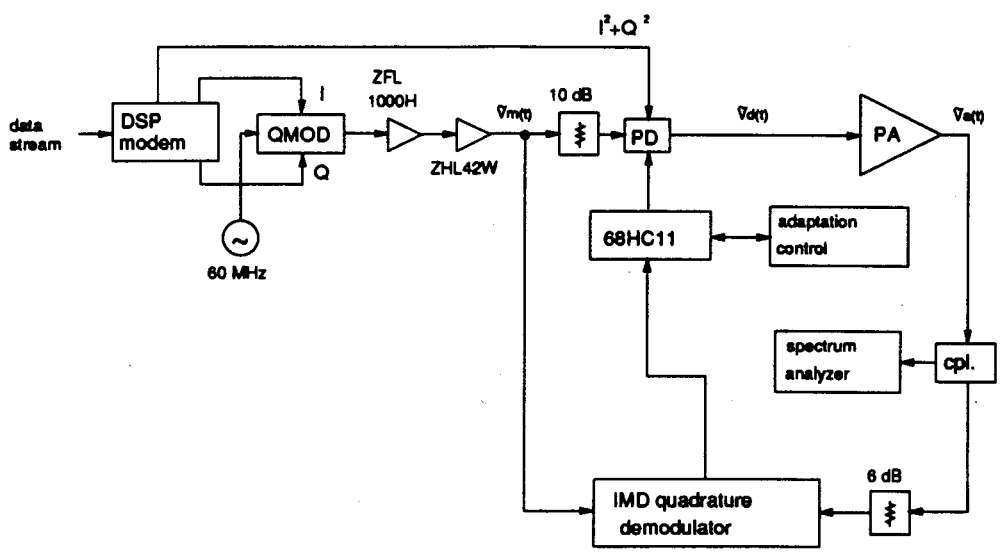

Figure 6.1. Experimental Set-up

The DSP modem generates the I and Q channel data for the 16 QAM signal. Since the predistorter module is made up of a quadrature modulator operating in the 55-90 MHz frequency range, an identical quadrature modulator was used to up-convert the complex baseband 16 QAM signal into the real bandpass 16 QAM signal. 60 MHz was selected to be the testing carrier

frequency. The real bandpass 16 QAM signal is amplified by two Mini-Circuits amplifiers (ZFL-1000H and ZHL42W) to provide the mixers in the IMD quadrature demodulator circuit with the required power level.

The power amplifier used to test the adaptive analog predistorter was built using a Mini-Circuits MAR-6 amplifier that operates in the DC-2 GHz frequency range. The MAR-6 amplifier has a gain of 20 dB and a 1 dB compression point of 0 dBm. The power amplifier's output is connected to the IMD quadrature demodulator. A spectrum analyzer is connected in the experimental set-up via a coupler at the output of the power amplifier. The spectrum analyzer is used to visually monitor the reduction of the power amplifier's IMD skirts as a result of optimizing the α coefficient values. Also, the spectrum analyzer is used to down-load the data corresponding to the spectra at the power amplifier's output before and after each adaptation routine.

6.1.1 Experimental Set-up Difficulties

Several difficulties were encountered in the process of getting the adaptive analog predistorter operational. This subsection outlines some of the critical ones and how they were solved. First, since the proper operation of the F_1 and F_2 function generating circuits is crucial to the performance of the predistorter, the F_1 and F_2 function generating circuits need to be calibrated. The four quadrant multipliers are not perfect devices, hence any offset on either of the two inputs generates harmonics that affect the operation of the predistorter. These offsets can be nulled out by adjusting the input offset trimmers incorporated into the circuits. A calibration procedure has been adopted, in which a sinusoid is used as input to the F_1 and F_2 function generating circuits and all the multiplier input offsets are nulled out.

A second problem that is also related to the predistorter's operation is the stability of the voltage references needed by the DAC circuits and α_3 and α_5 coefficient DC offsets. Since the stability of the voltage reference governs the accuracy of the α_3 and α_5 coefficient values, precision voltage references were utilized to obtain the needed reference voltages.

Initially, the operation of the IMD quadrature demodulator and power detector circuit proved to be puzzling. It was found that a reduction in the IM_o power value produced by the power detector corresponded to a reduction in the power amplifier's IMD skirts. However, the minimum IM_o power value found by the optimization routines did not correspond to the greatest reduction of the power amplifier's IMD skirts. It was first thought that an error in the ADC circuit's operation combined with a software bug were the cause of this discrepancy.

The problem was found to be caused by the operation of the IMD quadrature demodulator. The operation of the IMD quadrature demodulator proved to be sensitive to the $\tilde{V}_m(t)$ and $\tilde{V}_a(t)$ signal power levels. The $\tilde{V}_m(t)$ signal power level is critical to the operation of the mixers of the IMD quadrature demodulator. Since level 10 mixers were utilized, two Mini Circuits amplifiers, as shown in Figure 6.1, were needed to ensure that the $\tilde{V}_m(t)$ signal power level at the input to the IMD quadrature demodulator was roughly 10 dBm. Finding the necessary $\tilde{V}_a(t)$ signal power level at the input of the IMD quadrature demodulator needed some experimentation. It was found that a 6 dB attenuator was needed between the power amplifier's output and the IMD quadrature demodulator circuit in order for the minimum IM_o power value to correspond to the maximum reduction in the power amplifier's IMD skirts.

Just like for the case of the simulations, the accuracy of the IM_o power value is critical to the convergence of the adaptation algorithms. To find the uncertainty in the IM_o power value, the number of samples per IM_o power value evaluation were varied from 5 to 30 samples. The results of the measurements are shown in Figure 6.2.

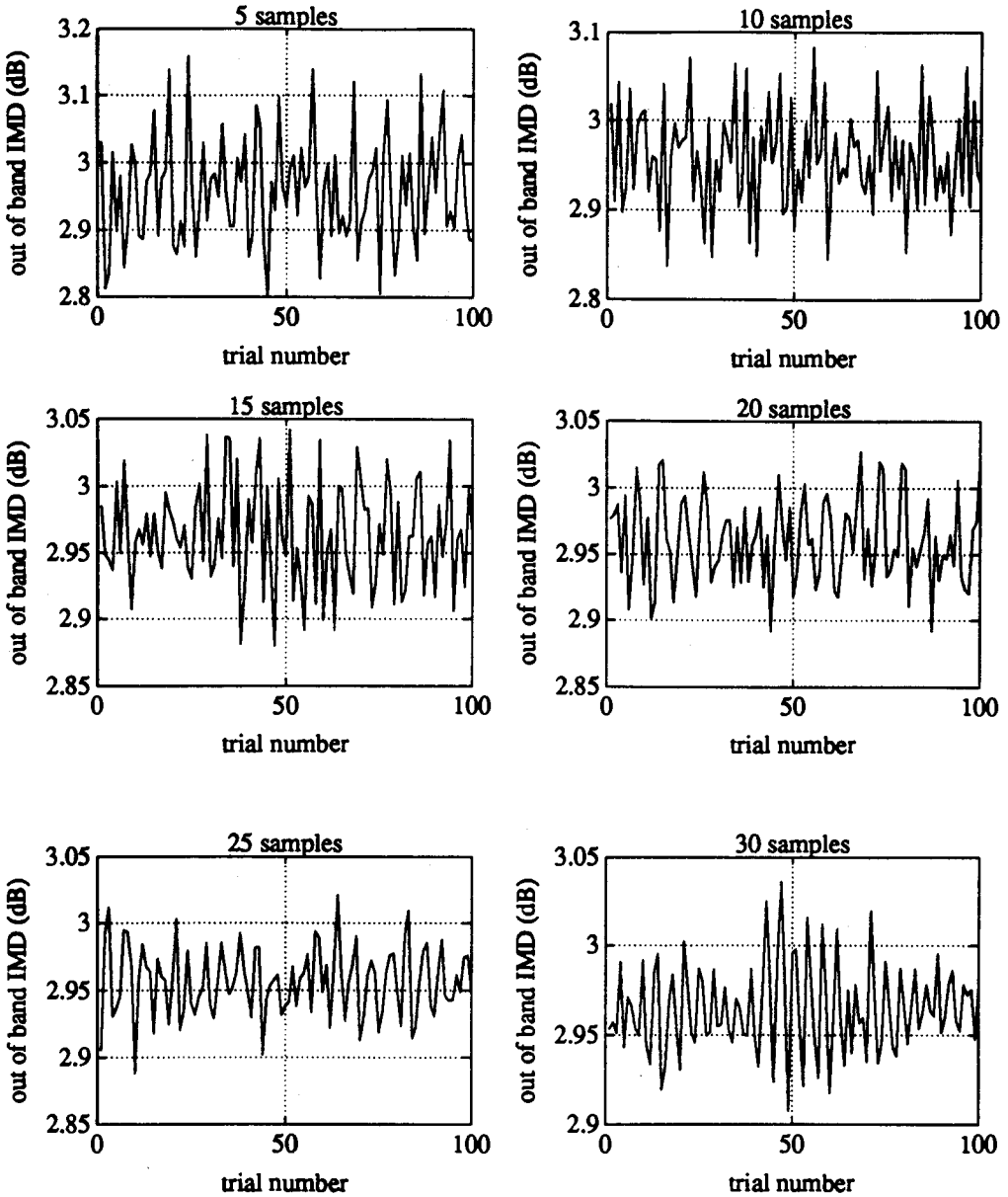

Figure 6.2. IMo Measurements for 5 to 30 Samples

These measurements showed that the higher the number of samples, the more accurate the IM_o power value. The statistical summary of the IM_o power value measurements are presented in Table 6.1.

Table 6.1. Uncertainty in IM_o Power Value Evaluation

# of samples	5	10	15	20	25	30
# of trials	100	100	100	100	100	100
Minimum	2.8002	2.8373	2.8795	2.8918	2.8876	2.9074
Mean	2.9577	2.9585	2.9628	2.9604	2.9563	2.9651
Maximum	3.1590	3.0829	3.0420	3.0274	3.0209	3.0362
Variance	0.0807	0.0574	0.0393	0.0325	0.0258	0.0249

As shown by Table 6.1, the higher the number of samples, the more accurate the IM_o power value. However, it was found that the optimization algorithms converged to the minimum IM_o power value faster when the number of samples was kept relatively small, 5 samples.

6.2 Implemented Predistorter Results

This sub-section presents the results obtained for Hooke and Jeeves method, steepest descent technique and DFP method with the implemented analog predistorter. The normalized spectra of the 16 QAM signal at the input and output of the power amplifier are illustrated in Figure 6.3.

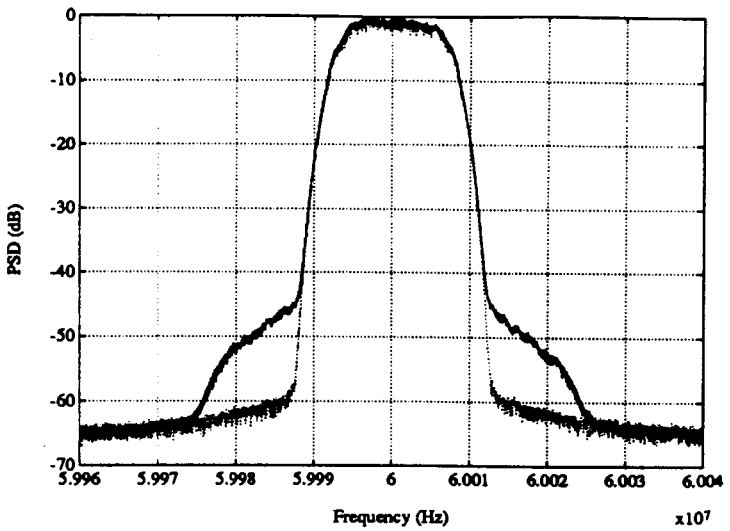

Figure 6.3. Power Amplifier Input and Output Spectra

As shown in Figure 6.3, the 16 QAM input signal has a 60 dB signal to noise ratio and the power amplifier raises the IMD skirts by 15 dB. At the start of each optimization technique, the α_3 and α_5 coefficients were set to zero. This corresponds to having no predistortion. In order to evaluate the IM_o power value, 5 samples of the I and Q down-converted signals were taken by the micro-controller. Delays were incorporated into the micro-controller code to ensure that enough symbols were processed for each IM_o power evaluation. Taking the symbol data rate and the delay into account, it was calculated that one IM_o power value evaluation takes 9375 symbols to process.

6.2.1 Hooke and Jeeves Method

The Hooke and Jeeves algorithm was implemented as described in Chapter 3.1.1 and similar stopping criteria were used. The convergence of the four α coefficients and the convergence of the IM_o power value is shown in the plots of Figures 6.4 and 6.5, respectively.

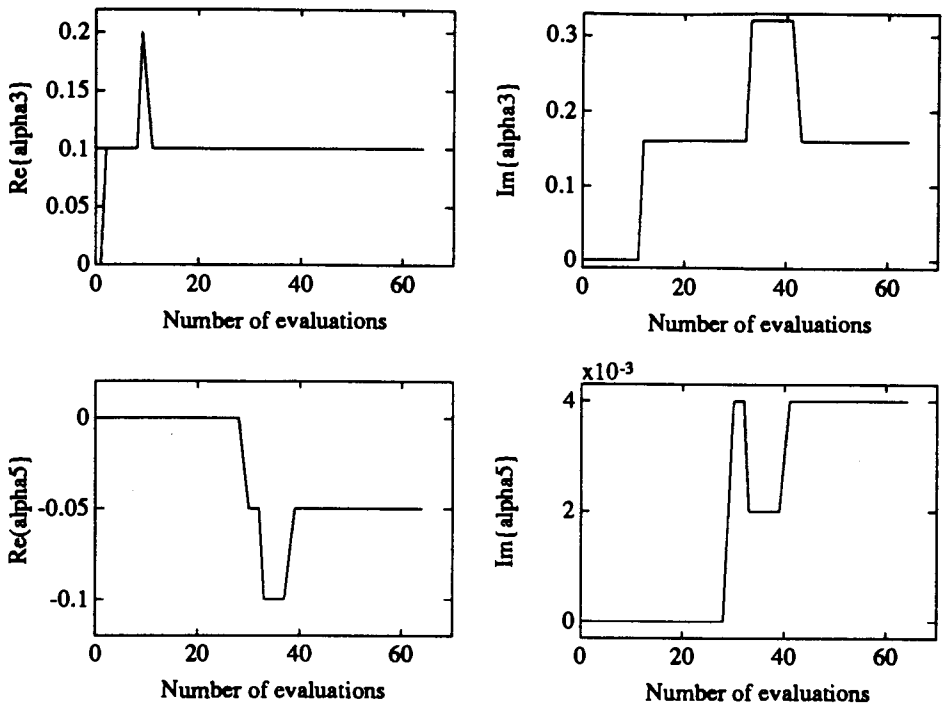

Figure 6.4. Coefficient Convergence for Hooke and Jeeves Optimization

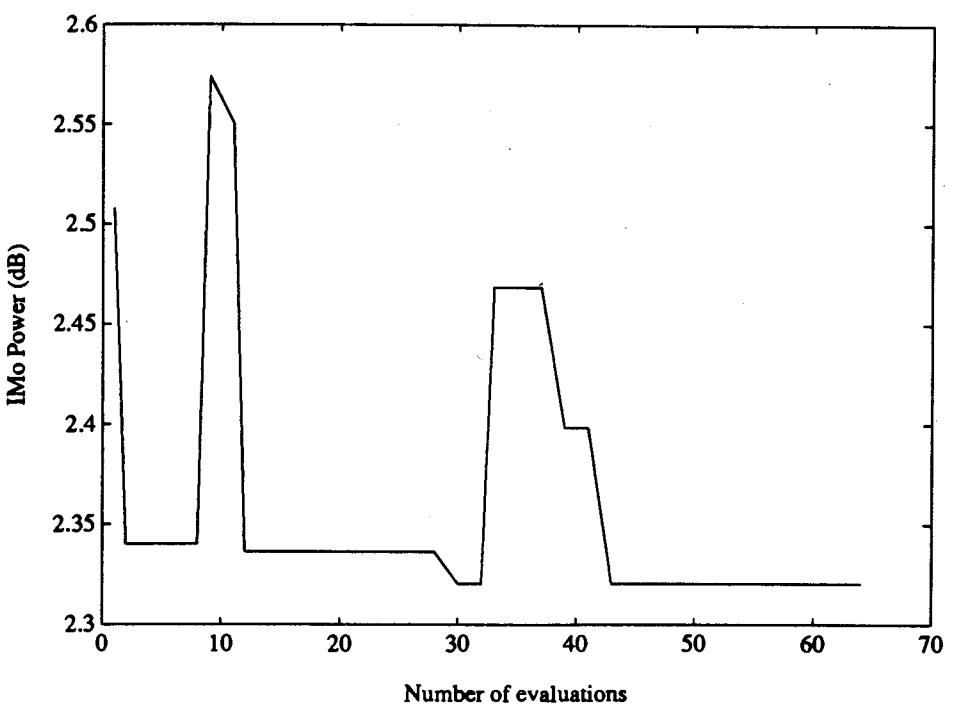

Figure 6.5. IM_o Power Value Convergence for Hooke and Jeeves Optimization

In order to find the minimum IM_o power value, the I and Q outputs of the IMD quadrature demodulator circuit were sampled 64 times. This corresponds to processing 600,000 symbols before the minimum IM_o power value was found. With a 62.5 kbit/second data rate, this amounts to a 38.4 seconds for Hooke and Jeeves' rate of convergence. To show the reduction in the power amplifier's IMD skirts, the PSD seen by the spectrum analyzer shown in Figure 6.1 is plotted before and after the Hooke and Jeeves optimization in Figure 6.6.

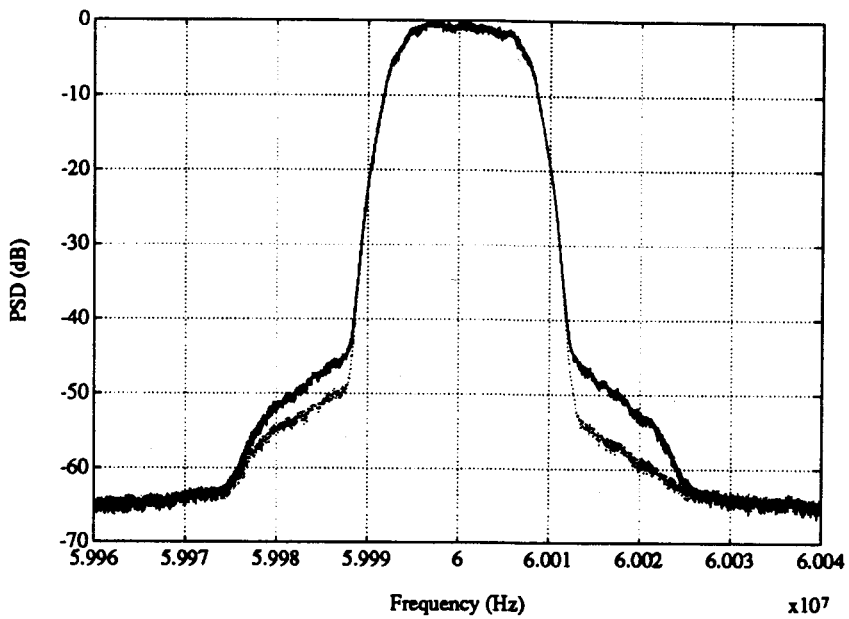

Figure 6.6. PSD of 16 QAM Signal Before and After Hooke and Jeeves Optimization

The optimum predistorter nonlinear functions found by the Hooke and Jeeves method are

$$F_1[x_m(t)] = 1.037 + 0.1x_m(t) - 0.05x_m^2(t)$$

$$F_2[x_m(t)] = 1.014 + 0.16x_m(t) + 0.004x_m^2(t)$$

6.2.2 Steepest Descent Technique

The same code used in the steepest descent simulation section was used by the implemented predistorter. However, different gradient evaluation step size h and descent steplength λ^k had to be used. Also, the gradient evaluation step size h was being reduced by one half after each

complete loop of the algorithm in order to obtain a more accurate IM_o power value. Figures 6.7 and 6.8 show the convergence of the four α coefficients and the convergence of the IM_o power value, respectively.

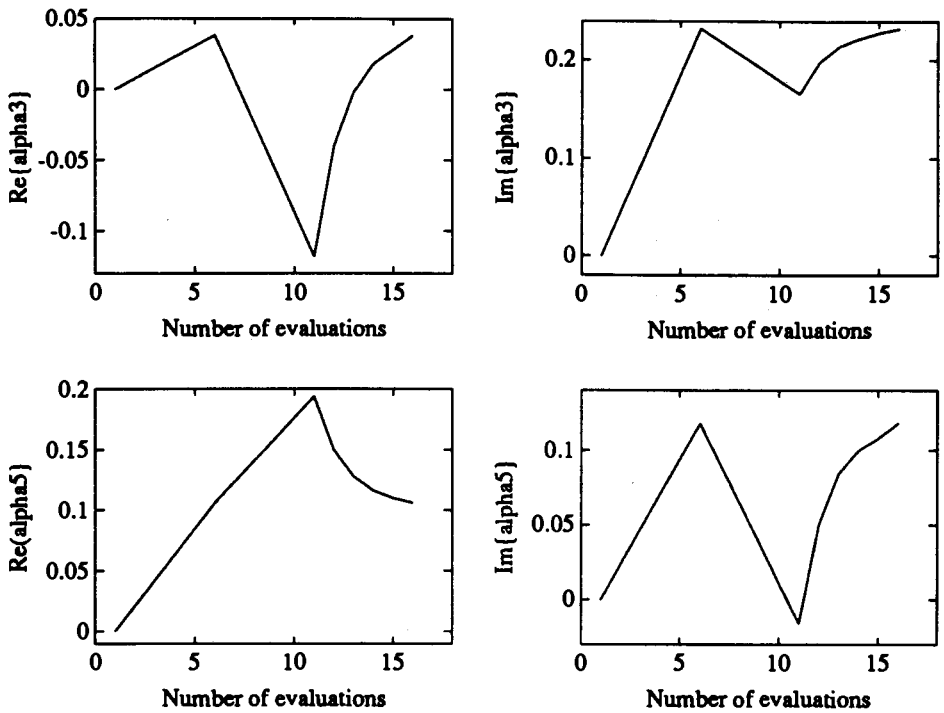

Figure 6.7. Coefficient Convergence for Steepest Descent Optimization

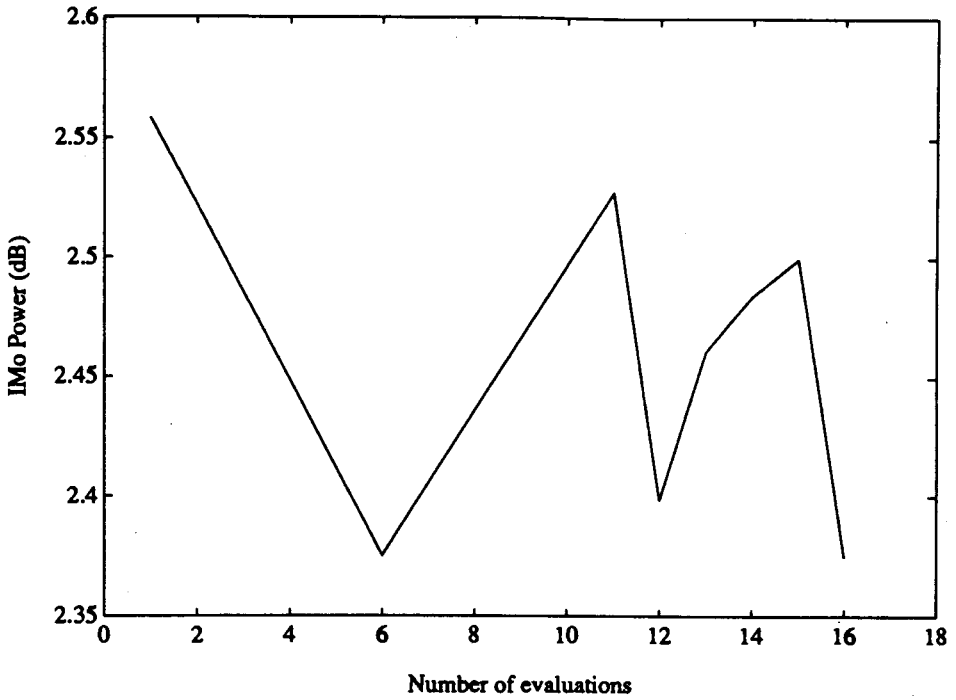

Figure 6.8. IM_o Power Value Convergence for Steepest Descent Optimization

As seen from the convergence plots, the steepest descent optimization technique has to perform 16 IM_o power value evaluations before the minimum IM_o power value is found. This amounts to 150,000 symbols or a rate of convergence of 9.6 seconds. To show the reduction in the power amplifier's IMD skirts, the PSD at the power amplifier's output before and after the steepest descent optimization is plotted in Figure 6.9.

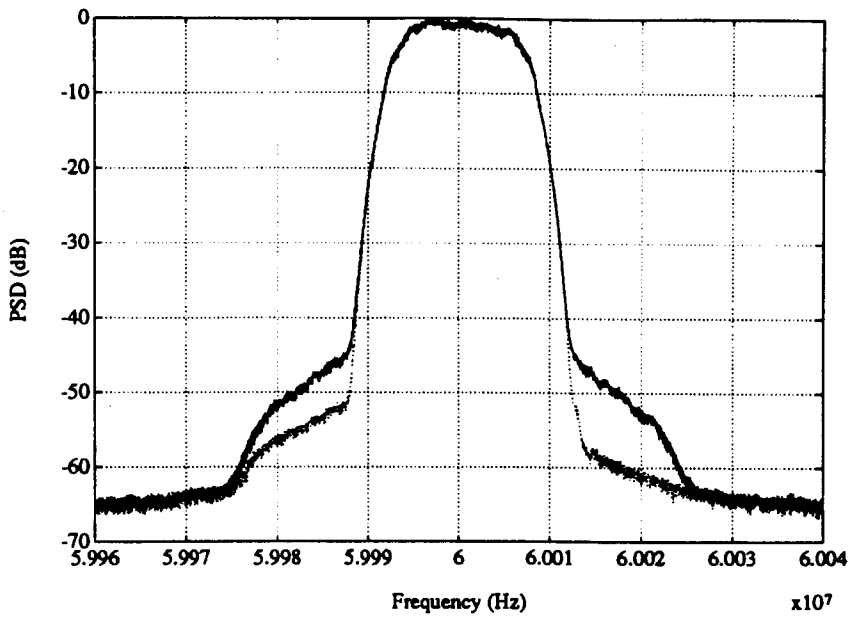

Figure 6.9. PSD of 16 QAM Signal Before and After Steepest Descent Optimization

The optimum predistorter nonlinear functions found by the steepest descent method are

$$F_1[x_m(t)] = 1.037 + 0.038x_m(t) + 0.106x_m^2(t)$$

$$F_2[x_m(t)] = 1.014 + 0.232x_m(t) + 0.118x_m^2(t)$$

6.2.3 DFP Method

The plots showing the convergence of the four α coefficients and the convergence of the IM_o power value are illustrated in Figures 6.10 and 6.11, respectively.

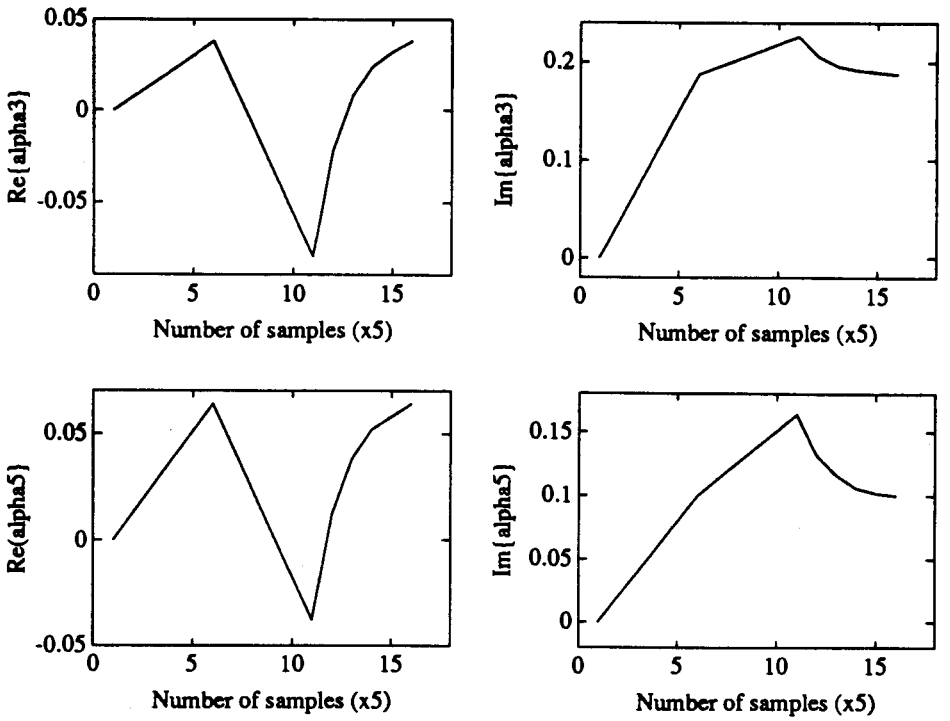

Figure 6.10. Coefficient Convergence for DFP Optimization

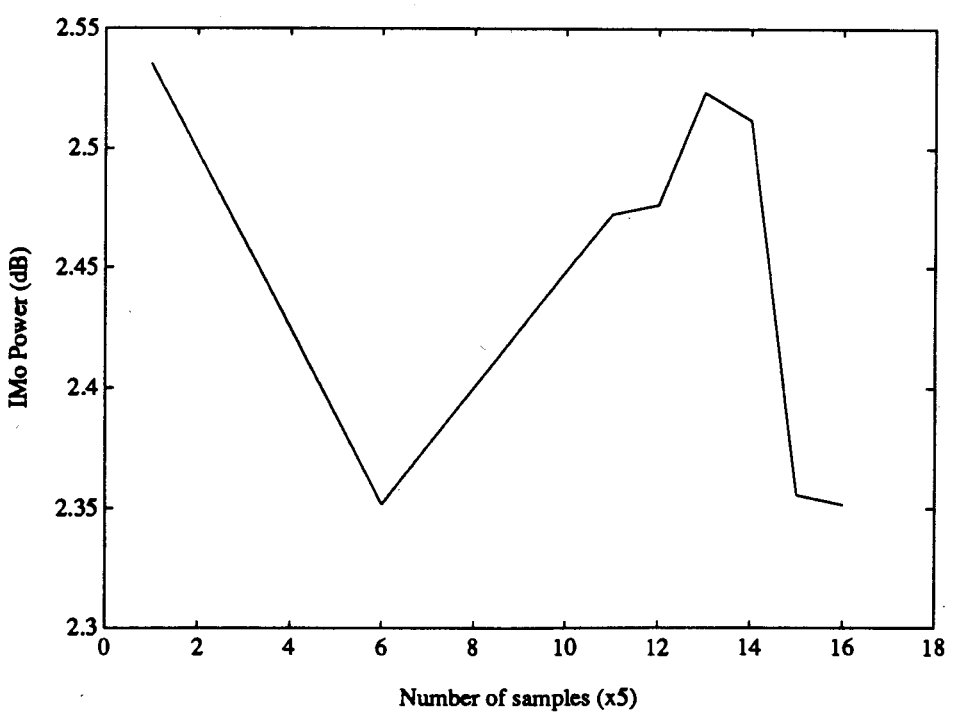

Figure 6.11. IM_o Power Value Convergence for DFP Optimization

Just like for the steepest descent optimization method, 16 IMo power value evaluations had to be performed before the IMo power value was minimized. Again this means that 150,000 symbols had to be processed, which is equivalent to a 9.6 second rate of convergence. The PSD at the power amplifier's output before and after the DFP optimization is shown in Figure 6.12.

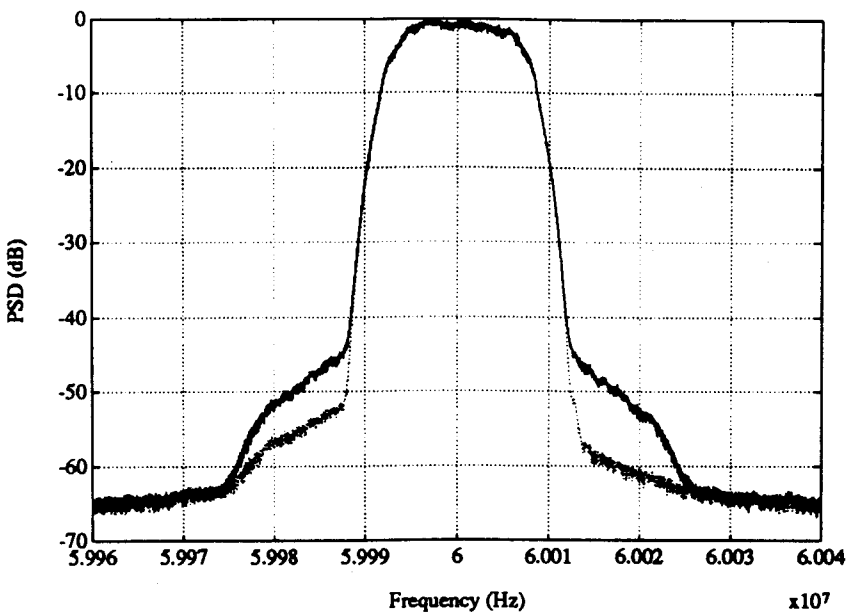

Figure 6.12. PSD of 16 QAM Signal Before and After DFP Optimization

The optimum predistorter nonlinear functions found by the DFP method are

$$F_1[x_m(t)] = 1.037 + 0.038x_m(t) + 0.04x_m^2(t)$$

$$F_2[x_m(t)] = 1.014 + 0.188x_m(t) + 0.100x_m^2(t)$$

6.3 Comparison of Results

As shown in Figures 6.6, 6.9 and 6.12, the PSD at the end of the three optimizations is not symmetric. It was first thought that quadrature modulator and quadrature demodulator gain and phase imbalances and DC offsets were the cause of the asymmetric spectra. However, it was showed by Derek Hilborn [25] that quadrature modulator and demodulator imbalances and offsets do not cause the spectrum asymmetry.

I believe that spectrum asymmetry is related to an isolation problem in the IMD quadrature demodulator circuit and also to feedback due to signal pick-up. As a result of pick-up, a feedback path between the power amplifier's input ad output is created. The mixers used in the IMD quadrature demodulator have a 25-32 dB LO-RF isolation. Since the power level of the LO signal is higher than the power level of the RF signal, some of the LO signal will leak into the RF path which is connected to the power amplifier's output. This leakage mixes with the amplifier's output signal and can cause the asymmetric spectrum. Also, since most of the circuits were implemented on prototype boards, pick-up of signals from adjacent circuits could also contribute to the asymmetric spectrum.

Next, to compare the achieved IMD skirt reduction of the three optimization methods, the PSD at the output of the power amplifier before and after optimization were plotted as shown in Figure 6.13.

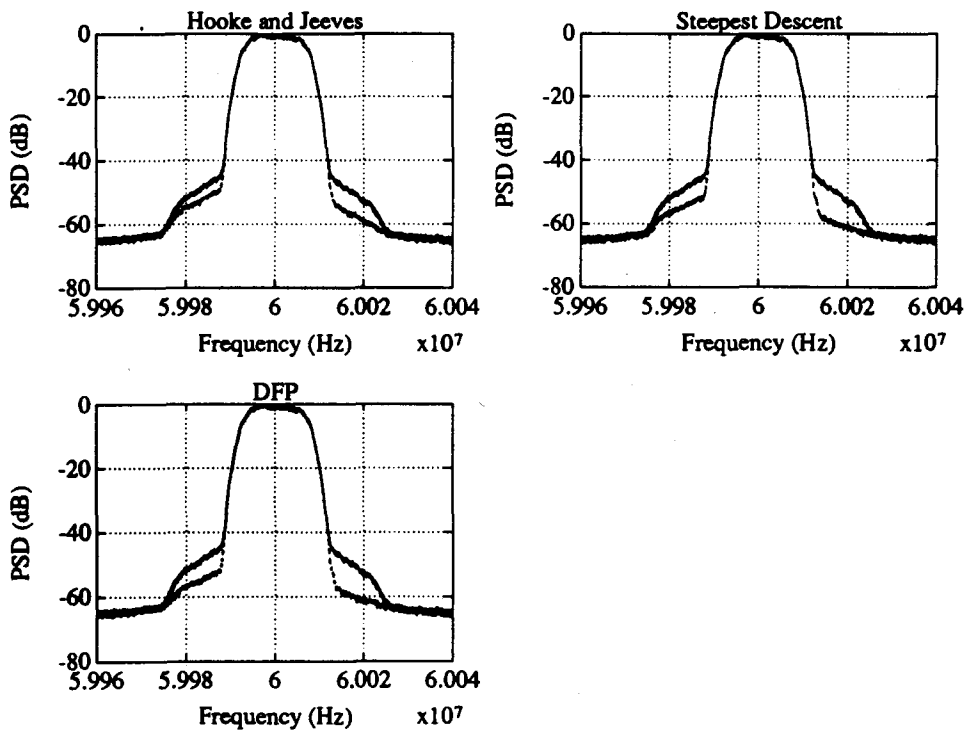

Figure 6.13. PSD Before and After Optimization for Implemented Predistorter

The Hooke and Jeeves optimization method reduced the power amplifier's IMD skirts by 5 dB and by 9 dB on the left and right hand side of the spectrum, respectively. The steepest descent optimization method reduced the power amplifier's IMD skirts by 8 dB and by 12 dB on the left and right hand side of the spectrum, respectively, while the DFP optimization method reduced the power amplifier's IMD skirts by almost 10 dB and by 13 dB on the left and right hand sides of the spectrum, respectively.

Figure 6.14 compares the convergence rate of the three optimization methods.

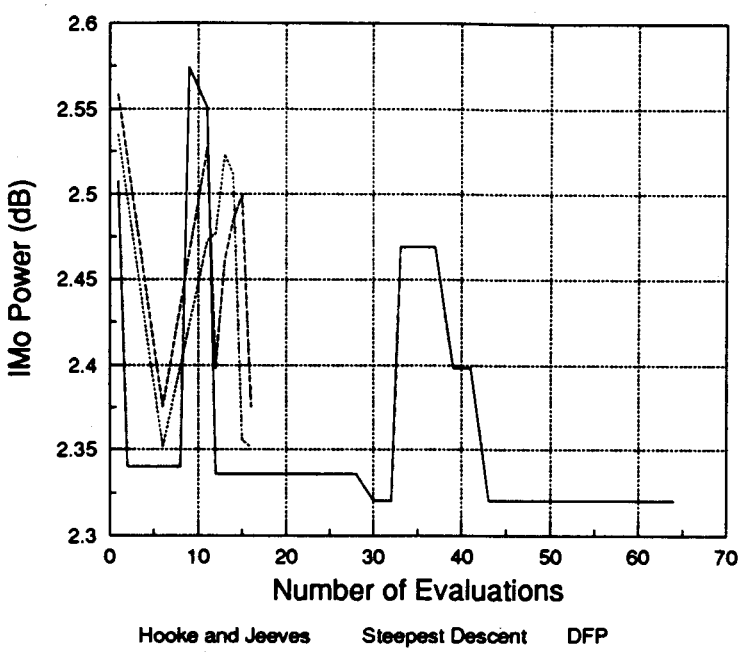

Figure 6.14. Convergence Comparison Plot for Implemented Adaptive Predistorter

As shown in Figure 6.14, Hooke and Jeeves method needed 38.4 seconds to converge to the minimum IM_o power value. The steepest descent and DFP methods reduced the IMD skirts almost by the same amount and both took 9.6 seconds to converge to the minimum IM_o power value. From the simulation performed, the DFP method should have converged faster than the steepest descent. This discrepancy is caused by the uncertainty in the IM_o power value evaluations. Since both steepest descent and DFP methods start with the Hessian matrix equal to the identity matrix, both methods found the minimum IM_o power value after the first loop through the optimization code. The uncertainty in the IM_o power value due to noise, as outlined

in section 6.1.1, does not allow the optimization algorithms to find a lower IM_o power value. Therefore, the update of the perturbations performed on the Hessian matrix by the DFP method were done in vain since the uncertainty of the IM_o power value did not allow the DFP method to find a smaller IM_o power value.

7 CONCLUSIONS AND RECOMMENDATIONS

This thesis presented an adaptive analog polynomial predistorter that can be used to compensate for a power amplifier's AM-AM and AM-PM nonlinearities. The adaptation allows the predistorter to monitor the power amplifier's out-of-band power and iteratively adjust the predistorter parameters to minimize the IM_o power value. A technique to measure the power amplifier's IM_o power value was introduced by which the power amplifier's distorted signal is mixed with a "clean" input signal to quadrature demodulate the I and Q channel out-of-band power contributions to baseband, where the power content can be easily measured.

The IMD quadrature demodulator circuit can be improved for future applications either by using mixers that possess higher isolations, or in-line isolators can be used at the LO and RF inputs. Also, a way to eliminate the feedback effects is needed, if feedback does prove to be one of the reasons for the asymmetry of the output spectrum. An alternate method for measuring the power amplifier's IM_o power value would be to directly down-convert the power amplifier's output signal to baseband, then filter out the contribution of the 3^{rd} and 5^{th} order IMD products.

The noise pick-up can be greatly reduced by making printed circuit boards for all the separate circuits that make up the analog predistorter. Also each sub-circuit has to be well shielded to prevent the pick-up of the stronger signals.

As a result of the simulations of the adaptive predistorter with a 16 QAM input signal a 15 dB reduction of the power amplifier's IMD skirts was achieved. The IMD skirt reduction was further confirmed when the adaptive analog polynomial predistorter was implemented and tested with a 16 QAM input signal. A 10-13 dB reduction of the IMD skirts was obtained by optimizing the α coefficients. The fastest achieved convergence was 9.6 seconds for a 62.5 kbit/second data rate. Since the convergence rate is quite small, the optimization algorithm can be made to continuously monitor the IMo power value and adapt to drifts in the performance of the amplifier caused by transistor degradation, temperature changes and channel switches.

8 REFERENCES

[1] CCIR Rec. 478-2.

[2] Saleh, A.A.M. and Cox, D.C., "Improving the Power-Added Efficiency of FET Amplifiers Operating with Varying Envelope Signal", *IEEE Transactions on Microwave Theory and Techniques*, vol. 31, no. 1, pp. 51-56, January 1983.

[3] Green, D.R. Jr., "Characterization and Compensation of Nonlinearities in Microwave Transmitters", *IEEE Trans.*, pp. 213-217, 1982.

[4] Casadevall, F.J., "The LINC Transmitter", *RF Design*, pp. 41-48, February 1990.

[5] Akaiwa, Y. and Nagata, Y., "Highly Efficient Digital Mobile Communications with a Linear Modulation Method", *IEEE Journal Sel. Areas in Comm.*, vol. SAC-5, no. 5, pp. 890-895, June 1987.

[6] Bateman, A., Haines, D.M. and Wilkinson, R.J., "Linear Transciever Architecture", *Proc. IEEE Veh. Tech. Conf.*, 1988, pp. 478-484.

[7] Namiki, J., "An Automatically Controlled Predistorter for Multilevel Quadrature Amplitude Modulation", *IEEE Trans. on Comm.*, vol. COM-31, no. 5, pp. 707-712, May 1983.

[8] Nojima, T. and Konno, T., "Cuber Predistortion Linearizer for Relay Equipment in the 800 MHz Band Land Mobile Telephone System", *IEEE Trans. on Vehic. Tech.*, vol VT-34, no. 4, pp. 169-177, November 1985.

[9] Nannicini, M., Magni, P. and Oggioni, F., "Temperature Controlled Predistortion Circuits for 64 QAM Microwave Power Amplifier", *IEEE Trans. on Vehic. Tech.*, vol. VT-34, no. 4, pp 169-177, November 1985.

[10] Nagata, Y., "Linear Amplification Technique for Digital Mobile Communications", *Proc. IEEE Vehic. Tech. Conf.*, pp 159-164, San Francisco 1989.

[11] Saleh, A.A.M. and Salz, J., "Adaptive Linearization of Power Amplifiers in Digital Radio Systems", *Bell Syst. Tech. J.*, vol. 62, no. 4, pp. 1019-1033, Apr. 1983.

[12] Cavers, J.K., "A Linearizing Predistorter with Fast Adaptation", *40th Vehicular Technology Conference*, IEEE Cat. 90CH2864-4, pp. 41-47.

[13] Jacoby, S.L.S., Kowalik, J.S. and Pizzo, J.T., *Iterative Methods for Nonlinear Optimization Problems*, New Jersey: Prentice-Hall, 1972.

[14] Bunday, B.D., *Basic Optimization Methods*, London: Edward Arnold, 1984.

[15] Peressini, A.L., Sullivan, F.E. and Uhl, J.J. Jr., *The Mathematics of Nonlinear Programming*, New York: Springer-Verlag, 1988.

[16] Kandola, G, *Analysis and Simulation of an Adaptive Predistorter*, MASc Thesis, School of Engineering Science, 1991.

[17] Motorola, *Linear/Interface Devices*, pp. 11-11 to 11-24.

[18] Mini-Circuits, *RF/IF Signal Processing Handbook, Volume 2*.

[19] National Semiconductor, *CMOS Logic Databook*, pp. 5-179 to 5-181.

[20] Signetics, *Linear Data Manual, Volume 1: Communications*, 1987, pp. 4-119 to 4-129.

[21] Geis, L.J., *Transform Analysis and Filters*, New Jersey: Prentice-Hall, 1989.

[22] Motorola, *M68HC11 Reference Manual*, New Jersey: Prentice-Hall, 1989.

[23] Texas Instruments, *Linear Circuits, Data Acquisition and Conversion*, vol. 2, 1989, pp. 2-223 to 2-246.

[24] National Semiconductor, *Data Acquisition Linear Devices Databook*, 1989, pp. 3-158 to 3-169.

[25] Hilborn, D., personal correspondence, 1991.

APPENDIX A

Mathematical Derivation of Composite Complex Gain Coefficients

Start by substituting the truncated complex power series approximations of the predistorter and power amplifier's complex gain

$$F[x_m(t)] = \alpha_1 + \alpha_3 x_m(t) + \alpha_5 x_m^2(t) \tag{A.1}$$

$$G[x_d(t)] = \beta_1 + \beta_3 x_d(t) + \beta_5 x_d^2(t) \tag{A.2}$$

into the truncated complex power series approximation for the composite complex gain to obtain

$$K[x_m(t)] = \gamma_1 + \gamma_3 x_m(t) + \gamma_5 x_m^2(t) \tag{A.3}$$

$$= [\alpha_1 + \alpha_3 x_m(t) + \alpha_5 x_m^2(t)]\,[\beta_1 + \beta_3 x_d(t) + \beta_5 x_d^2(t)]$$

$$= \alpha_1\beta_1 + \alpha_3\beta_1 x_m(t) + \alpha_5\beta_1 x_m^2(t) + \alpha_1\beta_3 x_d(t) + \alpha_3\beta_3 x_m(t)x_d(t)$$

$$+ \alpha_1\beta_5 x_d^2(t) + \alpha_5\beta_3 x_m^2(t)x_d(t) + \alpha_3\beta_5 x_m(t)x_d^2(t) + \alpha_5\beta_5 x_m^2(t)x_d^2(t)$$

Next, expand the terms of equation (A.3) in order to express the composite complex gain as a function of $x_m(t)$ only. The last three terms of equation (A.3) are ignored since their expansion yields higher order terms than required. The following relationships are used in simplifying the terms of equation (A.3)

$$x_m(t) = |V_m(t)|^2 \tag{A.4}$$

$$x_d(t) = |V_d(t)|^2 \tag{A.5}$$

$$V_d(t) = V_m(t)\cdot F[x_m(t)] = V_m(t)\,[\alpha_1 + \alpha_3 x_m(t) + \alpha_5 x_m^2(t)] \tag{A.6}$$

Using equations (A.4), (A.5) and (A.6) the 4th, 5th and 6th terms of equation (A.3) are expanded to

$$\alpha_1\beta_3 x_d(t) = \alpha_1\beta_3 |V_d(t)|^2 = \alpha_1\beta_3 V_d(t)V_d^*(t) \tag{A.7}$$

$$= \alpha_1\beta_3[V_m(t)(\alpha_1 + \alpha_3 x_m(t) + \alpha_5 x_m^2(t))]\,[V_m(t)(\alpha_1 + \alpha_3 x_m(t) + \alpha_5 x_m^2(t))]^*$$

$$= \alpha_1\beta_3 x_m(t)\,[\alpha_1\alpha_1^* + \alpha_3\alpha_1^* x_m(t) + \alpha_5\alpha_1^* x_m^2(t) + \alpha_1\alpha_3^* x_m(t)$$

$$+ \alpha_3\alpha_3^* x_m^2(t) + \alpha_5\alpha_3^* x_m^3(t) + \alpha_1\alpha_5^* x_m^2(t) + \alpha_3\alpha_5^* x_m^3(t) + \alpha_5\alpha_5^* x_m^4(t)]$$

$$= \alpha_1|\alpha_1|^2\beta_3 x_m(t) + \alpha_1\beta_3\alpha_3\alpha_1^* x_m^2(t) + \alpha_1\beta_3\alpha_1\alpha_3^* x_m^2(t) + \textit{higher order terms}$$

$$= \alpha_1|\alpha_1|^2\beta_3 x_m(t) + 2\alpha_1\beta_3\,\mathrm{Re}\{\alpha_1\alpha_3^*\}x_m^2(t) + \textit{higher order terms}$$

$$\alpha_3\beta_3 x_m(t)x_d(t) = \alpha_3\beta_3 x_m(t)\,|\,V_d(t)\,|^2 = \alpha_3\beta_3 x_m(t)V_d(t)V_d^*(t) \tag{A.8}$$

$$= \alpha_3\beta_3 x_m(t)\,[V_m(t)(\alpha_1 + \alpha_3 x_m(t) + \alpha_5 x_m^2(t))]\,[V_m(t)(\alpha_1 + \alpha_3 x_m(t) + \alpha_5 x_m^2(t))]^*$$

$$= \alpha_3\beta_3 x_m^2(t)\,[\alpha_1\alpha_1^* + \alpha_3\alpha_1^* x_m(t) + \alpha_5\alpha_1^* x_m^2(t) + \alpha_1\alpha_3^* x_m(t)$$

$$+ \alpha_3\alpha_3^* x_m^2(t) + \alpha_5\alpha_3^* x_m^3(t) + \alpha_1\alpha_3^* x_m^2(t) + \alpha_3\alpha_3^* x_m^3(t) + \alpha_5\alpha_3^* x_m^4(t)]$$

$$= |\,\alpha_1\,|^2\alpha_3\beta_3 x_m^2(t) + \textit{higher order terms}$$

$$\alpha_1\beta_5 x_d^2(t) = \alpha_1\beta_5[V_d(t)V_d^*(t)]\,[V_d(t)V_d^*(t)] \tag{A.9}$$

$$= \alpha_1\beta_5\alpha_1\alpha_1^*\alpha_1\alpha_1^* x_m^2(t) + \quad \textit{higher order terms}$$

$$= \alpha_1|\,\alpha_1\,|\,\beta_5^4 x_m^2(t) + \quad \textit{higher order terms}$$

Substituting equations (A.7), (A.8) and (A.9) into equation (A.3) yields the following expressions for the γ coefficients

$$\gamma_1 = \alpha_1\beta_1 \tag{A.10}$$

$$\gamma_3 = \alpha_3\beta_1 + \alpha_1\beta_3|\,\alpha_1\,|^2 \tag{A.11}$$

$$\gamma_5 = \alpha_5\beta_1 + \alpha_3\beta_3|\,\alpha_1\,|^2 + \alpha_1\beta_5|\,\alpha_1\,|^4 + 2\alpha_1\beta_3\Re e\{\alpha_1\alpha_3^*\} \tag{A.12}$$

The derivation can be taken one step further, by writing the complex α and β coefficients into their real and imaginary form, meaning that the expressions for the complex γ coefficients from equations (A.10), (A.11) and (A.12) become

$$\gamma_1 = (\alpha_{11} + j\alpha_{21})(\beta_{11} + j\beta_{21}) = (\alpha_{11}\beta_{11} - \alpha_{21}\beta_{21}) + j(\alpha_{11}\beta_{21} + \alpha_{21}\beta_{11}) \tag{A.13}$$

$$\therefore \gamma_{11} = \alpha_{11}\beta_{11} - \alpha_{21}\beta_{21} \tag{A.15}$$

$$\gamma_{21} = \alpha_{11}\beta_{21} + \alpha_{21}\beta_{11} \tag{A.16}$$

$$\gamma_3 = (\alpha_{13} + j\alpha_{23})(\beta_{11} + j\beta_{21}) + (\alpha_{11} + j\alpha_{21})(\beta_{13} + j\beta_{23})(\alpha_{11}^2 + \alpha_{21}^2) \tag{A.17}$$

$$\therefore \gamma_{13} = \alpha_{13}\beta_{11} - \alpha_{23}\beta_{21} + \alpha_{11}^3\beta_{13} - \alpha_{11}^2\alpha_{21}\beta_{23} + \alpha_{11}\alpha_{21}^2\beta_{13} - \alpha_{21}^3\beta_{23} \tag{A.18}$$

$$\gamma_{23} = \alpha_{23}\beta_{11} + \alpha_{13}\beta_{21} + \alpha_{11}^2\alpha_{21}\beta_{13} + \alpha_{11}^3\beta_{23} + \alpha_{21}^3\beta_{13} + \alpha_{11}\alpha_{21}^2\beta_{23} \tag{A.19}$$

$$\gamma_5 = (\alpha_{15} + j\alpha_{25})(\beta_{11} + j\beta_{21}) + (\alpha_{13} + j\alpha_{23})(\beta_{13} + j\beta_{23})(\alpha_{11}^2 + \alpha_{21}^2) \tag{A.20}$$

$$+ (\alpha_{11} + j\alpha_{21})(\beta_{15} + j\beta_{25})(\alpha_{11}^4 + 2\alpha_{11}^2\alpha_{21}^2 + \alpha_{21}^4) + 2(\alpha_{11} + j\alpha_{21})(\beta_{13} + j\beta_{23})(\alpha_{11}\alpha_{13} + \alpha_{21}\alpha_{23})$$

E

$$\therefore \gamma_{15} = -\alpha_{21}^5\beta_{25} + \alpha_{11}^5\beta_{15} + \alpha_{11}\alpha_{21}^4\beta_{15} - \alpha_{21}\alpha_{11}^4\beta_{25} + 2\alpha_{11}^3\alpha_{21}^2\beta_{15} - 2\alpha_{21}^3\alpha_{11}^2\beta_{25} \quad \text{(A.21)}$$

$$+ \alpha_{13}\alpha_{11}^2\beta_{13} + \alpha_{13}\alpha_{21}^2\beta_{13} - \alpha_{23}\alpha_{11}^2\beta_{23} - \alpha_{23}\alpha_{21}^2\beta_{23} + 2\alpha_{11}^2\alpha_{13}\beta_{13} \quad \text{(A.22)}$$

$$- 2\alpha_{21}^2\alpha_{23}\beta_{23} - 2\alpha_{21}\alpha_{11}\alpha_{13}\beta_{23} + 2\alpha_{11}\alpha_{21}\alpha_{23}\beta_{13} + \alpha_{15}\beta_{11} - \alpha_{25}\beta_{21}$$

$$\gamma_{25} = \alpha_{21}^5\beta_{15} + \alpha_{11}^5\beta_{25} + \alpha_{11}\alpha_{21}^4\beta_{25} + \alpha_{11}^4\alpha_{21}\beta_{15} + 2\alpha_{21}^3\alpha_{11}^2\beta_{15} + 2\alpha_{11}^3\alpha_{21}^2\beta_{25}$$

$$+ \alpha_{11}^2\alpha_{23}\beta_{13} + \alpha_{21}^2\alpha_{23}\beta_{13} + \alpha_{11}^2\alpha_{13}\beta_{23} + \alpha_{21}^2\alpha_{13}\beta_{23} + 2\alpha_{21}^2\alpha_{23}\beta_{13}$$

$$+ 2\alpha_{11}^2\alpha_{13}\beta_{23} + 2\alpha_{21}\alpha_{11}\alpha_{13}\beta_{13} + 2\alpha_{11}\alpha_{21}\alpha_{23}\beta_{23} + \alpha_{25}\beta_{11} + \alpha_{15}\beta_{21}$$

APPENDIX B

Mathematical Derivation of IMD Quadrature Demodulator Circuit Output

Using an AM signal as input to a power amplifier, its input and output signals have the form

$$RF\ \ signal = B^{'}\cos\omega_c t + A_u^{'}\cos(\omega_c+\omega_m)t + C_u^{'}\cos(\omega_c+2\omega_m)t + D_u^{'}\cos(\omega_c+3\omega_m)t + A_l^{'}\cos(\omega_c-\omega_m)t + C_l^{'}\cos(\omega_c-2\omega_m)t + D_l^{'}\cos(\omega_c-3\omega_m)t \quad \text{(B.1)}$$

E

$$LO\ \ signal = B\cos\omega_c t + A_l\cos(\omega_c-\omega_m)t + A_u\cos(\omega_c+\omega_m)t$$

The mixer's output signal is

$$\begin{aligned} mixer\ output\ =\ & B^{'}B\cos(\omega_c)t\cdot\cos(\omega_c)t + A_u^{'}B\cos(\omega_c+\omega_m)t\cdot\cos(\omega_c)t \\ & + C_u^{'}B\cos(\omega_c+2\omega_m)t\cdot\cos(\omega_c)t + D_u^{'}B\cos(\omega_c+3\omega_m)t\cdot\cos(\omega_c)t \\ & + A_l^{'}B\cos(\omega_c-\omega_m)t\cdot\cos(\omega_c)t + C_l^{'}B\cos(\omega_c-2\omega_m)t\cdot\cos(\omega_c)t \\ & + D_l^{'}B\cos(\omega_c-3\omega_m)t\cdot\cos(\omega_c)t + B^{'}A_l\cos(\omega_c)t\cdot\cos(\omega_c-\omega_m)t \\ & + A_u^{'}A_l\cos(\omega_c+\omega_m)t\cdot\cos(\omega_c-\omega_m)t + C_u^{'}A_l\cos(\omega_c+2\omega_m)t\cdot\cos(\omega_c-\omega_m)t \\ & + D_u^{'}A_l\cos(\omega_c+3\omega_m)t\cdot\cos(\omega_c-\omega_m)t + A_l^{'}A_l\cos(\omega_c-\omega_m)t\cdot\cos(\omega_c-\omega_m)t \\ & + C_l^{'}A_l\cos(\omega_c-2\omega_m)t\cdot\cos(\omega_c-\omega_m)t + D_l^{'}A_l\cos(\omega_c-3\omega_m)t\cdot\cos(\omega_c-\omega_m)t \\ & + B^{'}A_u\cos(\omega_c)t\cdot\cos(\omega_c+\omega_m)t + A_u^{'}A_u\cos(\omega_c+\omega_m)t\cdot\cos(\omega_c+\omega_m)t \\ & + C_u^{'}A_u\cos(\omega_c+2\omega_m)t\cdot\cos(\omega_c+\omega_m)t + D_u^{'}A_u\cos(\omega_c+3\omega_m)t\cdot\cos(\omega_c+\omega_m)t \\ & + A_l^{'}A_u\cos(\omega_c-\omega_m)t\cdot\cos(\omega_c+\omega_m)t + C_l^{'}A_u\cos(\omega_c-2\omega_m)t\cdot\cos(\omega_c+\omega_m)t \\ & + D_l^{'}A_u\cos(\omega_c-3\omega_m)t\cdot\cos(\omega_c+\omega_m)t \end{aligned} \quad \text{(B.2)}$$

Using trigonometric identities, all the terms of equation (B.2) can be rewritten as

$$B^{'}B\cos(\omega_c)t\cdot\cos(\omega_c)t = \frac{B^{'}B}{2}\cos(2\omega_c)t + \frac{B^{'}B}{2} \quad \text{(B.3)}$$

$$A_u^{'}B\cos(\omega_c+\omega_m)t\cdot\cos(\omega_c)t = \frac{A_u^{'}B}{2}\cos(2\omega_c+\omega_m)t + \frac{A_u^{'}B}{2}\cos(\omega_m t) \quad \text{(B.4)}$$

$$C_u' B \cos(\omega_c + 2\omega_m)t \cdot \cos(\omega_c)t = \frac{C_u' B}{2}\cos(2\omega_c + 2\omega_m)t + \frac{C_u' B}{2}\cos(2\omega_m)t \quad \text{(B.5)}$$

$$D_u' B \cos(\omega_c + 3\omega_m)t \cdot \cos(\omega_c)t = \frac{D_u' B}{2}\cos(2\omega_c + 3\omega_m)t + \frac{D_u' B}{2}\cos(3\omega_m)t \quad \text{(B.6)}$$

$$A_l' B \cos(\omega_c - \omega_m)t \cdot \cos(\omega_c)t = \frac{A_l' B}{2}\cos(2\omega_c - \omega_m)t + \frac{A_l' B}{2}\cos(-\omega_m)t \quad \text{(B.7)}$$

$$C_l' B \cos(\omega_c - 2\omega_m)t \cdot \cos(\omega_c)t = \frac{C_l' B}{2}\cos(2\omega_c - 2\omega_m)t + \frac{C_l' B}{2}\cos(-2\omega_m)t \quad \text{(B.8)}$$

$$D_l' B \cos(\omega_c - 3\omega_m)t \cdot \cos(\omega_c)t = \frac{D_l' B}{2}\cos(2\omega_c - 3\omega_m)t + \frac{D_l' B}{2}\cos(-3\omega_m)t \quad \text{(B.9)}$$

$$B' A_l \cos(\omega_c)t \cdot \cos(\omega_c - \omega_m)t = \frac{B' A_l}{2}\cos(2\omega_c - \omega_m)t + \frac{B' A_l}{2}\cos(\omega_m)t \quad \text{(B.10)}$$

$$A_u' A_l \cos(\omega_c + \omega_m)t \cdot \cos(\omega_c - \omega_m)t = \frac{A_u' A_l}{2}\cos(2\omega_c t) + \frac{A_u' A_l}{2}\cos(2\omega_m)t \quad \text{(B.11)}$$

$$C_u' A_l \cos(\omega_c + 2\omega_m)t \cdot \cos(\omega_c - \omega_m)t = \frac{C_u' A_l}{2}\cos(2\omega_c + \omega_m)t + \frac{C_u' A_l}{2}\cos(3\omega_m)t \quad \text{(B.12)}$$

$$D_u' A_l \cos(\omega_c + 3\omega_m)t \cdot \cos(\omega_c - \omega_m)t = \frac{D_u' A_l}{2}\cos(2\omega_c + 2\omega_m)t + \frac{D_u' A_l}{2}\cos(4\omega_m)t \quad \text{(B.13)}$$

$$A_l' A_l \cos(\omega_c - \omega_m)t \cdot \cos(\omega_c - \omega_m)t = \frac{A_l' A_l}{2}\cos(2\omega_c - 2\omega_m)t + \frac{A_l' A_l}{2} \quad \text{(B.14)}$$

$$C_l' A_l \cos(\omega_c - 2\omega_m)t \cdot \cos(\omega_c - \omega_m)t = \frac{C_l' A_l}{2}\cos(2\omega_c - 3\omega_m)t + \frac{C_l' A_l}{2}\cos(-\omega_m)t \quad \text{(B.15)}$$

$$D_l' A_l \cos(\omega_c - 3\omega_m)t \cdot \cos(\omega_c - \omega_m)t = \frac{D_l' A_l}{2}\cos(2\omega_c - 4\omega_m)t + \frac{D_l' A_l}{2}\cos(-2\omega_m)t \quad \text{(B.16)}$$

$$B' A_u \cos(\omega_c)t \cdot \cos(\omega_c + \omega_m)t = \frac{B' A_u}{2}\cos(2\omega_c + \omega_m)t + \frac{B' A_u}{2}\cos(-\omega_m)t \quad \text{(B.17)}$$

$$A_u' A_u \cos(\omega_c + \omega_m)t \cdot \cos(\omega_c + \omega_m)t = \frac{A_u' A_u}{2}\cos(2\omega_c + 2\omega_m)t + \frac{A_u' A_u}{2} \tag{B.18}$$

$$C_u' A_u \cos(\omega_c + 2\omega_m)t \cdot \cos(\omega_c + \omega_m)t = \frac{C_u' A_u}{2}\cos(2\omega_c + 3\omega_m)t + \frac{C_u' A_u}{2}\cos(\omega_m)t \tag{B.19}$$

$$D_u' A_u \cos(\omega_c + 3\omega_m)t \cdot \cos(\omega_c + \omega_m)t = \frac{D_u' A_u}{2}\cos(2\omega_c + 4\omega_m)t + \frac{D_u' A_u}{2}\cos(2\omega_m)t \tag{B.20}$$

$$A_l' A_u \cos(\omega_c - \omega_m)t \cdot \cos(\omega_c + \omega_m)t = \frac{A_l' A_u}{2}\cos(2\omega_c)t + \frac{A_l' A_u}{2}\cos(-2\omega_m)t \tag{B.21}$$

$$C_l' A_u \cos(\omega_c - 2\omega_m)t \cdot \cos(\omega_c + \omega_m)t = \frac{C_l' A_u}{2}\cos(2\omega_c - \omega_m)t + \frac{C_l' A_u}{2}\cos(-3\omega_m)t \tag{B.22}$$

$$D_l' A_u \cos(\omega_c - 3\omega_m)t \cdot \cos(\omega_c + \omega_m)t = \frac{D_l' A_u}{2}\cos(2\omega_c - 2\omega_m)t + \frac{D_l' A_u}{2}\cos(-4\omega_m)t \tag{B.23}$$

Collecting the amplitudes of the signals at DC, f_m, $2f_m$, $3f_m$ and $4f_m$ the spectrum shown in Figure B.1 is obtained. Note that the spectrum of Figure B.1 agrees with the positive side of the spectrum of Figure 2.8, which was the spectrum obtained by complex convolution.

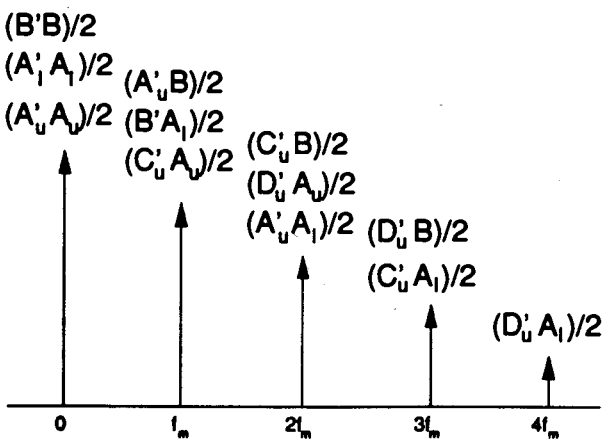

Figure B.1. Spectra of Down-converted Signal

APPENDIX C

Schematics of Implemented Predistorter

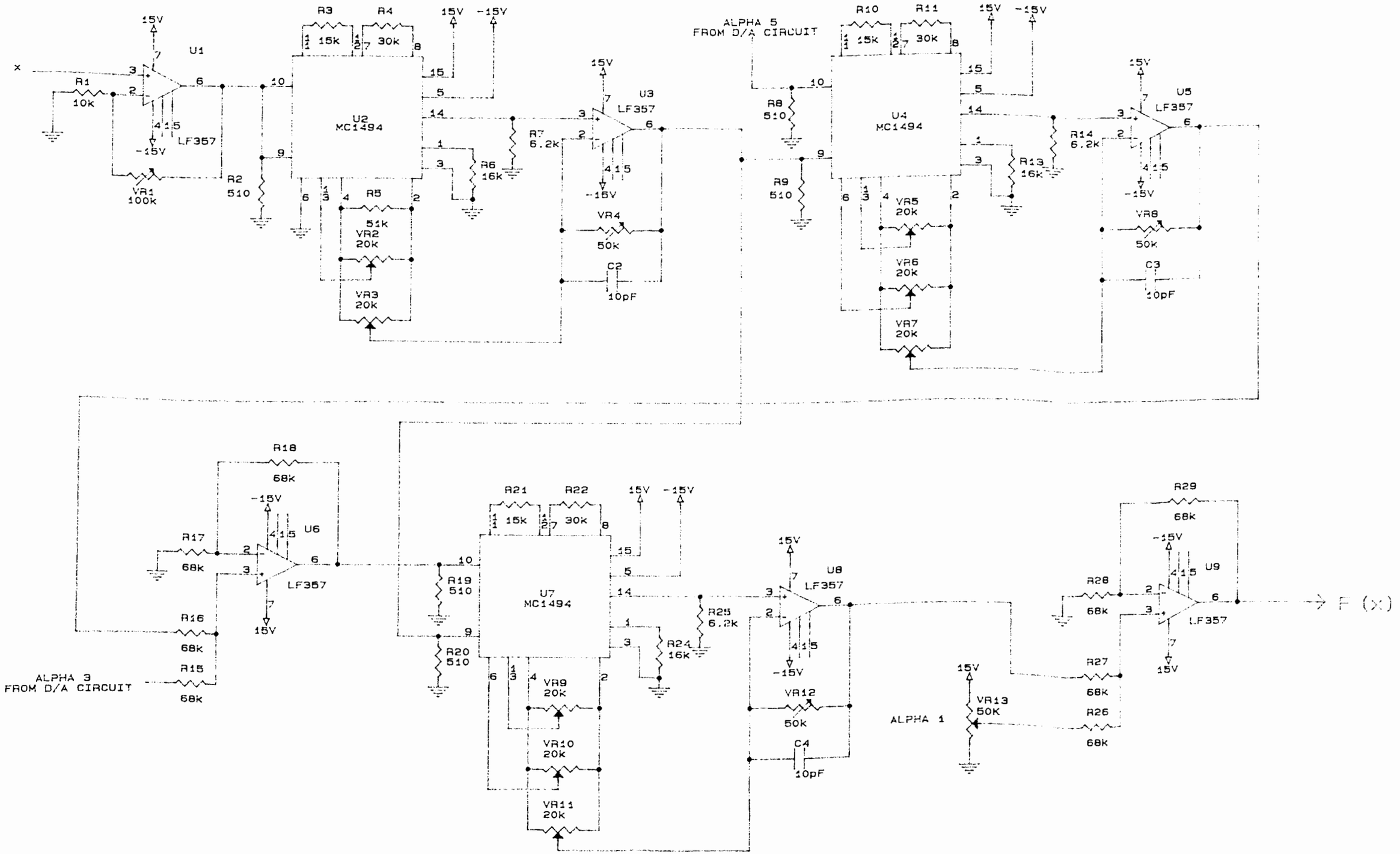

Figure C.1. Schematic of F1 or F2 Circuit

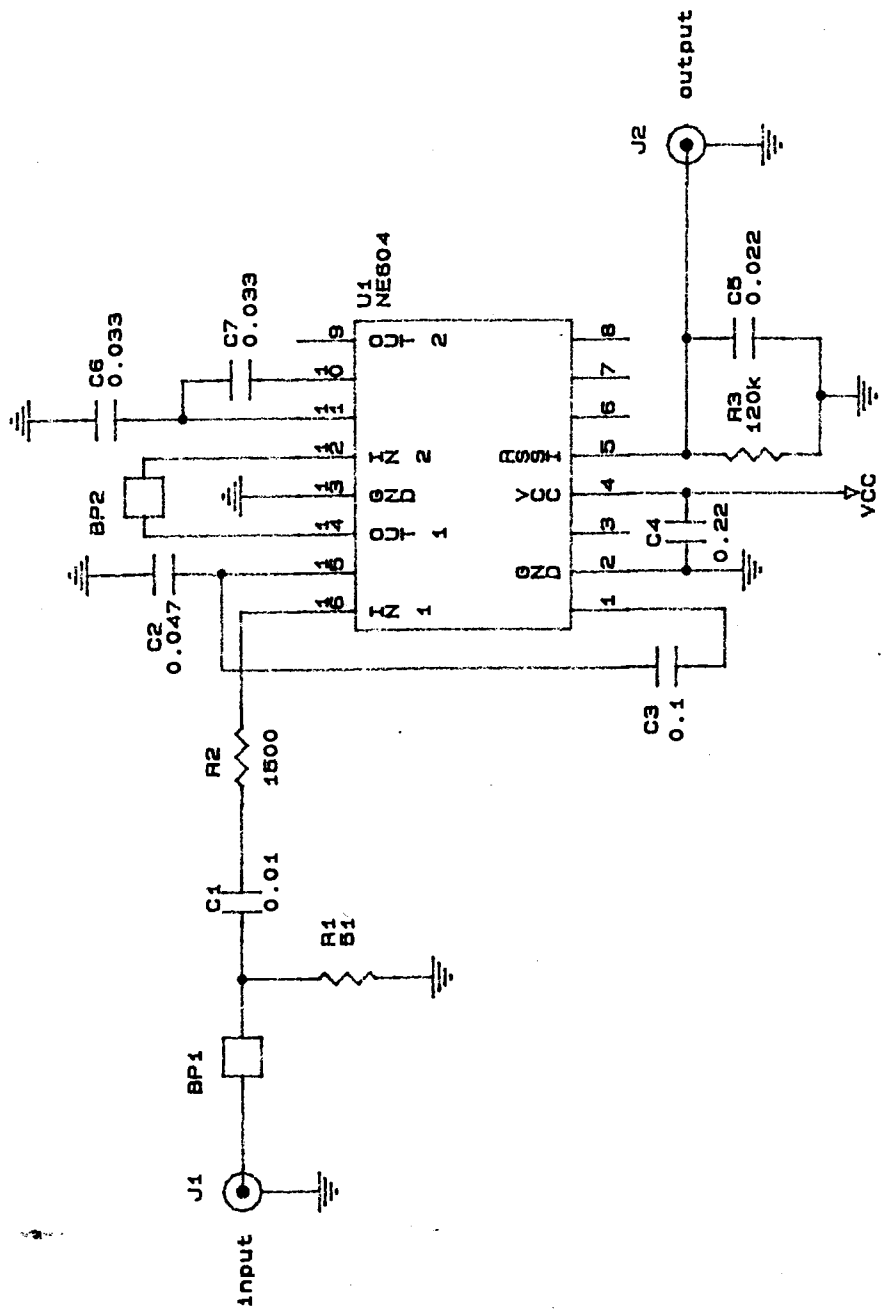

Figure C.2. Schematic of Power Detector Circuit

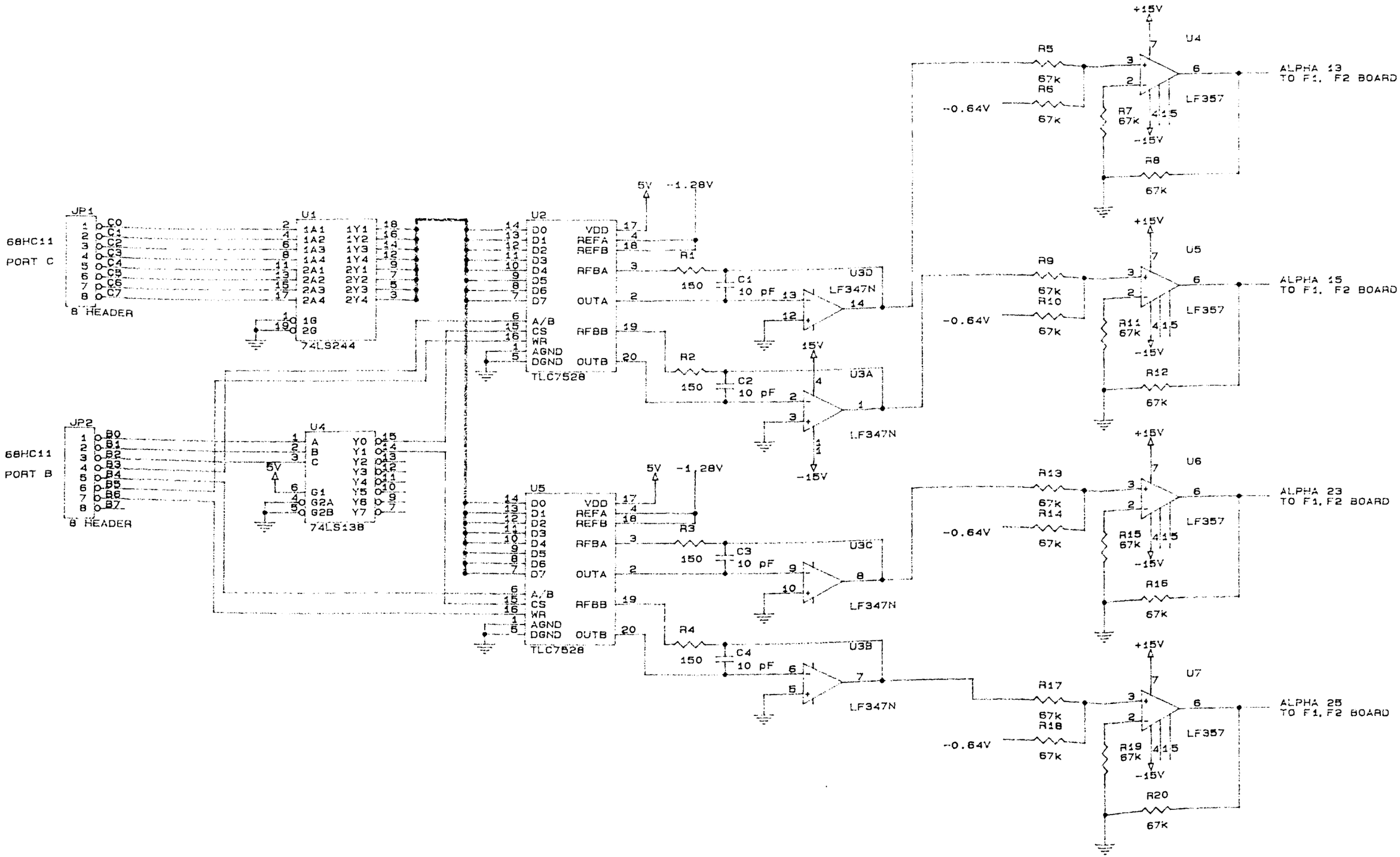

Figure C.3. Schematic of DAC Circuit Interface

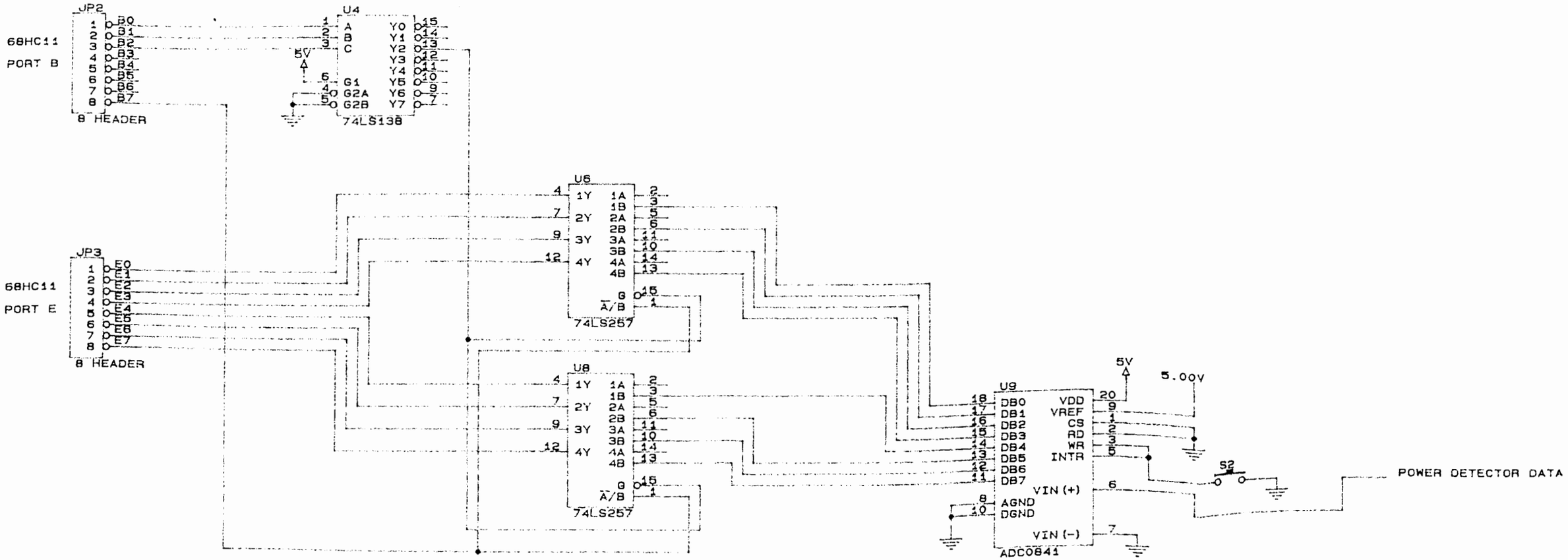

Figure C.4. Schematic of ADC Circuit Interface